Title

Evolution of technology and molecular sensor diversity in hyperpolarized xenon NMR of biological and oriented environments

Author

Truxal, Ashley

Publication Date

2018

Peer reviewed|Thesis/dissertation

Evolution of technology and molecular sensor diversity in hyperpolarized xenon NMR of biological and oriented environments

by

Ashley Truxal

A dissertation submitted in partial satisfaction of the

requirements for the degree of

Doctor of Philosophy

in

Chemistry

in the

Graduate Division

of the

University of California, Berkeley

Committee in charge:

Professor Alexander Pines, Chair
Professor David E. Wemmer
Professor Jeffrey A. Reimer

Fall 2018

Evolution of technology and molecular sensor diversity in hyperpolarized xenon NMR of biological and oriented environments

Abstract

Evolution of technology and molecular sensor diversity in hyperpolarized xenon NMR of biological and oriented environments

by

Ashley Truxal

Doctor of Philosophy in Chemistry

University of California, Berkeley

Professor Alexander Pines, Chair

The work in this dissertation revolves around the use and evolution of methods and molecular contrast agents for ^{129}Xe nuclear magnetic resonance (NMR) techniques. A general overview of the scope of this work is provided in Chapter 1. An overview of the basic principles of magnetic resonance, the manipulation of magnetization in an NMR experiment, and the ways data from NMR experiments can be treated is provided in Chapter 2. Chapter 3 introduces hyperpolarized ^{129}Xe NMR and describes the theoretical background and current applications of hyperpolarized xenon as they apply to biosensing, including the functionalization of xenon for molecular detection using macromolecular hosts and the principles of the hyperpolarized gas chemical exchange saturation transfer (hyperCEST) technique. Practical technical considerations involved with hyperpolarized ^{129}Xe gas generation and delivery are provided in Chapter 4. The following three chapters each expound upon a completely different type of ^{129}Xe sensor explored as a part of this thesis work: a cryptophane derivative (Chapter 5), a cucurbit[6]uril rotaxane (Chapter 6), and a targeted cucurbit[7]uril (Chapter 7), while Chapter 8 introduces a new device that enables examination of hyperpolarized ^{129}Xe in viscous and orienting media. Chapter 9 synthesizes all the components of previous chapters to explore the use of orienting media to further enhance molecular detection. This dissertation concludes in Chapter 10 with a clear direction for the next steps toward sensitive analysis of unprocessed biological samples with ^{129}Xe NMR.

To my invaluable friends and mentors

Contents

List of Figures

List of Tables

Acknowledgments

This dissertation work was an education in much more than academic research. While working innumerable days and nights underneath superconducting magnets, within the polarizer framework, and behind my office computer, I learned pramgmatism, diplomacy, and tenacity. Although the creative autonomy offered by Alex was exciting, inspiring and appreciated, I could not have learned these skills alone; I owe my achievements to the guidance and support of many mentors and friends.

First, I am grateful to my father, who taught me to never venture out into the world without duct tape, because most problems can be solved with nothing more than a careful wit and a roll of duct tape (and, after a certain age, an angle grinder).

From there, I'd like to thank Dr. Chris Vassiliou, who taught me the most important thing I learned in my first year as a graduate student: when a small part is dropped on the floor, do not move reflexively! First, Spot the part. Then, figure out the best way to retrieve it. In many ways, this advice has become invaluable. My greatest mentor and comrade in the lab was Clancy Slack, who taught me how to negotiate the minefield of academic politics, have confidence in my own abilities over the assertions of others', and somehow remain empathetic. I am glad to have provided and received support from my lab colleague Muller Gomes, and have appreciated all of his incredible theoretical insight.

Outside of the lab, no one fellow scientist kept me as grounded nor advocated for me as ferociously as Nicole Haloupek, in all possible ways. My peers in other labs, Natalie Gibson and Samuel Kenny, provided me with both helpful criticism of and liberation from my work, both being of incredible and equal value. I extend additional endless thanks to my closest and longest friend, Rachel Welch, for her unflinching support through each setback and accomplishment in- and outside of my graduate career.

I am very thankful for Alex's endless support and enthusiasm for my strange ideas as well as my teaching and outreach pursuits. It is rare in these times to find a doctorate adviser that cares so much about the cultivation of teaching and communications skills alongside research techniques. I'd like to thank Dave Wemmer for his unending skepticism of all data presented to him, as it has led to the construction of solid scientific work from all those who have had the privilege of working under his tutelage. I thank both Dave Wemmer and Jeff Reimer for their careful review and helpful feedback throughout this dissertation work.

Finally, I would like to thank Terry Valentino, who, in his martial arts teachings, impressed upon me that anyone can tolerate any impossible challenge for a finite amount of time.

Symbols

$\otimes$	Tensor product
$\cdot$	Dot product
$\|\psi\rangle$	A ket vector in Hilbert space
$\langle\psi\|$	A bra dual vector in Hilbert space
$p_{nm} = c_n c_m^* \|n\rangle\langle m\|$	A density matrix describing ensemble quantum state
$\mathcal{H}$	Hamiltonian, the total energy operator of a system
$\mathbf{B}$	Magnetic field vector
B_0	Amplitude of external static magnetic field
$\mathbf{I}$	Nuclear spin operators
$\mathbf{S}$	Electron spin operators
$\mathbf{A}$	Hyperfine tensor
ZFS	Zero-field splitting
γ	Gyromagnetic ratio of spin
B_1	Radio frequency field
T_1^*	effective spin-lattice relaxation time
T_2^*	effective spin-spin relaxation time
T_1	spin-lattice relaxation time
T_2	spin-spin relaxation time
$\mathbf{M}$	Spin magnetization
$\vec{B_0}$	Magnetic field vector
B_0	Amplitude of the static magnetic field
Ω	Offset frequency
ω_0	Resonance frequency

Abbreviations

BM	Bloch-McConnell
CA	contrast agent
CB6	Cucurbit[6]uril
CB7	Cucurbit[7]uril
CBn	Cucurbit[n]uril
CEST	Chemical exchange saturation transfer
CPMG	Carr Purcell Meiboom Gill
CryA	Cryptophane-A
FID	Free induction decay
FOV	Field of view
FWHM	Full width at half-maximum
Hp-	Hyperpolarized
HyperCEST	Hyperpolarized Xenon chemical exchange saturation transfer
ID	Inner diameter
MR	Magnetic resonance
NMR	Nuclear magnetic resonance
OD	Outer diameter
PDMS	Polydimethyl siloxane
PEEK	Polyether ether ketone
PMMA	Polymethyl methacrylate
Ppm	Parts per million
Rb	Rubidium
RF	Radiofrequency
SEOP	Spin-Exchange Optical-Pumping
SLPM	Standard liter per minute
Xe	Xenon

Physical Constants

h	Planck constant, 6.626176×10^{-34} J· s
$\hbar$	Reduced Planck constant, h/2π
k_B	Boltzmann constant, 1.380662 times 10^{-23} J/K
e	Electron charge, 1.602177×10^{-19} C
m_e	Electron rest mass, 9.109383×10^{-31} kg
m_p	Proton rest mass, 1.672622×10^{-27} kg
μ_0	Vacuum permeability, $4\pi \times 10^{-7}$ V · s/(A· m)
g_s	Electron g-factor, -2.00231930436153 $\pm$ 2.6 $\times 10^{-13}$
μ_B	Bohr magneton, e$\hbar$/(2m$_e$) = 9.274×10^{-24} J/T
μ_N	Nuclear magneton, e$\hbar$/(2m$_p$) = 5.051 $\times 10^{-27}$ J/T

Chapter 1

Introduction

"Magnetism, it was my greatest weapon, and without it, I am lost" –Magneto

1.1 Motivation

The speed with which scientists are uncovering early pathogenic markers such as small changes in serum concentrations of antibodies, metabolites and enzymes now far outpaces the development of diagnostic imaging techniques sufficiently sensitive to detect them. Efficient and universal biosensors for the characterization of pathologies are highly desired, but existing sensors and imaging methods either require sophisticated labeling with radioactive isotopes (e.g., in positron-emission tomography (EPT) or single-photon emission computed tomography (SPECT)), cannot image through opaque media (optical microscopy), or are insensitive (such as magnetic resonance imaging (MRI) and ultrasound).[1] However, the signal amplitude, and, thus, sensitivity of MRI can be increased by 4–8 orders of magnitude by using hyperpolarization techniques.[2–4] Hyperpolarization of solids, liquids, and gases has been demonstrated via a number of techniques including Brute Force Polarization (BFP), Spin Exchange Optical Pumping (SEOP), Dynamic Nuclear Polarization (DNP), Chemically-Induced Dynamic Nuclear Polarization (CIDNP), Parahydrogen Induced Polarization (PHIP) and Signal Amplification By Reversible Exchange (SABRE).[5–12] Hyperpolarization techniques are revolutionizing the fields of NMR spectroscopy and MRI, as many applications that were previously inaccessible or impractical due to weak NMR signals are now becoming possible. Moreover, the enormous gain in attainable signal-to-noise ratio (SNR) allows spectroscopic detection and imaging of hyperpolarized compounds to be performed in seconds, obviating the need for time-consuming signal averaging and recovery of the spin magnetization to thermal equilibrium.

Of these, hyperpolarized ^{129}Xe MRI is a promising alternative to conventional MRI techniques that yields practical detection limits of small biological targets without the risks associated with ionizing radiation.[13] ^{129}Xe nuclei can be hyperpolarized by SEOP such that signal is increased by 4–5 orders of magnitude compared to thermal polarization.[2] Xenon

gas is an attractive contrast agent because it is inert, exogenous, and non-toxic; it has even been in use as an anesthetic gas for decades.[14–16] Initial applications of hyperpolarized ^{129}Xe MRI included lung imaging and probing of hydrophobic regions in proteins for structural and kinetic information, and newer applications include *in vivo* brain and live-cell imaging with the help of innovative pulse sequence and reconstruction methods.[14,17,18]

The advent of macromolecular host molecules with which xenon atoms transiently associate has enabled selective, localized detection of a diverse range of biological targets in both *in vivo* and *in vitro* contexts.[19,20] Xenon atoms exchange in and out of the hosts, acting as a reporter of the hosts' chemical environment through ^{129}Xe chemical shift or relaxation measurements. When these hosts interact with their specific targets, they give rise to unique resonances on a ^{129}Xe NMR spectrum. Ideally, both the free and bound hosts, termed biosensors, have resolved xenon signals, allowing quantitation of concentration and kinetic parameters. Biosensors based on organic supramolecular compounds such as cryptophanes, cyclodextrin conjugates, and cucurbiturils, as well as larger macromolecules (gas vesicles, nanodroplets, small proteins, inorganic frameworks and more) have been developed in the last decade alone.[20] This ever-expanding variety of xenon biosensors has been applied to the selective detection and monitoring of binding events involving receptors on cell surfaces, transmembrane proteins, enzymes, and microenvironments indicative of tumor pathology such as abnormal pH or oxidation values. Application of chemical exchange saturation transfer (CEST) techniques to hyperpolarized xenon (hyperCEST) has further improved detection limits of biosensors to nano- and picomolar scales.[21] HyperCEST exploits the exchange of thousands of xenon atoms in and out of a biosensor in one saturation cycle to greatly lower the detection limits of both biosensors and biological targets for detection. Recent developments in ultra-fast hyperCEST imaging have made the prospect of fast, selective, and sensitive hyperpolarized ^{129}Xe MRI viable.

This dissertation encompasses work on the use and development of contrast agents and devices for hyperpolarized ^{129}Xe MRI applications. An overview of the basic principles of magnetic resonance, the manipulation of magnetization in an NMR experiment, and the ways data from NMR experiments can be treated will be provided in Chapter 2. The magnetic resonance physics discussed in this introduction will largely be from the NMR spectroscopy perspective, and any notable deviations in MRI will be noted. Chapter 3 introduces hyperpolarized ^{129}Xe NMR and describes the theoretical background and current applications of hyperpolarized xenon as they apply to biosensing, including the functionalization of xenon for molecular detection using macrocyclic hosts and the principles of the hyperpolarized gas chemical exchange saturation transfer (hyperCEST) technique. Practical technical considerations involved with hyperpolarized ^{129}Xe gas generation and delivery are provided in Chapter 4. The following three chapters each expound upon a completely different type of ^{129}Xe sensor explored as a part of this thesis work. Chapter 5 takes a classic cryptophane-based sensor and explores its sensitivity to different structural deformities caused by the chelation of metal ions. Chapter 6 introduces a more recent style of cucurbituril-based rotaxane biosensor that 'turns on' in specific chemical milieus; in this case, in oxidizing envi-

ronments due to pathologic upregulation of hydrogen peroxide. Then, in Chapter 7, a new, directly functionalized cucurbituril combines the benefits of directly functionalized sensors like the cryptophanes with cucurbiturils' optimal exchange dynamics for hyperCEST imaging to enable selective, 'always on' detection of avidin, a small protein, opening the doors for the detection of a huge array of biorelevant targets via bioconjugation.

Changing perspectives, Chapter 8 pursues evolution of ^{129}Xe molecular detection from the instrumental perspective, introducing a new device that enables examination of hyperpolarized ^{129}Xe in viscous and orienting media. Chapter 9 synthesizes all the components of previous chapters to explore the use of orienting media to enhance molecular detection by presenting preliminary data showing molecular ordering of CB6 in an aqueous liquid crystal phase, a result that reinforces the potential for improved spectral resolution of xenon biosensors via anisotropic shielding contributions. This dissertation concludes in Chapter 10 and provides direction for the next steps toward enabling sensitive analysis of unprocessed biological samples with ^{129}Xe NMR.

Chapter 2

Nuclear Magnetic Resonance Spectroscopy

2.1 Spin

In magnetic resonance techniques, the property that is manipulated and measured is called spin. The term is thrown around constantly in conversation between NMR spectroscopists. But what is it?

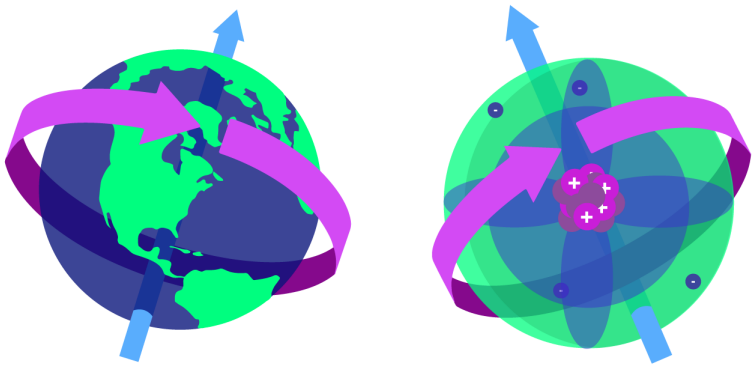

Figure 2.1: Spin exists everywhere in our universe, from celestial bodies to elementary particles.

In everyday life, an object that is spinning is rotating about an axis. Spinning tops, ferris wheels, the planet Earth and even galaxies all spin about some axis. Just as the mass and velocity of an object determines its momentum, a rotating object has an angular mass, called its moment of inertia, and a spinning speed that determines its angular momentum. Angular momentum is a vector that points perpendicular to the plane of rotation. In classical

mechanics, angular momentum is simply the product of an object's moment of inertia (I) and its angular velocity (ω):

$$\vec{L} = I\omega \tag{2.1}$$

For a particle, the same value is derived from the cross product of its position vector and instantaneous linear momentum vector:

$$L = \vec{r} \otimes \vec{p} \tag{2.2}$$

Delving even deeper, quantum mechanics(QM) has its own forms of angular momentum– two, in fact: orbital and spin angular momentum (Fig. 2.2). The first is more like its classical counterparts and is derived from rotating bodies, but is quantized, so it can only take on specific values- this is orbital angular momentum ($\vec{L}$). The classical form above can be translated to QM by simply reinterpreting the $\vec{r}$ and $\vec{p}$ vectors as the operators associated with the position and linear momentum.

The second QM form of angular momentum invokes the inherent "spookiness" of quantum mechanics, as it comes from a property called spin, which does not correspond to any actual rotation of a particle but rather is an intrinsic property that a particle possesses, much like charge or mass. Almost all elementary particles have this property of spin that is unrelated to their spatial motion. This kind of angular momentum is called spin angular momentum ($\vec{S}$), and is the foundation of all magnetic resonance techniques.

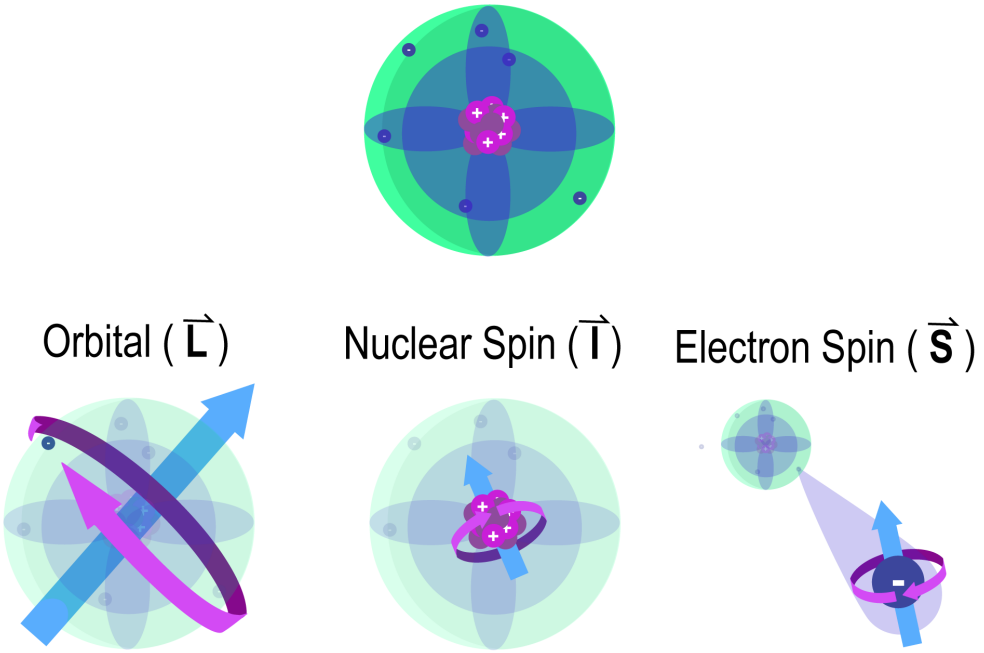

Figure 2.2: The three dominant forms of angular momentum in an atom come from orbiting electrons, (left), nuclear spins (middle) and electron spins (right).

The total angular momentum ($\vec{J}$) of a particle combines both its orbital and spin angular momentum:

$$\vec{J} = \vec{L} + \vec{S} \tag{2.3}$$

The *nuclear* spin angular momentum of a given isotope, specifically, is determined by the particles that comprise it. Quarks have their own spin values, and certain arrangements of quarks determine the spin of the protons and neutrons they build. The sum of proton and neutron spins gives the total nuclear spin (denoted **I** to distinguish from electron spin **S**) of the atom. This is why different isotopes of the same element can have spin, and be 'NMR active,' while others cannot. A nucleus of odd mass number A will have half-integer spin and a nucleus of even A will have integer spin. Some examples of spin values for particles and isotopes are given in Table 2.1. Note that electrons, too have their own spin S = $\frac{1}{2}$, which is the source of the macroscopic magnetism seen in everyday items like refrigerator magnets, electric motors and magnetic strips on credit cards.

Any nucleus with non-zero spin has a magnetic moment associated with it that produces magnetic interactions with its environment:

$$\vec{\mu_I} = \gamma \vec{I} \tag{2.4}$$

Table 2.1: Properties of some NMR-active isotopes[22]

Isotope	**Isotopic abundance**	**Nuclear Spin (I)**	γ_n $(\frac{rad}{s\mu T})$	$\frac{\gamma_n}{2\pi}$ $(\frac{MHz}{T})$
^{1}H	99.98%	1/2	267.522	42.58
^{2}H	0.02%	1	41.066	6.5
^{7}Li	92.60	3/2	103.977	16.5
^{13}C	1.11%	1/2	67.283	10.7
^{14}N	99.63%	1	19.338	3.1
^{19}F	100.00%	1/2	251.623	0.4
^{31}P	100.00%	1/2	108.394	17.2
^{129}Xe	26.4	1/2	-73.997	-11.77
^{131}Xe	21,18	3/2	22.06	3.51

Where gamma is the gyromagnetic ratio, a constant that is specific to each nuclear composition. The energy of interaction between a nuclear magnetic moment and an external magnetic field (B_0) can be thought of as a torque acting on a magnetic dipole:

$$E = -\vec{\mu_I} \cdot \mathbf{B}_0 = -\mu_{I_z} B_{0z} - \mu_{I_y} B_{0,y} - \mu_{I_x} B_{0x} \tag{2.5}$$

The total magnetic moment, or magnetization of an ensemble of spins is the sum of all the individual magnetic moments of the spins:

$$\mathbf{M} = \sum_i \mu_{\mathbf{i}} \tag{2.6}$$

Technically, any nucleus with non-zero spin (and therefore non-zero magnetic moment) is NMR-active, but the most conveniently probed nuclei tend to have a total nuclear spin of $\frac{1}{2}$. This is best explained through history: in 1922, Stern and Gerlach performed an experiment where silver atoms possessing only one valence electron were sent through an inhomogeneous magnetic field. They were deflected by said field into two discrete populations, evidenced by silhouettes they left as they passed through a foil canvas (Fig 2.3).

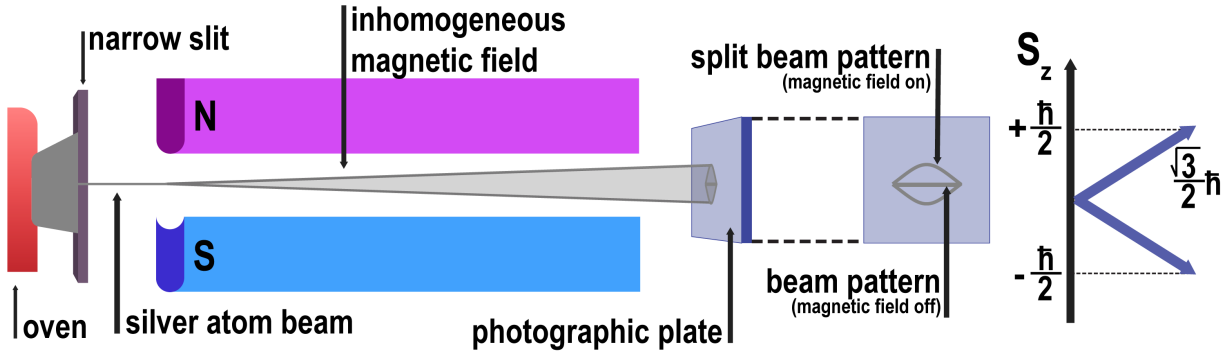

Figure 2.3: The Stern-Gerlach experiment confirmed the quantization of electron spin into two orientations. In the experiment, a beam of silver atoms was sent through an inhomogeneous magnetic field, which effected an energetic torque that broke the degeneracy of the silver atoms' electronic spin states. This in turn resulted in the deflection of the beam into two distinct paths, the separation of which is proportional to the electron spin (right) and magnetic field gradient.

This is because application of a magnetic field gradient breaks the degeneracy of spin sublevels ($m_s = \pm\frac{1}{2}$). In this case, the atoms had no orbital angular momentum, so two silhouettes were observed because particles could only be deflected into two possible spin states as they passed through the magnet. If the same number of particles is distributed into more states as they pass through the magnet, as for particles of higher spin order, a higher number of discrete silhouettes that are less intense will result. This is one reason why spin-$\frac{1}{2}$ nuclei are favored in NMR: an NMR signal relies on the population difference between nuclear spin states, and that difference will be much easier to register when there are a limited number of possible spin states to occupy. A phenomenon called coupling, in which spins couple to other spins and fields, also causes splitting and broadening of signals. Nuclei of spin order greater than $\frac{1}{2}$ possess nuclear quadrupolar moments that couple to electric field gradients (See Chapter 9 for relevant terms) and cause both splitting and broadening, while spin-$\frac{1}{2}$ nuclei do not.

2.2 The NMR experiment

2.2.1 Magnetization

A nucleus of spin I has 2I+1 degenerate spin states of values m_I = -I, -I+1,. . . ,I. Thus, for spin-$\frac{1}{2}$ nuclei, there are 2 degenerate m_I-levels of values $+\frac{1}{2}$ and $-\frac{1}{2}$. There is no preferred orientation for these spins and thus no net magnetization. When placed in an external magnetic field (B_0), however, some degree of alignment of the spins with or against that field becomes more energetically favorable. Usually, B_0 is chosen to be along the z-axis, such that 9.5) reduces to

$$E = -\mu_{I_z} B_0 \tag{2.7}$$

As a result, degeneracy is lifted, and the m_I sublevels split into *Zeeman* levels whose energy difference depends on the characteristic gyromagnetic ratio of the nucleus and the external field (B_0, Fig. 2.4):

$$E_{m_I} = -\gamma m_I B_0 \tag{2.8}$$

For m $= \pm\frac{1}{2}$,

$$E_{\pm\frac{1}{2}} = \mp\frac{\hbar}{2}\gamma B_0 \tag{2.9}$$

and

$$\Delta E = \gamma\hbar B_0 \tag{2.10}$$

B_0 is usually said to propagate in the $\hat{z}$ direction. The $m_I = +\frac{1}{2}$ and $m_I = -\frac{1}{2}$ states are termed the α and β states, respectively, and the lower-energy α state is designated as that which is aligned with B_0, i.e. along +z, while the β state is aligned against B_0, along -z (Fig. 2.4).[23]

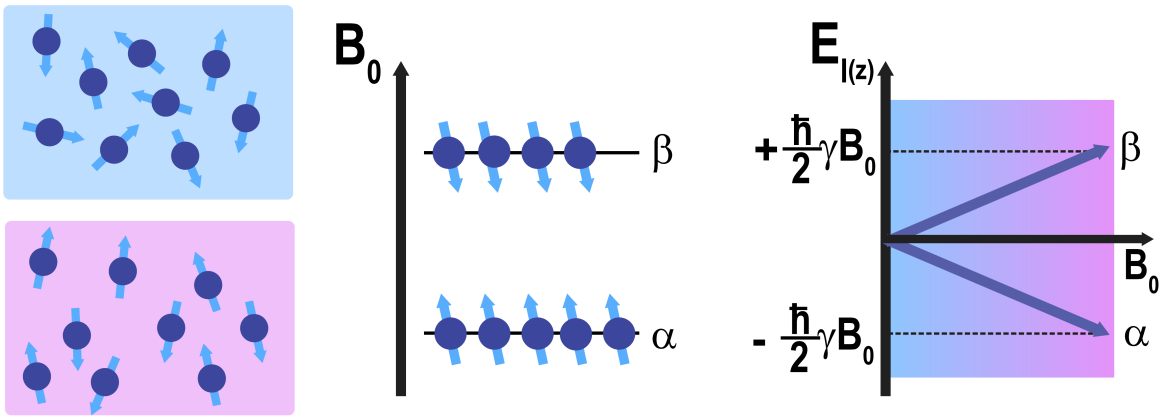

Figure 2.4: In the absence of an external magnetic field, nuclear spins have no preferential orientation (top left), m_l sublevels are degenerate in energy, and there is no net magnetization. However, if a static external field (B_0) is turned on, spins will experience a torque that will cause them to preferentially align with or against that static field (bottom left). α-spin nuclei, being aligned with the external field, are lower in energy than β-spin nuclei, which align against it (middle). α- and β- spins have equal and opposite energies whose separation is dictated by the strength of the external field (right).

The frequency associated with the energy difference between these states is the Larmor precessional frequency,

$$\omega_0 = -\gamma B_0 \tag{2.11}$$

which gets its name from the idea that the spins precess about the external magnetic field (much like a spinning top will wobble in circles as it slows down). Although the number difference between the α and β populations is small (on the order of ppm for protons, see section 2.4), there will be a preponderance of spins aligned with or against the external field, leading to a net magnetization (Eq. 2.6).

It is the net magnetization that is manipulated in an NMR experiment, and its size determines the amplitude of the NMR signal. To visualize how the net magnetization of a spin ensemble changes over time, the Bloch equations are helpful. First, the energy of interaction between the net magnetization and and external field is analogous to that for individual spins, where the application of B_0 effects a torque that change in the angular momentum vector of the net magnetization:

$$\tau = \frac{dL}{dt} = M \times B \tag{2.12}$$

Since $M = \gamma L$,

$$\frac{d\mathbf{M}}{dt} = \gamma \mathbf{M} \times \mathbf{B} \tag{2.13}$$

Expanding gives

$$\mathbf{M} \times \mathbf{B} = \begin{bmatrix} i & j & k \\ M_x & M_y & M_z \\ B_x & B_y & B_z \end{bmatrix} = (M_y B_z - M_z B_y)i + (M_z B_x - M_x B_z)j + (M_x B_y - M_y B_x)k \tag{2.14}$$

In terms of individual components,

$$\begin{aligned} \frac{dM_x}{dt} &= \gamma(M_y B_z - M_z B_y) \\ \frac{dM_y}{dt} &= \gamma(M_z B_x - M_x B_z) \\ \frac{dM_z}{dt} &= \gamma(M_x B_y - M_y B_x) \end{aligned} \tag{2.15}$$

At thermal equilibrium, the only external field is that applied in the z-direction, so B_x=B_y=0 and $B_z = B_0$, and Eqs. 2.15 become

$$\begin{aligned} \frac{dM_x}{dt} &= \gamma M_y(t) B_0 \\ \frac{dM_y}{dt} &= -\gamma M_x(t) B_0) \\ \frac{dM_z}{dt} &= 0 \end{aligned} \tag{2.16}$$

The solutions to these equations are as follows:

$$M_x = M_x cos(\omega t) + M_y sin(\omega t)$$

$$M_y = M_y cos(\omega t) - M_x sin(\omega t)$$
$$M_z^{eq} = M_0 \tag{2.17}$$

,
which easily show that the effect of the static field is precession of the net magnetization M_0 about B_0 at the Larmor frequency, visualized below in Fig. 2.5.

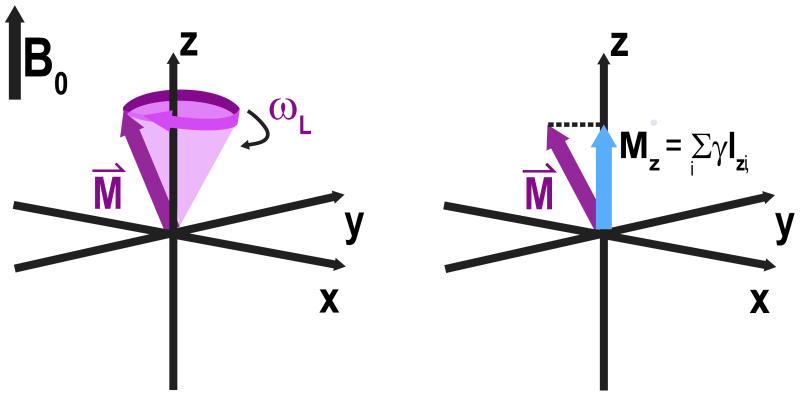

Figure 2.5: In the Bloch-McConnell vector model, the effect of a static external field B_0 is to create net nuclear magnetization in the direction of B_0, typically set in the z-direction. This magnetization precesses around B_0 with frequency ω_L and z-component M_z upon which RF pulses act in an NMR experiment.

If the ensemble is perturbed, it will return to its thermal equilibrium magnetization over time through relaxation.

2.2.2 Excitation

In an NMR experiment, an RF excitation pulse that is on resonance with the Larmor frequency and normal to the external field effectively rotates the net magnetization away from equilibrium (Fig 2.6).

In the case of $B_0 \parallel \hat{z}$, the RF field is effectively circularly polarized in the xy-plane so that the B-component of its EM field is rotating around the $\hat{z}$ direction in the same sense as the Larmor precession of the nuclei with strength B_1. Thus, an RF field applied at the Larmor frequency ω with amplitude B_1 (or ω_1) along $\hat{x}$ adds additional B-field components:

$$B_x = B_1 cos(\omega t) \qquad B_y = B_1 sin(\omega t) \qquad B_z = B_0$$

If one moves to a coordinate plane that is also rotating at ω_0, then spins precessing at ω_0 will appear to not rotate, and the RF pulse appears as a static B_1 field along $\hat{x}$ (Fig. 2.6). Any Larmor precession that is observed after application of this rotating frame of reference

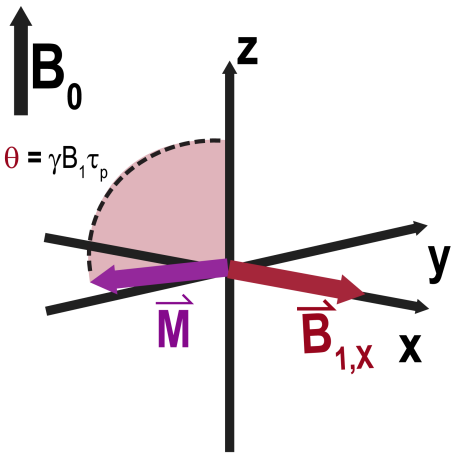

Figure 2.6: In the Bloch-McConnell vector model, the effect of a static external field B_0 is to create net nuclear magnetization in the direction of B_0, typically set in the z-direction. This magnetization precesses around B_0 with frequency ω_L and z-component M_z upon which RF pulses act in an NMR experiment.

represents an effective precession frequency caused by local magnetic field effects and is given by:

$$\omega_{eff} = \omega_0 + \Omega \tag{2.18}$$

where Ωis the frequency of apparent precession in the rotating frame. Because the RF pulse's B-field is on resonance with the Larmor frequency of the spins, z-magnetization begins to precess about $B_{1,x}$ with a frequency $\omega_1 = \frac{\gamma B_1}{2\pi}$. The degree to which the net magnetization of the spins is rotated θ is dependent upon the pulse field strength (B_1) as well as its duration (τ_p):

$$\theta = \omega_1 t_p = \gamma B_1 \tau_p \tag{2.19}$$

If $\theta = 90^o$, the net magnetization is tipped fully into the xy-plane, and initially,

$$\begin{aligned} M_x &= M_0^{eq} \\ M_y &= 0 \\ M_z &= 0 \end{aligned} \tag{2.20}$$

Once the RF field is removed, the system begins to return to equilibrium and magnetization builds up again along $B_0(\hat{z})$ (Fig. 2.7). The rate at which the magnetization then returns to equilibrium is governed by coupling between it and neighboring fields and spins. Coupling creates local magnetic fields of varying strength and frequency that can, much like the excitation pulse, induce rotation of the perturbed spins and affect their precession frequencies:

$$\omega_{eff} = \gamma(1+\sigma)B_0 \tag{2.21}$$

where σ is the chemical shielding parameter, which quantifies the change in total effective magnetic field resulting from the influence of proximal magnetic fields. Naturally, local fields

that oscillate at or near to ω_0 will be more effective at rotating it. These slight differences in precession frequency from spin to spin in the ensemble causes dephasing of the net magnetization over time, which is called spin-spin, or transverse relaxation (R_2). Chemical exchange processes, such as exchange of a labile proton between a carboxylic acid and bulk water, also contributes to dephasing and R_2. This means that there may yet be non-zero magnetization in the transverse plane, but its vectors are distributed evenly and thus it zeroes out. The return of magnetization to the +z direction, specifically, is governed by spin-lattice, or longitudinal relaxation (R_1).

R_1 requires on-resonance perturbations that cause changes of the spin state affecting z-magnetization, which can be visualized as rotation of the net magnetization vector back toward the z-direction, whereas any fluctuations in magnetic fields result in R_2, so at high B_0, R_2 is always faster than R_1 unless molecular motion is very fast ($\geq 10^{12} Hz$).

R_2 and R_1 cause the amplitudes of both transverse and longitudinal magnetization to change over time in the following ways:

$$\begin{aligned} \frac{dM_x}{dt} &= \gamma(M_y B_z - M_z B_y) - \frac{M_x}{T_2} \\ \frac{dM_y}{dt} &= \gamma(M_z B_z - M_x B_z) - \frac{M_y}{T_2} \\ \frac{dM_z}{dt} &= \gamma(M_x B_y - M_y B_x) - \frac{M_z + M_0}{T_1} \end{aligned} \tag{2.22}$$

where $T_2 = \frac{1}{R_2}$ and $T_1 = \frac{1}{R_1}$. After the RF pulse stops, and assuming all the magnetization has been rotated into the transverse plane (re: Eq. 2.20), only the B_0 external field remains such that the magnetization components, with relaxation terms applied, become:

$$\begin{aligned} \frac{dM_x}{dt} &= \gamma(M_y B_0) - \frac{M_x}{T_2} \\ \frac{dM_y}{dt} &= -\gamma(M_x B_0) - \frac{M_y}{T_2} \\ \frac{dM_z}{dt} &= -\frac{M_z + M_0}{T_1} \end{aligned} \tag{2.23}$$

It becomes clear that the effect of R_2 relaxation is to diminish transverse magnetization over time, while R_1 governs the rate of replenishment of equilibirum z-magnetization (see Fig. 2.7 for a visualization of this effect).

The solutions for $M_x(t)$, $M_y(t)$ in Eq. 2.23, from which the NMR signal is derived, and $M_z(t)$ are as follows:

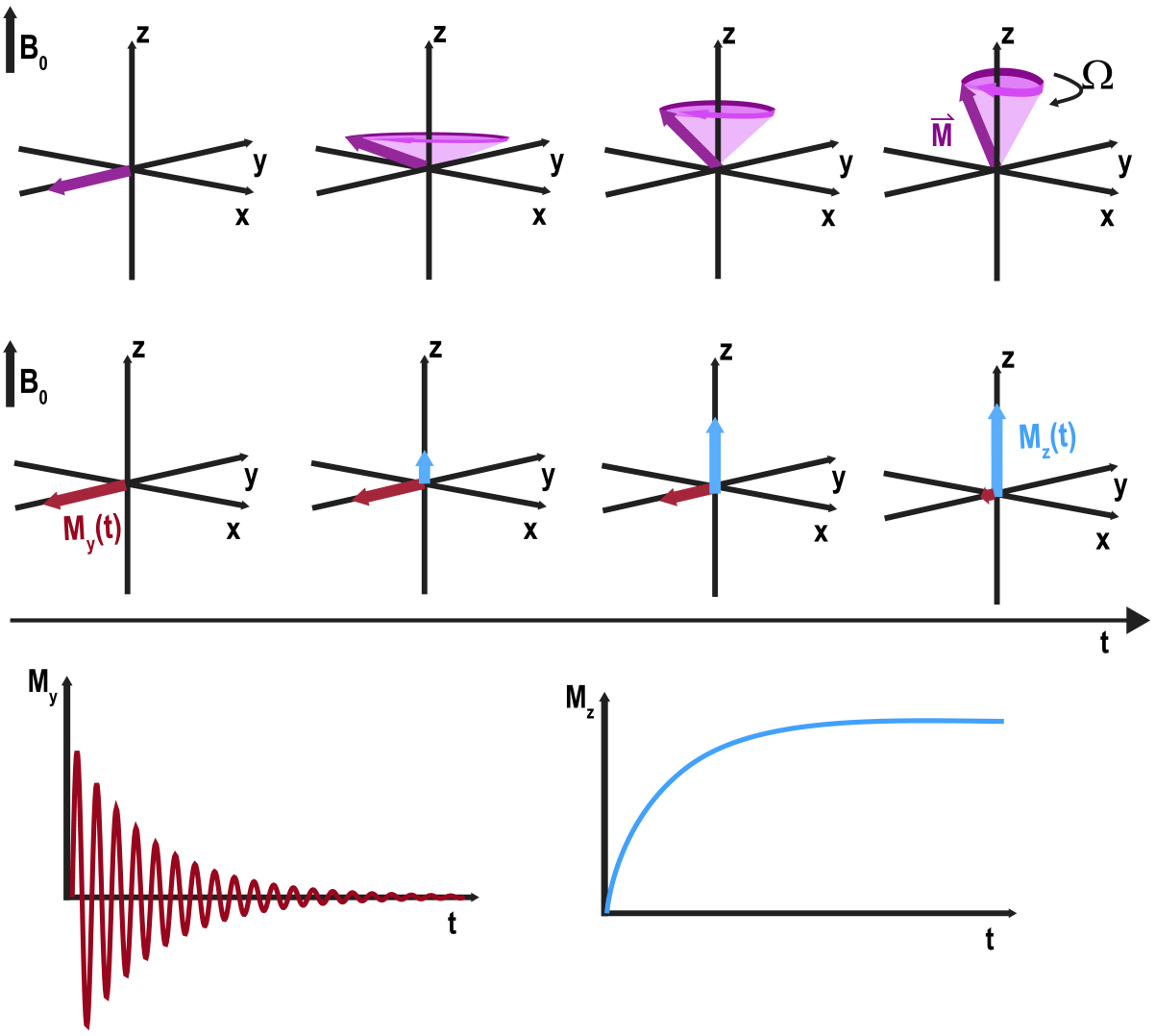

Figure 2.7: Just after an on-resonance, 90_x^o RF pulse, all magnetization is placed in the transverse plane. The magnetization continues to precess about B_0 with frequency Ω, corresponding to the offset from the Larmor frequency caused by local magnetic fields. Eventually, all transverse magnetization has decayed and equilibrium is regained. During relaxation, the change in transverse magnetization over time (bottom left, M_y shown) is observed as exponentially decaying sine function, with a decay rate governed by R_2. Meanwhile, equilibrium magnetization is recovered over time (bottom right) at a rate determined by T_1.

$$M_x(t) = [M_x cos(\gamma Bt) - M_y(0) sin(\gamma Bt)]e^{-\frac{t}{T_2}}$$

$$M_y(t) = [-M_x sin(\gamma Bt) + M_y(0) cos(\gamma Bt)]e^{-\frac{t}{T_2}} \tag{2.24}$$

$$M_z(t) = M_0[1 - e^{-\frac{t}{T_1}}] \tag{2.25}$$

Recall that at time zero after the RF pulse, the magnitude of the transverse magnetization is M_0^{eq}, which simplifies $M_x(t)$ and $M_y(t)$ to:

$$M_x(t) = M_0^{eq} cos(\gamma Bt - \phi_0) e^{-\frac{t}{T_2}}$$
$$M_y(t) = -M_0^{eq} sin(\gamma Bt - \phi_0) e^{-\frac{t}{T_2}} \quad (2.26)$$

where the angle between M_0^{eq} and the x-axis $\phi_0 = 0^o$ at time zero. It should be noted that the Bloch equation solutions do not provide easy incorporation of scalar, dipolar and quadrupolar coupling interactions, for which quantum mechanical treatment is required (and provided in Chapter 9).

2.2.3 Detection

Spins continue to precess about B_0 at their Larmor frequencies as they return to equilibrium, inducing an oscillating current in resonantly tuned LC circuits as they do so in a process called free induction. These circuits pick up only the transverse components of the precessing magnetization, M_x and M_y. The signal disappears as magnetization in the xy-plane decays and equilibrium magnetization builds up again along B_0 (Fig. 2.7).

The detected signal takes the form of a free induction decay (FID), and is described by an exponentially decaying function that contains both time-varying magnetization components derived above (2.26):

$$S(t) = S_0 e^{i\Omega t} e^{-\frac{t}{T_2}} \quad (2.27)$$

Where S_0 is the overall size of the signal (which is proportional to M_0 and the degree of rotation proffered by the RF pulse), and Ω is the frequency offset from Larmor precession caused by local magnetic fields ($\Omega = \omega_{eff}$- ω_0). Because it is much more rapid, R_2 dominates the decay of the FID. When the ensemble is fully returned to equilibrium, the net magnetization is no longer observable by the system without further perturbation.

2.2.4 Signal processing

The weak signal picked up by the resonantly tuned circuits is first passed through the duplexer into a preamplifier that scales up the NMR signal to a more easily handled voltage. Once preamplified, the signal is passed through a quadrature receiver for digitization. The receiver first down-converts the analog signal from MHz to kHz in order to bring it within the range of (and avoid overloading) the analog-to-digital converter (ADC) by subtracting from it a reference frequency $\omega_{ref} = \omega_0$.

Then, in order to resolve ambiguity of spins precessing slightly faster or slower than ω_0, the quadrature receiver separates the signal into real and imaginary parts, where the signal from

x-magnetization comprises the real part and the y-magnetization makes up the imaginary portion, yielding a complex signal of the form $S(t) = S_x(t) + iS_y(t) \propto M_x(t) + iM_y(t)$.

Each component of the complex signal has its own ADC that rapidly measures the voltage level of an input signal and presents the information as binary strings.The rate at which the ADC samples the signal for digitization is the inverse of the dwell time, and also determines the sampling bandwidth and spectral width.

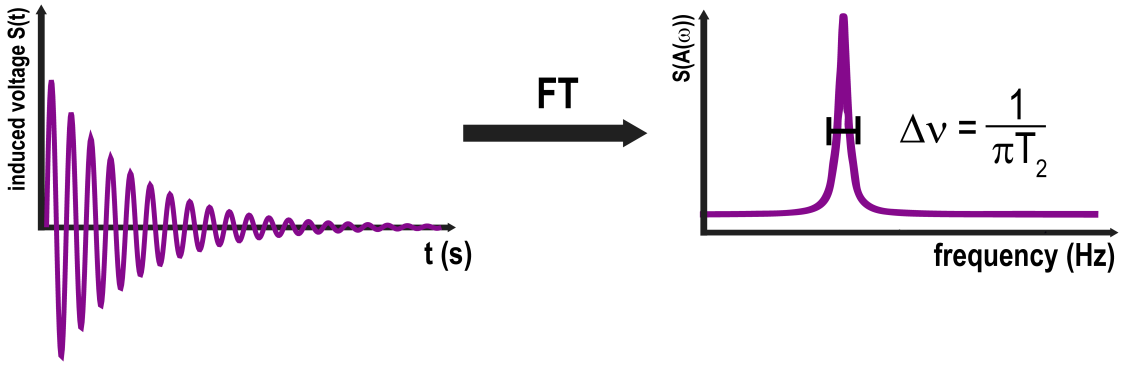

Figure 2.8: Fourier Transformation of a FID yields a NMR spectrum whose real component is comprised of absorptive lineshapes centered at each precession frequency observed in the FID with widths determined by their respective transverse relaxation rates.

The sampling bandwidth sets the maximum range of sampling frequency that can be accurately represented by the ADC sampling process, e.g. ≈ 250 kHz for liquids NMR or $\approx$ MHz for solid state NMR. The acquisition time is determined by the number of points sampled and the sampling dwell time: $\tau_{at} = n_{sample} \cdot \tau_{sample}$

The signal can be further processed by phasing/apodization, zero-filling and more, which will be discussed later in this chapter. Finally, the time-domain signal is Fourier transformed into a frequency-domain function whose real and imaginary components yield absorption and dispersion Lorentzian lineshapes:

$$S(\Omega) = \omega_1 M_0[A(\Omega) + D(\Omega)]$$
$$A(\Omega) = \frac{T_2^2\Omega}{1 + (T_2\Omega)^2} \qquad D(\Omega) = \frac{T_2}{1 + (T_2\Omega)^2} \tag{2.28}$$

The absorptive component yields a spectrum with Lorentzian lines centered at the various effective precession frequencies of the population (Fig. 2.8) and whose widths are largely determined by their relaxation rates ($FWHM \approx (\pi T_2)^{-1}$). An example of a spectrum comprised of multiple frequencies is shown in Fig. 3.2. As relaxation rates increase, so does peak width. The area under a given peak is independent of linewidth, so as a line broadens, its

intensity will decrease. For a more involved discussion involving the effects of coupling and relaxation on an NMR spectrum, the reader may refer to a number of exemplary texts on this complex and elegant subject.[23–26]

2.3 Technical Considerations

A few important parameters for NMR signal processing (acquisition time, sampling rate, spectral bandwidth) were discussed above but are certainly not comprehensive. This section seeks to provide awareness of some of the most imperative acquisition parameters, while more in depth discussion of NMR signal acquisition and manipulation can be found elsewhere.

2.3.1 Frequency offset

The spectral window, for sample, is set not only by the spectral bandwidth mentioned above but also where that range is centered. The center of the spectrum is set by varying the transmitter frequency[1]. For Agilent, Varian and Bruker consoles, this value is changed by setting both the major transmitter frequency (in MHz) and the amount of offset from the transmitter frequency (in Hz, called o1 for Bruker and tof for Agilent/Varian instruments). For example, for a ^{129}Xe NMR experiment using a 9.4 T magnet, one may set the transmitter frequency 110 MHz (roughly the Larmor frequency for ^{129}Xe at 9.4 T). Without an offset, the spectrum will be centered at 110 MHz (0 ppm). If the offset is set to 20 kHz, the spectrum will have the same bandwidth, but will now be set to 110 MHz + 20 kHz, corresponding to about 200 ppm. Knowing this is important because a pulse is strongest at its center frequency, so a relatively weak signal can be found and amplified with an appropriately set spectral window.

2.3.2 Repetition rate

The rate of recovery of magnetization to equilibrium along the z-axis is given by the solutions to Eq. 2.23 for M_z,shown below, with charcteristic time constant T_1:

$$M_z(t) = M_0[1 - e^{-\frac{t}{T_1}}] \tag{2.29}$$

From this equation, one finds that $1 - e^{-5}$ is ≈ 0.99, which is why many spectroscopists will say that a delay of $5T_1$ (where the T_1 of the longest-lived resonance is used) is sufficient enough a delay between RF pulses for the magnetization to recover. Often, a compromise must be made in the interest of time, where not all resonances are able to fully relax before an experiment is repeated. In this case, a spectrum will still be returned, but the integrated areas of some resonances may be off, which is important when structure determination or

[1] Also known as the carrier frequency or transmitter offset

concentration measurements are the goal.

One way to get around long relaxation times is to add relaxation agents, such as O_2 or paramagnetic metal ions, that cause equilibrium magnetization to recover more quickly at the cost of linewidth. Another work-around is to use pulses with tip angles smaller than 90^0 at the cost of some SNR. The relaxation rates aren't effectively changed, but the time required for magnetization to recover is reduced since it was less perturbed to begin with. Additionally, phase cycling, or alternating the phases of the RF pulse and receiver between transients, can help reduce effects of short repetition rates such as direct current offsets in the receiver and residual transverse magnetization. Lastly, small, short-term 'homospoil' pulses can be applied prior to the relaxation delay to dephase and thus eliminate residual x- and y-components of magnetization. These are small gradient fields produced either through the room-temperature Z1 shim or through a gradient coil in the probe itself. The latter sort of probe is called a PFG, or pulsed field gradient probe.

It's important to note that the relaxation delay is not the same as the acquisition time. Because the NMR signal is governed by T_2, not T_1, the FID signal often decays much more quickly than equilibrium magnetization recovers. Recording data for the length of $5T_1$ would only result in the acquisition of a lot of noise, which would translate to the NMR spectrum. As with the recovery of equilibrium magnetization, the depletion of transverse magnetization is described by an exponential decay:

$$M_{x,y}(t) \approx M_0 e^{-\frac{t}{T_2}} \tag{2.30}$$

Similarly, then, 99% of the transverse magnetization disappears within $5T_2$. However, a lot of the time, inhomogeneities in the external field due to poor shimming cause a shorter apparent relaxation time, $\frac{1}{T_2*} = \frac{1}{T_{2,inhom.}} + \frac{1}{T_2}$, where T_2 is the inherent relaxation time of the chemical species, and $T_{2,inhom.}$ is the contribution from field inhomogeneity. Because of this, acquisition times for a simple pulse-acquire experiment must be made even shorter and reflective of T_2*.

2.3.3 Zero filling

The digital resolution of a spectrum corresponds to how many frequencies (in Hz) are associated with one data point. Finer digital resolution means less space between points on an NMR spectrum, and thus smoother lines. Digital resolution can be improved with zero-filling, which is accomplished by literally adding a long string of zeroes to the dataset until its size matches the next power of two. Adding more points to the dataset, even if they are just zeroes, will force resolution in Hz/pt to become finer if the spectral width is kept the same. Zero-filling to double or quadruple the size of a dataset is common practice in modern NMR.

2.3.4 Apodization

Another way to circumvent artifacts resulting from stopping acquisition before magnetization has fully decayed (truncation) is to apply a function that acts as a 'window' through which the signal appears to decay to zero before it is digitized. This is accomplished by apodization, or multiplying the FID by a function, most commonly Gaussian, exponential or various sine bell functions. This process helps to avoid truncation artifacts, most typically presenting as 'ringing' on either side of the resonances in the spectrum. Meanwhile, the use of some apodization functions (e.g. sine bells) can be used to resolve small peaks shouldering on larger resonances at the cost of overall SNR as initial parts of the FID are cut off in this case.

2.3.5 Phase correction

As mentioned earlier, after being separated, both components of the complex NMR signal are passed through individual ADCs so that net magnetization precessing in different senses relative to the rotating frame (the reference frequency) can be distinguished. During this process, and in the delay between the RF pulse and acquisition, signals can become out of phase with one another, causing resonances on the spectrum to have both absorptive and dispersive characters. Phase correcting the spectrum ensures that all observed resonances are absorptive. Usually, zero- and first-order phase correction address these issues sufficiently. Zero-order phase correction assists with the first problem, wherein the variation in the proportion of amplitude data taken from the two orthogonal receivers is corrected by applying a consistent amount of phase offset to each point in the spectrum.

First-order phase correction helps with phase errors resulting from pulse ringdown delays by applying a linearly varying amount of phase offset to each resonance along the spectrum, because, in this case, a resonance that is not far off-resonance will require less correction than one that is.

2.3.6 Baseline correction

Baselines that are not flat are the result of a variety of instrumental and experimental hobgoblins (with some positing Maxwell's demons), ranging from ringdown effects to acoustic contamination. Baseline correction algorithms help to make spectra more easily interpretable and come standard with most processing software, however the important message about baseline correction is that it must be used judiciously. Without careful examination, very broad resonances due to quickly exchanging species or miniscule satellite peaks can be deleted by baseline correction algorithms. A correction that requires manual input for what is and is not the spectral baseline is best.

2.3.7 Pulse ringdown times

Pulses and gates are not perfect, and so both ringup and ringdown times exist before pulses reach a constant amplitude. The higher the pulse power, the longer the ringdown time. Pulse ring-down can corrupt the first few points in a FID causing pulse artifacts at the center of the spectrum or seemingly infinitely narrow but large resonances poppping up about the spectrum. One can preclude these effects a couple ways. A short delay can be imposed between pulsing and acquisition, but this can be hard to calibrate without losing valuable signal attributed to short-lived species and sacrificing accurate integration information. One can also discard the first few points of the FID and use backward linear prediction to refill them.

2.4 Polarization

Unfortunately, the source of inherent insensitivity in NMR and MRI is in part what makes it so safe a diagnostic technique: the low-energy RF pulses used to generate contrast excite transitions between Zeeman levels of protons, but the energetic difference between these states is so small that ambient thermal energy is sufficient to cause spins to be almost equally distributed between those states. The intensity of an NMR signal scales with the population difference, or polarization, of the Zeeman levels, which is derived from a Boltzmann distribution:

$$P = \frac{N_+ - N_-}{\sum N} \propto e^{-\frac{\Delta E}{k_B T}} \tag{2.31}$$

where k_B is 1.3805x10^{-23}J/K, which can be simplified to

$$P = tanh(\frac{\frac{1}{2}\mu_B B}{k_B T}) \tag{2.32}$$

and $\mu = \gamma I = \pm\frac{\gamma}{2}$ for protons. This amounts to only a few ppm for protons at 1.5 T. The goal of hyperpolarization techniques such as that explored in the next chapter is thus to improve sensitivity by maximizing P.

Chapter 3

Hyperpolarized ^{129}Xe NMR

Utilization of conventional magnetic resonance techniques for biosensor applications may be limited by the intrinsically low sensitivity and the complexity of spectra obtained from biomolecules and mixtures. Hyperpolarized ^{129}Xe NMR is an appealing alternative to conventional NMR and MRI techniques that yields practical detection limits of small biological targets without the risks associated with ionizing radiation.[27,28] ^{129}Xe nuclei can be hyperpolarized by spin exchange optical pumping (SEOP) such that signal is sufficiently increased to enable detection of analytes at biologically relevant (milli- to picomolar) concentrations. This chapter will explain why ^{129}Xe NMR as is so promising a modality for molecular sensing. First, an overview of some of the physical properties of xenon and principles of ^{129}Xe NMR are provided. The generation of hyperpolarized xenon by SEOP is described both in theory and practical application. Finally, the application of macrocyclic xenon hosts for molecular detection is reviewed.

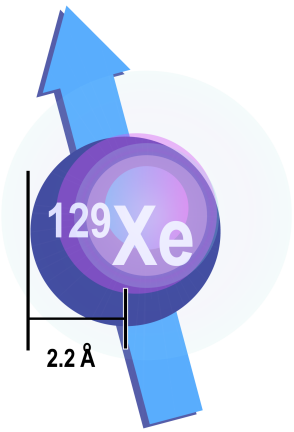

Figure 3.1: A xenon atom!

3.1 Xenon: L'Etranger

The name 'xenon' comes from the Greek *ξένος (xenos)*, meaning stranger, or guest, alluding to both its curious history and its role in this modern work. In 1898 Ramsay and Morris performed a fractional distillation of liquid air, slowly evaporating off its components over time. Within the remaining residue, they revealed a mysterious element that yielded the previously unknown but now characteristic bright blue spectroscopic lines associated with xenon.

Intriguingly, distillation from air remains the primary method by which xenon is isolated from air for industrial and research use. It naturally exists at 87 ppb in Earth's atmosphere

and is odorless and colorless. Being a fifth period noble gas, xenon is quite large, possessing a van der Waals radius of $\approx 2.2\,\text{Å}$. It is largely inert and hydrophobic, as a stable octet valence electron configuration provides that it cannot easily participate in interactions requiring dipole moments, though some notable xenon halides, oxides and even hydrides have been synthesized.

At atmospheric pressure and temperature, xenon exists as a dense gas ($5.8\ \frac{kg}{m^3}$). Its liquid phase is highly polarizable, allowing the dissolution of organics, biomolecules and water, however, the temperature range of liquid xenon is small: it freezes at 161 K and boils at 165 K.

Xenon has many interesting uses in fields ranging from astrophysics to medicine. It can be found in flash lamps for cameras and car headlights, as a propellant for modern spacecraft ion thrusters, to detect weakly interacting massive particles thought to comprise dark matter, and as a breathable general anesthetic. Many surmise that its utility as an anesthetic has to do with its ability to dissolve in lipid layers of tissue and disrupt certain transmembrane mechanisms and by binding to hydrophobic pockets in and inhibiting enzymes.[29] Compared to nitrous oxide, it is 44% more potent as an anesthetic, meaning it can be used in lower concentrations with oxygen to reduce risk of hypoxia.[30]

3.2 Xenon NMR

Xenon has eight stable isotopes, and nearly fifty unstable isotopes that undergo radioactive decay. Isotopic ratios of xenon are often used to study the early history and massive content of the solar system. Of its stable isotopes, there are only two, ^{129}Xe and ^{131}Xe, that can be used in NMR spectroscopy. ^{129}Xe has a nuclear spin of $\text{I} = \frac{1}{2}$ and 26.4 % natural abundance, and ^{131}Xe has a nuclear spin of $\frac{3}{2}$ and 21.2 % natural abundance. Both isotopes are very sensitive to changes in local chemical environments due to the high polarizability of their large stock of valence electrons: these electrons reside far enough from the nucleus that their spatial distributions can fluctuate in response to passing charges to produce transient polarity (i.e. weak induced dipoles) in the atom to which the nuclear spin can couple.

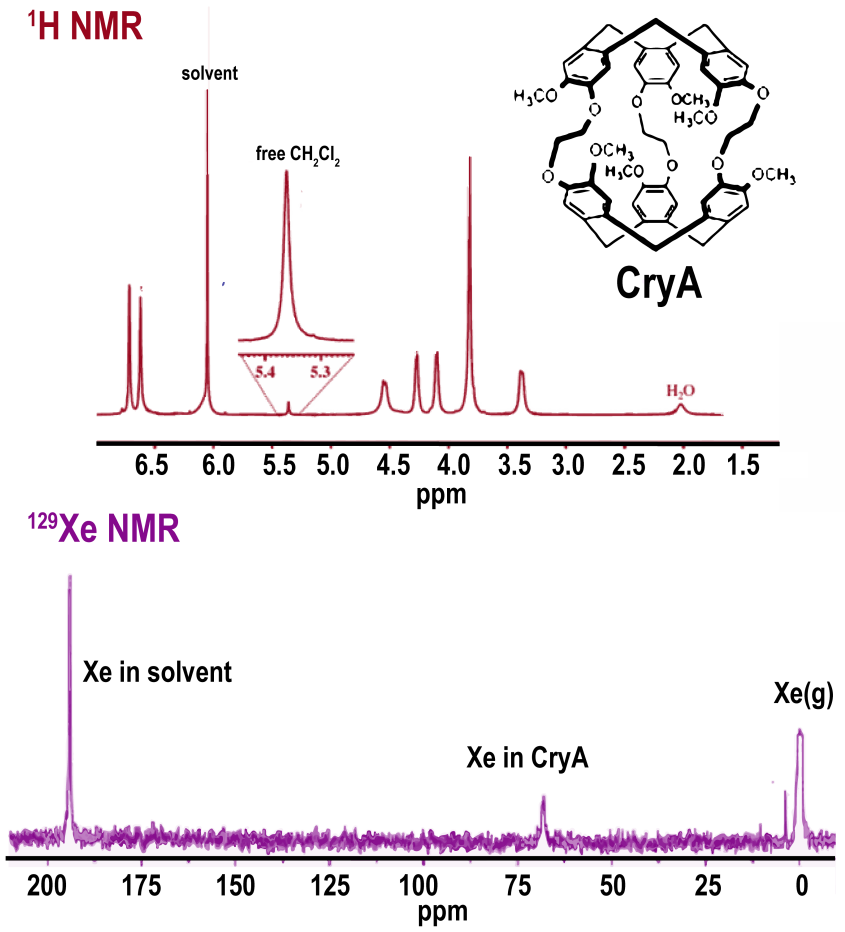

Figure 3.2: ^{1}H (top) and ^{129}Xe NMR (bottom) spectra for the analysis of the molecule Cryptophane-A (CryA) ^{1}H spectra are much more complicated with a much smaller chemical shift range than ^{129}Xe spectra. In the above ^{1}H spectrum, there is no xenon present. When xenon is added, the atoms exchange in and outside of the cage-like CryA slowly enough to provide a unique single resonance on the ^{129}Xe NMR spectrum.

This polarizability is both the reason for xenon's chemical shift sensitivity in NMR as well as its appreciable solubility in water despite being an ideal hydrophobe.[31]

Because xenon atoms do not generally participate in covalent bonds with each other or other atoms, xenon NMR spectra are less complex than those from ^{1}H or ^{13}C NMR, usually showing only a few, easily interpretable lines corresponding to unique chemical environments (Fig. 3.2). Despite its spectral simplicity, xenon exhibits the important property that it can sensitively report on its local environment via its chemical shift and relaxation parameters. For example, the range of xenon chemical shifts corresponding to non-specific interactions in various liquids is greater than 250 ppm, compared to 10 ppm for ^{1}H NMR. A depiction of notable xenon chemical shifts in such environments can be found in Figure 3.3. Lastly,

being inert, xenon does not alter or destroy any of the samples with which it interacts.

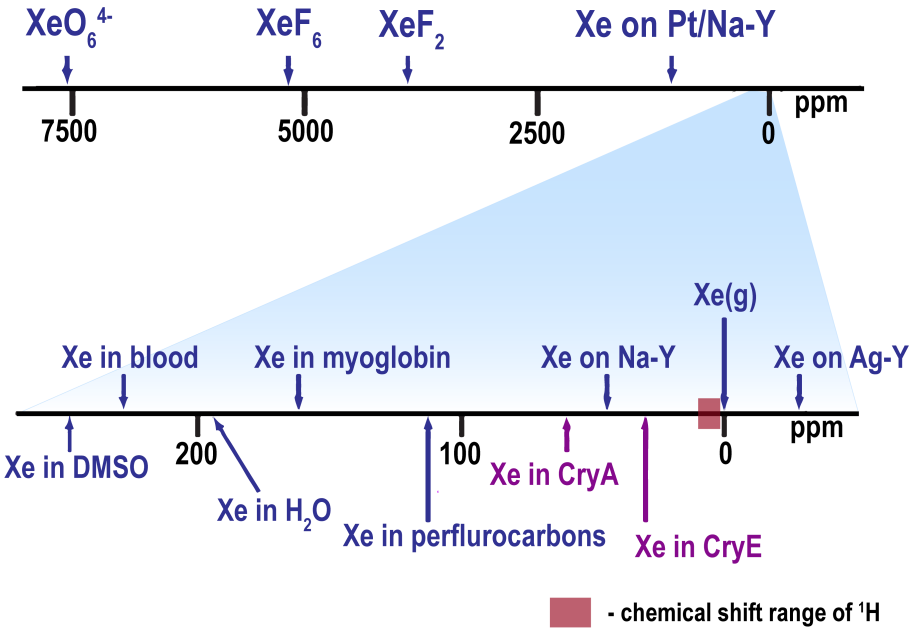

Figure 3.3: ^{129}Xe has an incredible chemical shift range owing to its high electron polarizability, especially compared to ^{1}H NMR. A few xenon molecules have been probed, but non-covalently bound Xe has been used most extensively to characterize liquids, material surfaces and porosity, liquid crystal and plastic phase transitions, and more. Typically, ^{129}Xe spectra are referenced to gas-phase xenon at 0 ppm, with most biorelevant samples falling within the 0-220 ppm range.

For the most part, literature has focused on using xenon chemical shifts to probe porous materials, clathrates and protein cavities for the purpose of quantifying such properties as pore or cavity size and structure, atomic orientations, order, gas diffusion and adsorption, and chemical composition.[32–38] In most cases, xenon gas exchanges slowly enough to have unique chemical shifts for captured xenon vs free xenon.

Although ^{131}Xe can be used to derive physical properties like orientations of atoms in porous or crystalline structures, it possesses a quadrupolar moment (as does any nucleus of spin $> \frac{1}{2}$) that gives rise to extremely high relaxation rates and line broadening that are unfavorable for biological studies, wherein the samples probed are already chemically and magnetically complex. ^{129}Xe is thus the preferred isotope for any biorelevant Xe NMR work. Indeed, the application of ^{129}Xe NMR to medical imaging has led to the advent of a revolutionary type of lung and sinus imaging that doesn't succumb to the same susceptibility and void space

issues that face conventional ^{1}H MRI.[28,39]

However, many enticing biological targets reside in complex liquid environments, such as blood, saliva and mucus. Xenon is most soluble in organics, but, as previously mentioned, its high electron polarizability gives it an appreciable solubility in water. At standard temperature and pressure, mM concentrations of xenon can be attained in water. This value will decrease at higher temperatures (such as those associated with *in vivo* studies), but increases with pressure. At 37°C (body temperature) and 60 psi (≈4 atm), we can expect concentrations of 0.35-0.91 mM ^{129}Xe if using 2-5 % Xe sources and nearly 20 mM if using isotopically enriched xenon in aqueous samples.

Xenon dissolved in liquids has been used to probe hydrophobic pockets in proteins, lipid rafts, micelles, phase separations, liquid crystal phase transitions, and more.[15,16,40] However, low thermal polarization and long spin-lattice relaxation leads to experimental averaging that can require times of hours to days, inhibiting practical diagnostic screening using this technique. Happily, laser polarization of ^{129}Xe magnetization using spin exchange optical pumping, detailed in the next section, has enabled single-shot measurement of dissolved xenon populations, expanding potential applications of this technique to monitoring of dynamic chemical processes and decreasing the cost involved with using xenon sources.

3.3 Xenon Hyperpolarization through Spin Exchange Optical Pumping

Spin exchange optical pumping, or SEOP, is just one of many clever scientific approaches that exploit a more easily (and affordably) attainable state to accomplish a technically difficult feat. In this case, the facile polarization of electronic spin states of rubidium using optical pumping with resonant photons enables the polarization of xenon nuclear spin states via collisional mixing between thermally polarized Xe and Rb atoms. If all experimental considerations are optimally balanced, the polarization of xenon is roughly proportional to the rubidium polarization in the cell. Therefore, it is important that a Xe NMR user knows how to optimize rubidium polarization. This section describes both Rb polarization and spin exchange from a theoretical perspective, followed by a description of the physical phenomena that contribute to the efficacy of polarization. The next section will discuss how to optimize both processes in practice.

3.3.1 Setting the State: Rubidium Spin States

Rubidium, like all alkali metals, has one valence electron of spin S = $\frac{1}{2}$ that sits in an s orbital (l = 0) in its ground state, denoted as $^{2}S_{\frac{1}{2}}$ in spectroscopic notation, and a p orbital (l = 1) in its first excited state. Promotion into the p shell leads to splitting of the energy levels into the $^{2}P_{\frac{1}{2}}$ and $^{2}P_{\frac{3}{2}}$ states with respective total angular momentum J = $\frac{1}{2}$ and J = $\frac{3}{2}$.

Both excited states have multiplicity of 2 owing to degenerate m_j sublevels. The energetic structures of these levels are shown in Fig. 3.4. Transitions between the $^2S_{\frac{1}{2}}$ ground state and the $^2P_{\frac{1}{2}}$ and $^2P_{\frac{3}{2}}$ excited states are known as the D1 and D2 transitions, respectively.

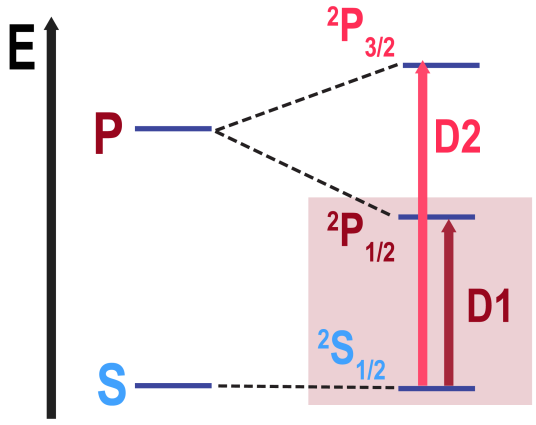

Figure 3.4: [129]Energy levels of the ground and first excited state of a rubidium atom (not drawn to scale). The first excited state splits into J=1/2 and J=3/2 due to fine structure introduced by the addition of orbital angular momentum the p shell. They can be visualized as states with the orbital and spin angular momenta laying either parallel (J=3/2) or anti-parallel (J=1/2). The transitions between the $^2S_{1/2}$ ground state and the $^2P_{1/2}$ and $^2P_{3/2}$ excited states are termed the D1 and D2 transitions, respectively.

The majority of alkali metals also have non-zero nuclear spin lending hyperfine structure to their atomic energy levels due to coupling, but the energy differences between them are so small that in systems relevant to this work they can be effectively treated as though they were degenerate.

If the rubidium atoms are placed in an external magnetic field, the degeneracy of the m_j states is broken and they split into Zeeman levels as described in Chapter 2, but with electron spin states instead of nuclear spin states. This splitting leads to the energy level structure shown in Fig. 3.5, which becomes the playing field for optical pumping.

3.3.2 Pumping the D1 Transition

In our case, the type of optical pumping used is depopulation pumping with circularly polarized light at the resonant frequency of the Rb D1 transition. The D1 transition is chosen over the D2 transition because the former has the potential to generate unity polarization. The D2 transition, on the other hand, can at best reach 50% polarization in our systems due to the presence of requisite buffer and quenching gases.

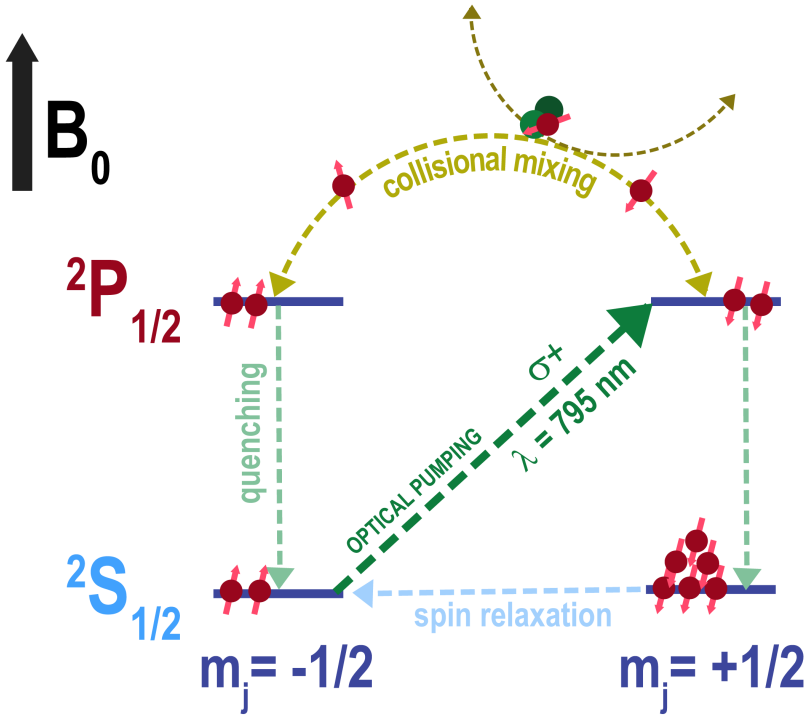

Figure 3.5: Optical pumping of the D1 transition of a rubidium electron with σ+ polarized light at 795 nm. Because of the circular polarization of the incident beam, only atoms in the m_j=-1/2 sublevel can be promoted to the excited state. Atoms mix between the Zeeman sublevels of the excited $^2P_{1/2}$ states due to collisions with buffer gases. Atoms relax to the $^2S_{1/2}$ ground states with equal probabilities. Atoms in the m_j = -1/2 level can immediately absorb another photon, but those in the m_j = +1/2 sublevel cannot. Although atoms can further relax from the $^2S_{1/2}$ m_j = +1/2 Zeeman level to the m_j = -1/2 level, the m_j = +1/2 sublevel is populated by optical pumping much more quickly than it is depleted.

Circular polarization restricts the spin projection of incident photons as either along ($+\sigma$) or against ($-\sigma$) the axis of light propagation. Photons of $+\sigma$ polarization lend +1 unit of electron spin angular momentum. If we have a $+\sigma$ polarized photon, a spin in the $^2S_{\frac{1}{2}}$ ground state $m_j = -\frac{1}{2}$ sublevel can absorb the photon's angular momentum and be promoted to the $m_j = +\frac{1}{2}$ sublevel of the $^2P_{\frac{3}{2}}$ excited state. A spin in the $m_j = +\frac{1}{2}$ sublevel cannot absorb angular momentum from $+\sigma$ polarized photons due to selection rules (there is no excited state with m_j angular momentum of $+\frac{3}{2}$. Thus, while electrons of $m_j = -\frac{1}{2}$ are being depleted from the ground state while electrons of $m_j = +\frac{1}{2}$ are stuck in the ground state.

3.3.3 Polarization Build-up

Once promoted to the $m_j = +\frac{1}{2}$ level of the $^2P_{1/2}$ state, an electron spin can either relax back into either of the m_j levels of the ground state, or they can jump to the $m_j = -\frac{1}{2}$ level of the excited state via collisional mixing. Strong coupling between the excited state electrons and the rotation of the complex formed during collisions lead to a roughly equal population

distribution in the excited states.

Spins in either excited state can relax back into both m_j ground states, but spins the $m_j = +\frac{1}{2}$ state are confined to it since the $+\sigma$ polarized light cannot excite them. Therefore, there is a preferential build-up of spins in the $m_j = +\frac{1}{2}$ state, leading to spin polarization.

Of course, there are also relaxation mechanisms that result in depolarization. Spins in the $m_j = +\frac{1}{2}$ ground state relax back into the $m_j = -\frac{1}{2}$ ground state and relaxation from either excited state results in the emission of resonant photons of arbitrary sign of angular momentum, which leads to depletion of the $m_j = +\frac{1}{2}$ state. Collisions with the rubidium cell wall and other atoms also deplete polarization.

The amount each of these processes contributes to the total optical pumping rate can be modulated by the density of rubidium vapor and presence of additional buffer and quenching gases in the rubidium cell, which is discussed in detail elsewhere.[41] Without quenching and buffer gases, excited state spins relax twice as quickly into the $m_j = -\frac{1}{2}$ ground state compared to the $m_j = +\frac{1}{2}$ state. With the proper balance of quenching and buffer gases contributing to collisional mixing, the probability of decaying into either m_j level of the ground state becomes equal, leading to an increased polarization rate. A recommended expanded theoretical view of polarization rates can is found in Seltzer(2008),[41] while some practical experimental guidelines are given in Chapter 4.

3.3.4 The Hand-Off: Polarization of Xenon via Spin-Exchange Collisions

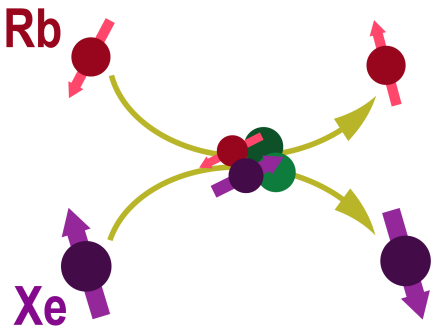

Figure 3.6: In the second part of the SEOP process, xenon atoms undergo momentum-conserving collisions with rubidium atoms in the presence of buffer gases (in this case, N_2). As a result of these collisions, the polarization of rubidium electrons is transferred to xenon nuclei. The buffer gases aid in quenching undesired emission of randomly-polarized photons during collisions.

As xenon gas flows through the rubidium cell, polarization is transferred from rubidium electron spins to xenon nuclear spins through spin-exchange collisions. During these collisions, xenon nuclei couple to the valence electron of rubidium via the Fermi contact interaction, and the electron imparts its angular momentum to the xenon spins (Fig. 3.6). Since the polarization of both spins is flipped, total spin is conserved, but energy is not. As previously

mentioned, N_2 molecules facilitate equal probability of Rb atoms decaying into either ground state by absorbing the randomly polarized photons emitted during collisional mixing. This same phenomenon is present in Rb-Xe spin exchange, as well, and the inclusion of buffer gas allows rapid build-up of hyperpolarized ^{129}Xe nuclei.

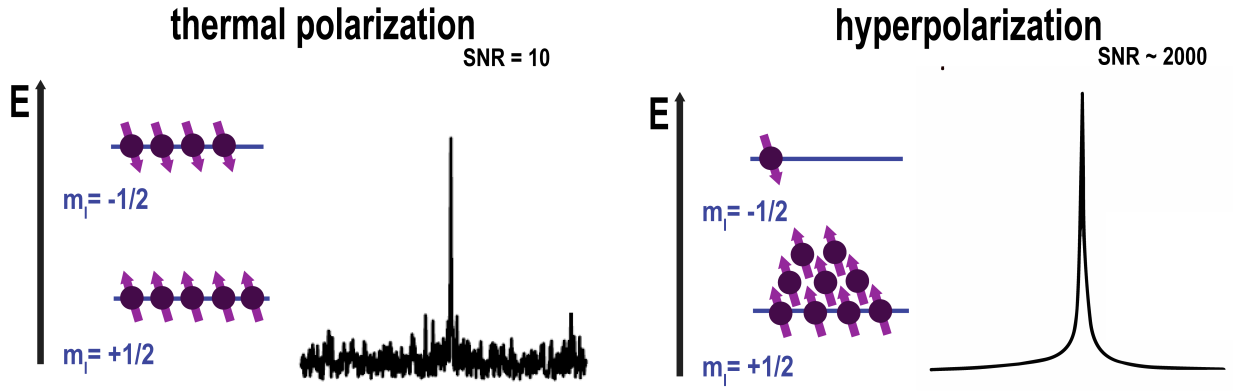

Figure 3.7: Thermal versus hyperpolarized ^{129}Xe NMR spectra. Both are single-shot acquisitions, however the hyperpolarized spectrum was obtained at ten times higher partial pressure of Xe than that of the thermally polarized spectrum.

As with rubidium, so long as the rate of polarization build-up dominates over that of relaxation mechanisms, up to 10% xenon polarization can be achieved, yielding an increase in xenon signal of up to 4-5 orders of magnitude compared to thermal polarization (Fig. 3.7). Once generated, hyperpolarized xenon is delivered to the sample and measured in an NMR probe. Because ^{129}Xe lacks a quadrupole moment, hyperpolarization may persist for many hours in the gas phase, about a minute dissolved in aqueous solutions, and several seconds dissolved in blood. The depolarized rubidium remains in the cell and may be repolarized under continuous laser irradiation.

3.4 Functionalizing Xenon for Molecular Detection using Macrocyclic Carriers

As a noble gas, xenon cannot typically partake in covalent bonding other atoms. This makes functionalizing xenon to detect specific environments or binding events seem impossible. However, xenon atoms can become encapsulated by "host" molecules and engage in non-covalent interactions leading to long enough residence times to be observed as unique chemical environments for ^{129}Xe NMR.[17] If these hosts can instead be functionalized to change magnetically or chemically in the presence of a specific molecular target, then xenon can detect that change while it resides in that host, leading to observable changes in chemical shift or relaxation rates. Such hosts are referred to as xenon biosensors. Xenon hosts of differing molecular structures have unique ^{129}Xe chemical shifts, which are more resolved

compared to ^{1}H or ^{13}C by way of xenon's large chemical shift range. This bolsters the prospect of multiplexing, i.e., the detection of multiple target analytes simultaneously by ^{129}Xe NMR. This section will introduce general host-guest dynamics relevant to Xe biosensing, then present the major families of xenon biosensors. This section will also describe how chemical exchange saturation transfer (CEST) techniques can enhance the detection limits and quantification of these biosensors.

3.4.1 Effect of Chemical Exchange on NMR spectra

As has been exhaustively posited by now, the sensitivity of xenon to its chemical surroundings makes it an appealing probe for complex molecular environments, but there are some constraints on this benefit. If multiple distinct chemical environments exist into which xenon atoms can separate, they will have unique xenon chemical shifts associated with them. However, if xenon can exchange between the different environments, the chemical shift of one environment will be affected by the other. The degree to which the chemical shift of the second environment influences the first is dependent on exchange kinetics and population distribution. Taking the simplest case of two different chemical environments, A and B, between which xenon can exchange,

$$Xe@A \underset{\kappa_{\mathrm{BA}}}{\overset{\kappa_{\mathrm{AB}}}{\rightleftarrows}} Xe@B \tag{3.1}$$

where κ_{AB} and κ_{BA} are the exchange rates of xenon from state A (Xe@A) to state B (Xe@B) and from B to A, respectively.

If a xenon atom exchanges between these different environments too quickly, the result will be broadened or averaged lines in an NMR spectrum. By analogy, if a car drives too quickly past a camera with a given shutter speed, the resulting photo will be a blurry blob, with part of the car on the left side of the frame and part of the car on the right; it is unclear exactly where the car was at the moment the photo was taken. If one wishes to distinguish different environments (such as xenon trapped in a host versus free in solution) by chemical shift, the gas must move between environments slowly enough to have distinct peaks in the spectrum. Exactly how slow that rate must be depends on the chemical and instrumental system but can be fundamentally described by the uncertainty principle: If a nucleus can exchange between multiple magnetic environments, then the uncertainty in its energy, or resonant frequency, is inversely proportional to its lifetime, or residence time, in one of those environments:

$$\Delta\nu = \frac{\hbar}{\tau}$$

If the nucleus spends a long time in one environment, there is little to no uncertainty in the resonance frequency, and a sharp peak at the resonance frequency is observed. As the

nucleus' residence time in that state decreases, the uncertainty in resonance frequency increases and the peak is broadened.

In the case of two equivalently populated states, the spectrum coalesces to a single peak at the average resonance value when the exchange rate, given as $\frac{1}{\tau}$, is large compared to the frequency difference between the two peaks. The coalescence point, t_c, is related to the energy difference between the two lines, Δf (Hz), by

$$t_c = (\sqrt{2}\pi\Delta f)^{-1} = \kappa^{-1}) \tag{3.2}$$

where $\kappa = \kappa_{AB} + \kappa_{BA}$ is the total exchange rate. This allows us to separate exchange processes into three regimes: The slow exchange regime ($\frac{\kappa}{|\Delta\omega|} \ll 1$), the intermediate exchange regime ($\frac{\kappa}{|\Delta\omega|} \approx 1$), and the fast exchange regime ($\frac{\kappa}{|\Delta\omega|} \gg 1$), where $\omega = 2\pi\nu$ (Fig. 3.8).

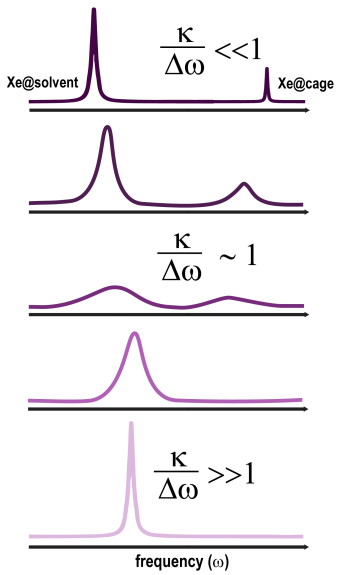

Figure 3.8: Exchange regimes for xenon in the presence of two distinct environments; in this case, a bulk solvent environment and a dilute molecular host (cage) environment. As xenon exchanges more quickly between environments, they become less distinguishable on an NMR spectrum, until, finally, a population-weighted average of the two resonances dominates.

In the slow exchange regime, the total exchange rate is much smaller than the difference in resonance frequency (or chemical shift) between the two pools, and the NMR spectrum contains sharp, resolved lines corresponding to xenon in each environment. In the intermediate exchange rate, xenon is exchanging quickly enough between environments that distinguishing them becomes more difficult, as lines broaden (due to uncertainty) and begin to approach one another as both environments' chemical shifts begin to weight the others'.

Once the exchange rate reaches the coalescence lifetime (t_t), both populations collapse into a single peak whose position is the average of the resonance frequencies of the two environments weighted by mole fraction of xenon in each population. Most often, the relative populations of xenon are not equal, leading to peaks of variable magnitudes in the NMR spectrum. The high polarizability that lends xenon high sensitivity to its chemical environment lends itself to exploitation for kinetic studies: by monitoring changes in chemical shift or peak width as xenon exchanges in and out of different chemical environments, one can elucidate kinetic parameters such as xenon binding affinity, association and dissociation rate constants.[42,43]

3.4.2 Exploiting Xenon Exchange with Host Macrocycles

An advantage of ^{129}Xe NMR is that xenon, being inert, does not alter or destroy any of the samples with which it interacts. But then the obvious question arises: How can one achieve selective molecular detection? To functionalize xenon for selective interactions that produce distinguished resonances, we utilize cage constructs that have internal volumes with which xenon has sufficient binding affinities and residence times to yield distinct peaks on a ^{129}Xe NMR spectrum (Fig. 3.9). While xenon acts as a highly sensitive probe for changes in the chemical environment, a highly customizable cage determines the specific event to be detected. Examples of the most prominent types of xenon hosts are shown in Fig 3.10.

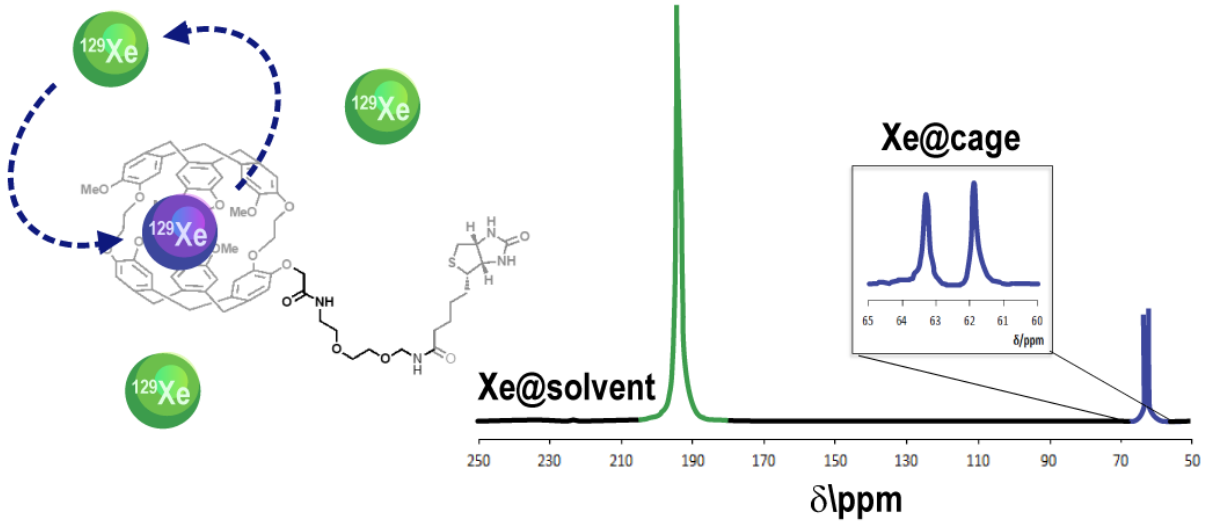

Figure 3.9: Xenon atoms exchange in and out of cryptophane derivatives slowly enough to yield unique Xe@cage resonances in a ^{129}Xe NMR spectrum. Two cage peaks are observed due to the presence of diastereomers.

These xenon-host ensembles, termed biosensors, currently come in two major classes: supramolecular compounds such as conjugates of cryptophanes, cyclodextrins, pillar[5]arenes, calixarenes, cucurbiturils and metallosupramolecular cages;[44–50] and larger compartmental carriers including viral capsids, nanoemulsions, nanoparticles, gas vesicles, liposomes, and some proteins.[51–57] The continuously exploding diversity of xenon biosensors has been applied to the selective detection of a variety of binding events involving receptors on cell surfaces, transmembrane proteins, enzymes, and reporting on microenvironments indicative of tumors.

Cryptophane cages were the first construct to be used with xenon for NMR studies due to the large binding affinity of Xe for cryptophane-A (CryA).[58] Table 3.1 lists the physical and kinetic properties of this and other xenon hosts. Synthesis of the starting CryA monoacid is technically difficult, requiring allylation of both hydroxyl groups of 3,4-dihydroxybenzaldehyde, the building block of CryA, followed by selective deprotection before final cyclization to the

cryptophane. The allyl group does not greatly affect cyclization and can be oxidized to a carboxylic acid for further derivitization.[59]

Table 3.1: Examples of xenon biosensors and their properties

Host	**129Xe δ(ppm)**	**Affinity (aq) (M^{-1})**	**Inner volume (A^3)**	**[Xe]/[host]**
Cryptophane-A	60	3.3-3.9 x 10^3	85-89	1
CBns	120-123	2.5 x 10^3 (CB6)	ID = 4.3 Å (CB6)	1
Pillar[5]arene	115	≈10	ID = 4.7 Å	1
Fe_4I_6 cages	204.4	≈10	141	1
α-Cyclodextrin	196	22.9	176	1
Calixarenes (STCAS)	117.7	13.6	138	1
Zeolites (ZXSM-5)	120-140		pore diameter:5-6	≫1
Gas vesicles	14.4-51.4		OD: 1.45x10^3	≫1
Nanodroplets (PFOB)	102-120		4x10^9	48x10^3
Bacteriophage (MS2-CryA)	57			≫1
β-Lactamase	255	≈ 10^2		4

In solution, xenon exchanges slowly between the bulk solution and host cage such that unique resonance corresponding to xenon encapsulated in the cage (xe@cage) appears (Fig. 3.9). When the cage is functionalized with a specific targeting moiety, there will be a change in xenon chemical shift upon binding of the host to the target.[60] Starting with a simple biotinylated CryA binding to streptavidin, this approach has since accomplished the detection of ligand binding to human carbonic anhydrase, $\alpha_{2b}\beta_3$ integrin, DNA hybridization, enzymatic cleavage, and others.[20,21]

Recently, cucurbit[n]urils (CBns), another family of macrocyclic hosts, has gained popularity in the xenon biosensing community. CBns are donut-shaped molecules made up of n glycouril units linked by methylenes, lending their inner cavities a relatively hydrophobic quality, while their portals, which are decorated with carbonyls, proffer aqueous solubility.[61] Portal diameters are roughly 2 Å smaller than that of the inner cavity, creating a constrictive binding pocket for molecular guests. This interesting structural and potential distribution, as well as their high stability and non-toxic quality, has made CBns especially useful as catalysts for click chemistry and as drug carriers that help to solubilize, stabilize and protect their payload.[62–65]

The tunability of their inner volumes means CBns are capable of capturing a wide variety of small molecule guests. As it turns out, certain CBns can even encapsulate xenon at timescales observable by NMR. For some time, the six-membered CBn, CB6, has been the "goldilocks" host for CBn-based Xe hyperCEST studies. Despite having a much lower binding constant compared to CryA (K_a = 2500 M^{-1}), the Xe-CB6 system is sufficiently long lived to have a unique chemical shift on a ^{129}Xe spectrum, but transient enough (κ = 2 kHz) to gain signal enhancement via CEST experiments.[57,66] By comparison, the residence time

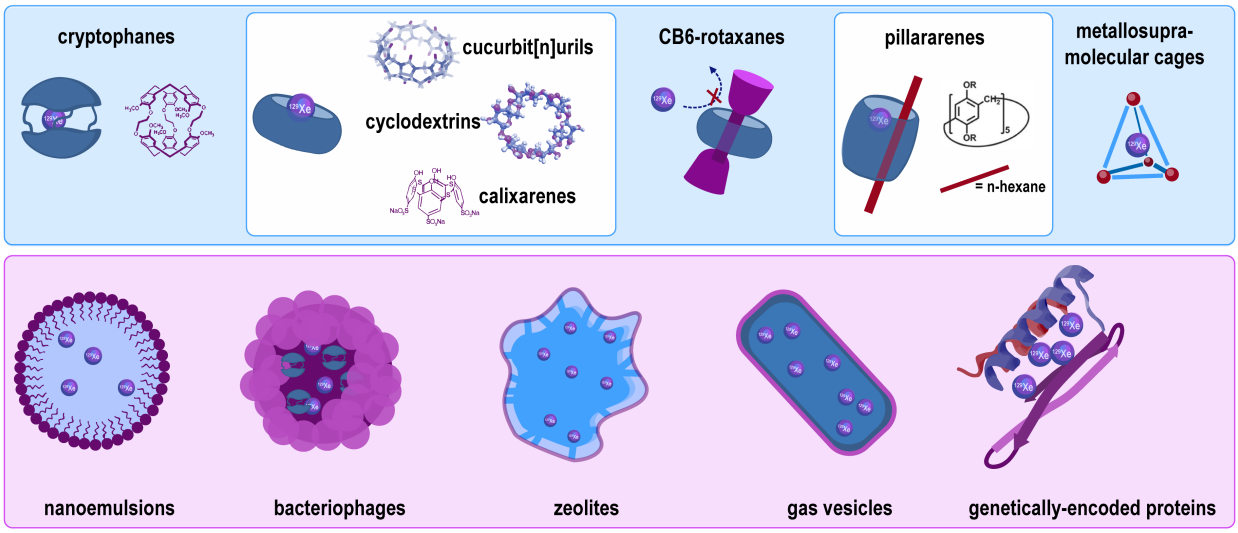

Figure 3.10: Major types of xenon hosts used for biosensing. The top row comprises the family of structures that carry only one xenon atom at a time, while the bottom row provides examples of macromolecular carriers that can simultaneously accommodate a few to many thousand xenon atoms.

of xenon in the smaller CB5 is nearly a day, making practical repetitive experiments impossible, while CB7-10 have shown minimal observation of xenon residence via hyperCEST due in part to the larger internal diameter of CB7-10 (7.3 Å – 11.7 Å) compared to CB6 (5.8 Å).

For the most part, CB6-based xenon biosensors have typically reported on their chemical environments indirectly, e.g. a CB6 is threaded onto a rotaxane axle that is cleaved in response to a specific stimulus.[54,67] Upon cleavage, the CB slides off its axle, and becomes available for exchange with xenon leading to an observable signal. Happily, developments in the use of functionalized CBns as xenon biosensors will potentially expand xenon biosensing toward multiplexed detection (see Chapter 6). Despite xenon's decent binding affinities for these and other macrocyclic hosts, there is always significantly more xenon dissolved in the bulk solution than in any given cage, meaning higher (µM) concentrations of cage are required for direct spectra, inhibiting their utility as sensors for very small concentrations of targets. However, indirect methods such as hyperCEST, have provided detection limits down to pM concentrations.

3.4.3 HyperCEST

Application of chemical exchange saturation transfer (CEST) techniques to hyperpolarized xenon (hyperCEST) has improved detection limits of biosensors to nano- and picomolar scales.[43,52,55] Instead of using labile protons on amides or water molecules, which can only provide detection limits down to mM concentrations, hyperCEST exploits the fact that thousands of xenon atoms can exchange in and out of a biosensor in one saturation cycle, greatly lowering the concentration requirements of both xenon hosts and biological targets for de-

tection.

In a hyperCEST experiment, selective saturation pulses destroy spin hyperpolarization. During one saturation cycle, xenon exchanges between host molecules and the bulk aqueous environment. As previously discussed, xenon atoms in hosts like cryptophanes and cucurbiturils have unique chemical shifts that are resolved from that of xenon dissolved in solution. If the saturation frequency corresponds to that associated with xenon encapsulated in a host, the loss of spin polarization at the host resonance is reflected in a decrease of the much larger dissolved Xe resonance as a result of exchange of the caged Xe back into the bulk solution (Fig 3.11). On the other hand, if a saturation pulse is not on resonance with the caged xenon frequency, then there will be no discernible change in the bulk solution peak. Of course, if saturation pulses are on resonance with the dissolved resonance itself, there will also be a drop if not complete obliteration of the signal.

Often, caged xenon populations manifest below the noise of a direct ^{129}Xe NMR spectrum, so saturation frequencies must be scanned in order to find their spectral location. This process is accomplished by repeating the hyperCEST experiment for each saturation frequency. Plotting the area of the dissolved xenon resonance against the arrayed saturation frequencies yields a hyperCEST z-spectrum, as shown in the bottom of Fig. 3.11. HyperCEST z-spectra thus allow us to indirectly probe small, fast-exchanging populations of xenon hosts by way of the much larger dissolved xenon pool. The advent of hyperCEST spectroscopy and imaging has enabled the detection of an expanding number of targets using ^{129}Xe NMR at biorelevant concentrations. Current development of ultra-fast methods has further mitigated the time-sink of having to repeat the experiment for many saturation frequencies, making possible the acquisition of full z-spectra in only a few minutes.[68]

Just as in direct NMR spectroscopy, a perfect delta function is not returned when the saturation pulse is on resonance with the caged xenon population; rather, there is a distribution of frequencies that cause broadening of these so-called CEST responses. The physical phenomena responsible for this broadening contain the usual suspects: exchange and lifetime broadening. An additional contribution comes from the so-called "spill-over" effect, wherein imperfectly selective saturation pulses cause depolarization to spill over into the next frequency step in the saturation frequency array. This causes additional apparent loss of signal on top of that expected from saturation at the new frequency.

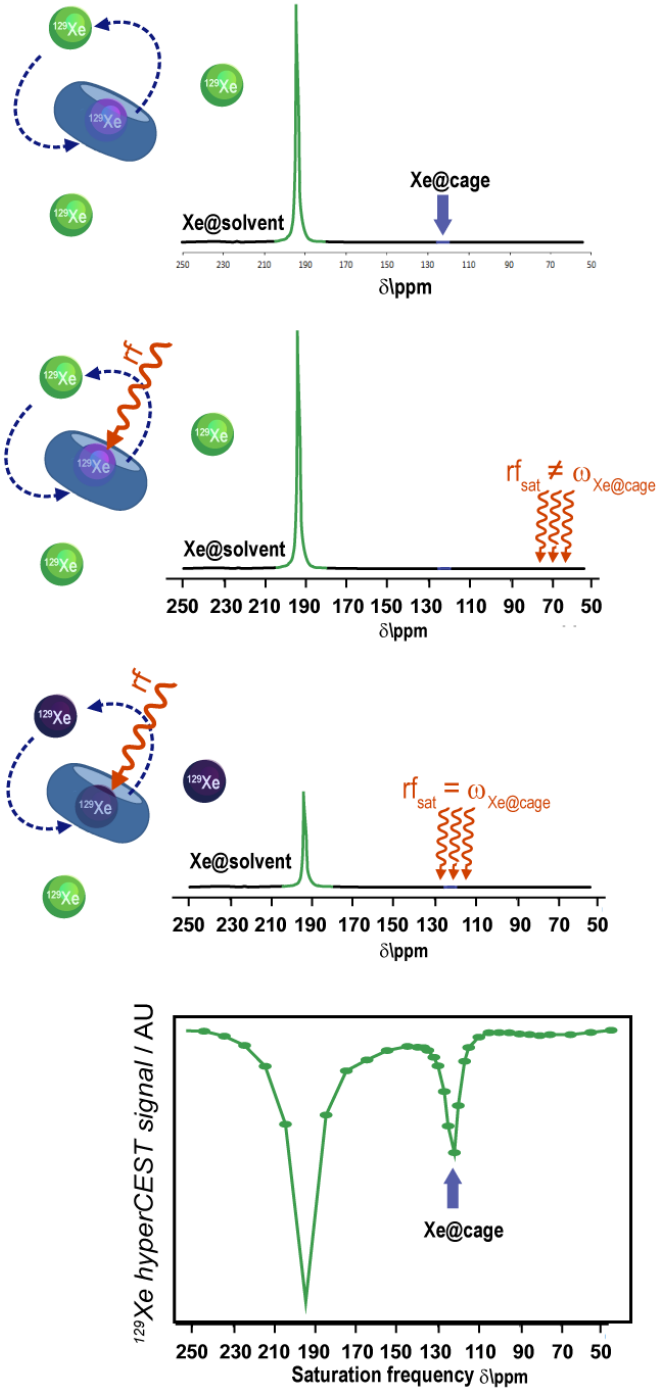

Figure 3.11: ^{129}Xe HyperCEST takes advantage of the fast exchange of xenon atoms in and out of hosts such as donut-shaped CB6. Xenon within CB6 (Xe@CB6, blue) has a characteristic resonance that is distinct from that of dissolved xenon (Xe@solvent, green) and not observable in direct spectra. If the sample is irradiated with a saturation RF pulse corresponding to the Xe@CB6 resonance, however, the caged xenon will become depolarized (dark purple). Xenon atoms will continue to exchange in and out of CB6 during saturation, leading to a net loss of signal from the much larger Xe@solvent resonance. Off-resonance saturation pulses will lead to no change in the Xe@solvent peak (until the Xe@solvent resonance is itself saturated, of course). If the area of the Xe@solvent peaks are plotted against an array of saturation RF frequencies, a z-spectrum is obtained that provides indirect observation of the Xe@cage population.

Technical consideration: Saturation power

Saturation pulse power not only determines the degree of saturation in a z-spectrum; arraying it leads to the quantification of important kinetic parameters in a xenon biosensor system. This makes it important to know how to modulate saturation power appropriately, which follows from an understanding of the technology underlying RF generation in a spectrometer.

The RF source synthesizes, gates, and controls the phase of pulses. Usually pulses are generated at a power of a few mW that is then amplified to 10^2 W before being sent to the probe. For selective pulses, an attenuator is placed between the RF source and amplifier, as the amplifiers can only apply a fixed gain. The attenuator adjusts the output pulse power, with attenuation expressed in dB:

$$Attenuation = 10log(\frac{P_{out}}{P_{in}}) \tag{3.3}$$

Where P_{in} is the power entering the attenuator and P_{out} is the power at the output. This expression is known as the power ratio. For example, if output power is $\frac{1}{2}$ the input power, the power ratio is -3, i.e. halving the power corresponds to a change of -3 dB. Each 3 dB of attenuation leads to halving the power, so -6 dB will give $\frac{1}{4}$ the power, and -12 dB will give $\frac{1}{16}$ the power. Power relates to current by the equation:

$$P = Ri^2 \tag{3.4}$$

Where R is resistance and i is current. Since the strength of the magnetic field generated by the pulse (B_1) is proportional to the current,

$$B_1 \propto \sqrt{P} \tag{3.5}$$

Therefore, to double the saturation field strength, P must be quadrupled. Multiplying the power by a factor of 4 is the same as doubling the power twice, i.e., +6 dB attenuation. Thus, to double B_1, 6 dB must be added to the pulse power.

A practical application of this knowledge is for calibration of pulse powers when the actual value of output power is unknown. Say a $\frac{\pi}{2}$ pulse of width t_p = 11 µs at (purportedly) 50 dB is calibrated, but a $\frac{\pi}{2}$ pulse at 20 µs is desired. To find the require attenuation, one can write the power ratio equation thusly:

$$P = [\frac{B_1^{new}}{B_1^{init}}]^2 = 20log_{10}[\frac{B_1^{new}}{B_1^{init}}] = 20log_{10}[\frac{t_p^{init}}{t_p^{new}}] \tag{3.6}$$

This results in an attenuation of 5.2 dB, so the pulse power is lowered to 44.8 dB to accommodate the new pulse width.

Chapter 4

Xenon Hyperpolarization: Technical Considerations

4.1 Introduction

Polarizers are like a good recipe: although many users apply unique personal touches to optimize certain properties, the same core components are always present. In this section, the focus will be on the most essential elements required to build a robust polarizer that is able to produce reliable batches of hyperpolarized xenon. First, a short summary of the experimental setup and flow path is described. Then, each component is discussed with some empirical technical considerations and notes on common variations on the instrumentation used.

The layout of a very basic xenon polarizer is shown in Fig 4.1. During a typical experiment, a gas mixture of xenon, helium and nitrogen is flowed through the system, passing through an oxygen and water trap before entering a glass optical pumping (OP) cell into which rubidium is heated and vaporized. The OP cell sits in an oven, which in turn is nested in a pair of Helmholtz coils. A diode laser is aligned with the long axis of the OP cell, and outputs 795 nm continuous wave light that is resonant with the D1 transition of Rb's valence electron. The light is guided through a quarter wave plate (to circularly polarize photons) and telescope (to dilate the beam cross-section) and into the OP cell. At the far end of the OP cell, a spectrometer receives the light so that the resonance absorption can be monitored.

Momentum-conserving collisions between gas-phase rubidium atoms and xenon atoms result in spin exchange such that polarized xenon is generated (see Chapter 3 for a more in-depth description of spin exchange optical pumping). The polarized gas is then bubbled into the inlet of the sample phantom, which rests in the probe of the magnet. In order to trigger the starting and stopping of bubbling, a solenoid valve is placed at the end of the line after the sample outlet. Flow is roughly adjusted using a manual flow meter or more precisely with an electronic mass flow controller. The goal of the following sections is to provide practical

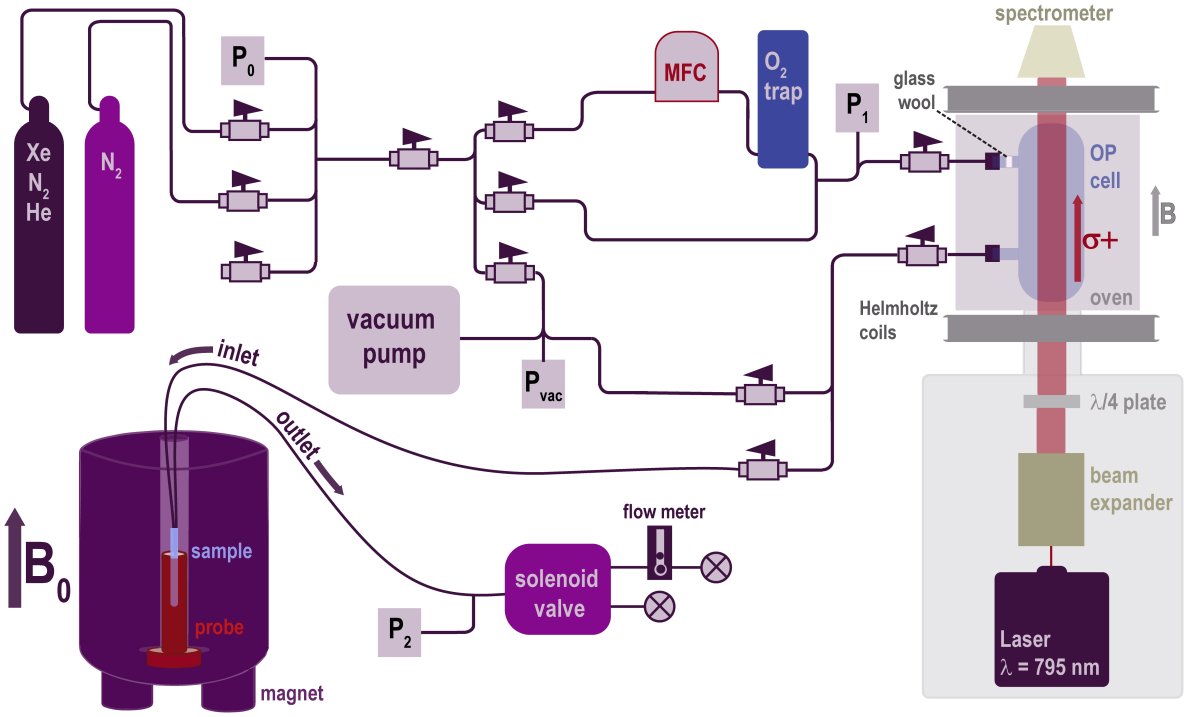

Figure 4.1: The SEOP setup used to generate and deliver hyperpolarized xenon for this thesis work. When in use, a gas mixture of natural abundance xenon (26.4% ^{129}Xe), nitrogen and helium are flowed a mass flow controller (MFC) and oxygen trap before being introduced to the optical pumping (OP) cell, where xenon becomes hyperpolarized. The gas is then sent through glass wool to catch Rb vapor and out of the polarizer to be bubbled into a sample inside a magnet. The gas finally leaves the setup by way of a computer-controlled solenoid valve. Optionally, a vacuum pump can be connected to the setup to remove as much air as reasonably possible before purging a system that has been exposed to air. This situation arises when changing gas tanks, before opening the outlet valve to the sample, or after replacing the OP cell. However, we have found that with careful flushing and consideration of pressure gradients during these tasks, that a vacuum pump may not be required. When no experiments are running, the system is purged with nitrogen.

wisdom regarding each of these components.

4.2 Gas sources

It is important to keep in mind that the goal of each component in a polarizer is to optimize the generation and delivery of hyperpolarized xenon. Even the simple result that a mixture of gases, and not just pure xenon, is most often used in today's polarizers is the result of a great deal of theoretical prediction and empirical observations. While the types and relative concentrations of gases used vary between groups, all recipes address a few main phenomena

that affect polarization build-up or transfer efficiency: pressure broadening, wall collisions, spin exchange collisions, and spin destruction collisions. Adding an inert buffer gas, such as He, decreases the incidence of wall collisions. Meanwhile, unfavorable relaxation mechanisms that lead to emission of light of arbitrary circular polarization can be absorbed by the vibrational and rotational modes of a diatomic quenching gas such as N_2. Thus, atoms can non-radiatively decay back into their ground states.

However, the pressure inside the rubidium cell modulates the linewidth of the D1 transition. A pressure that is too high reduces photon penetration depth as well as the number of on-resonant photons (pressure broadening), and also encourages spin-destruction collisions. Further, collisions with buffer gas atoms depolarize Rb atoms. So one must balance the need for buffer and quenching gases to facilitate spin exchange while trying to limit depolarization by wall collisions and spin-destruction collisions.

Although the size of the signal in a Xe NMR experiment is proportional to the amount of polarized xenon in solution, the relative fraction of xenon in the cell is kept low due to the high spin-destruction cross-section xenon shares with rubidium. So, while collisions between rubidium and xenon that result in spin-exchange are encouraged by having higher pressure, how much of that pressure is comprised of xenon must be limited so that spin-destruction collisions are minimized. In pursuit of this balance, most polarizers use 2-5% xenon (natural abundance or isotopically enriched), 10% N_2, and balance He.

If one desires to have both a high concentration of xenon in solution and high polarization, a condenser submerged in a dewar of liquid nitrogen may be placed after the outlet of the cell. While gas is flowing, xenon will freeze inside the condenser while nitrogen and helium, whose freezing points are much lower than 77 K, will simply pass through it. The xenon vaporizes as soon as the condenser is removed from the liquid nitrogen, and pure xenon is bubbled into the sample.

4.3 The oxygen and humidity trap

The greatest enemy of a rubidium cell is oxidation. An oxidized cell is useless for polarization generation or transfer because there no longer exists the electronic structure required to achieve it. If a cell is only partially oxidized, that is, there is only a thin layer of oxide on the rubidium surface, it is still usable, but will require much higher temperatures to vaporize the oxide layer and uncover the unreacted rubidium. This situation leads to more time spent setting up experiments, high pressure (which lends itself to spin-destruction collisions), and more off-resonant photons, which can deplete polarization. This is what makes the presence of an oxygen and humidity trap a necessity for any polarizer.

The humidity and oxygen trap seems to be most useful when the setup is not being used for experiments. When not in use, the system is purged with nitrogen. We have found that

even tanks of research-grade nitrogen contain enough contamination to partially oxidize the rubidium in the OP cell over time. This is good to know, however, because it means one may as well use more affordable and accessible industrial-grade nitrogen. During experimentation, the system is purged with the $Xe/N_2/He$ mixture. While most style of oxygen and humidity traps made for gases will do, one must pay attention to how much the trap restricts flow into the cell. If flow through the trap is too limited, both polarization and bubbling efficiency will be adversely affected. An easy way to determine whether this is happening is to compare xenon NMR signal amplitude when flowing gas through the oxygen trap to when it is bypassing the trap.

4.4 The Laser

There is no hyperpolarized xenon without polarized rubidium, and there is no polarized rubidium without circularly polarized continous-wave light at the energy of the Rb D1 transition. To provide this, a high power (150 W) diode laser operating at variable current (to tune the resonance) is used. As shown in Fig. 4.1, the high-power incident beam is first dilated using a telescope to a cross section of approximately one inch so that as much of the cell volume as possible can be bathed in resonant light. The widened beam is then passed through a quarter wave plate that converts the linearly polarized light into circularly polarized light by introducing a phase difference between its linear components of polarization.

Once aligned with a spectrometer at the far end of the OP cell, the beam and optics remain set until maintenance is required. Because of fluctuation in ambient temperature and humidity, slight adjustments to the center of the resonance are made by changing the diode current. Polarization efficiency can be qualitatively monitored by observing a 'dip' in the center of the resonance as atoms absorb resonant photons.

It is important to monitor the laser chiller over time to make sure coolant levels are maintained. Insufficient coolant flow or volume leads to a rise in the laser temperature, causing shifting of the resonance and potentially a failure mode.

4.5 The oven

The oven in and of itself it not complicated: it comprised of 5 mm thick, insulated aluminum housing arranged in a hollow cube structure that surrounds the rubidium cell. Hot air is created outside of the setup by sending wall air through high loss coils in aluminum tubing at a constant pressure (30 psi). The aluminum tubing is inserted into the bottom of the oven housing and air flow is directed toward the middle or far end of the cell.

However, the oven's function is integral to the generation of hyperpolarized xenon. First, xenon is hyperpolarized as a result of spin-exchange collisions with rubidium vapor. The boiling point of rubidium is roughly 80°C, but oftentimes experiments are run at much higher temperatures in order to gain a higher vapor density, especially in cases where partial oxidation requires 'burn off' of the oxidized surface layer to expose unreacted rubidium- usually up to 135°C. If rubidium vapor density is high enough, the spin-exchange rate is much faster than the optical pumping rate, leading to an equilibrium described by the spin-temperature distribution and analogous to thermal equilibrium; this would begin to happen at a pressure of 70 psi and temperature of 160°C for our setup.

4.6 The Helmholtz coils

The Helmholtz coils generate the magnetic field needed to break degeneracy of Zeeman levels for both the rubidium valence electron spins and xenon nuclear spins. A relatively low field is required to do this (≈1.5 mT), and, curiously, one can still get some degree of rubidium polarization and spin-exchange in the absence of the coils due to the laser itself generating a small magnetic field. However, the coils remain requisite for any substantial polarization to be obtained. Two to three coils are typically used to create a linear field that is roughly homogeneous along the long axis of the OP cell.

4.7 The OP cell

Both optical pumping and spin exchange occur simultaneously and continuously inside the OP cell as described in Chatper 3. The geometry of the cell is cylindrical in order to minimize wall collisions and each of its circular faces is flat so as to minimize refraction. Others have gone into detail regarding surface coatings that further reduce wall collisions.[41] The cell contains the rubidium, and can be monitored for oxidation between experiments. Clues for oxidation include evolution of a gold or copper tinge to the normally silver rubidium- this is evidence of rubidium suboxides. Fully oxidized rubidium is white or yellow.

Clearing the cell of oxidized rubidium is not technically difficult but requires considerable care due to the potential ignition of pockets of unreacted rubidium in the oxide. First, the cell should be depressurized by closing it off from gas sources and partially opening the outlet to air so that depressurization is slow. This will make cleaning the cell a bit safer for two reasons: one no longer has to deal with opening a pressurized container in the fume hood, and it will deplete some of the remaining unoxidized rubidium.

Once depressurized, the cell is closed and removed from the polarizer, and placed in a fume hood. Rubidium oxide dissolves in acetone or isopropanol, exposing unreacted rubidium. This rubidium may ignite with ambient humidity. It is best to do several washes of isopropanol or acetone, then begin to titrate water into the solvents to react with and dissolve

unreacted rubidium. Once all rubidium and rubidium oxide is removed, the cell is filled with strong base, then strong acid solutions for one hour each, and then filled with deionized water overnight. The cell is dried in an oven and then purged with inert gas, such as xenon, argon or even nitrogen at ambient pressure before being placed in a glove box for filling.

Though it might sound redundant, this pre-purging ensures that the cell will be effectively purged. We have found that the typical purging process done in the glove box antechamber does not effectively purge the cell of air. Thus, when one goes to fill the cell with rubidium, a partially oxidized surface is evident almost immediately. This extra pre-purging step has greatly reduced the incidence of partially or fully oxidized surface layers during rubidium fills, which means the cells can be used to generate hyperpolarized xenon more readily upon installation on the polarizer.

To fill the cell, rubidium is heated in an opened ampule on a hot plate within the glove box until it has low enough viscosity to be transferred to the cell via glass pipette. This step requires some grace to avoid oxidation of rubidium before it is transferred to the cell, spraying rubidium into the arms of the cell, or breaking a pipette tip into the cell. It is recommended that the filler practice the motion of transferring the rubidium from the ampule to the cell a few times without rubidium in the pipette.

After filling, the cell is closed, removed from the glove box and installed on the polarizer once more. The tubing connecting the cell inlet to the polarizer is purged at around 40 psi, then tightened onto the cell arm while gas is flowing through it. Then, the outlet plumbing is similarly purged at 30 psi by routing gas from the escape valve at the front of the polarizer to the outlet valve at the back of the polarizer. One can check for leaks by closing the gas source and certain valves and monitoring system pressure.

Once both lines are purged, the cell can be opened to the system via the Young's valves in its arms; the inlet is opened first, then the outlet. When not in use, the cell is purged with nitrogen to conserve xenon and may also be closed from the system if need be.

4.8 Bubbling into a phantom

Bubbling directly into samples facilitates rapid dissolution of xenon. The inlet delivers xenon through polyimide capillaries and into the sample. Gas is allowed to flow freely out of the outlet. The fitting into which the capillaries are inserted actually has multiple holes drilled through it to allow for pressure equilibration. For a 5 mm phantom, one long bubbling capillary is used, and for a 10 mm phantom, two long bubbling capillaries are used. Any remaining holes are used as vents to prevent over-or under-pressure above and below the fitting.

In batch mode, there is no gas flow out of the polarizer between scans. This approach allows hyperpolarized xenon to build up in the cell during the delay. A more evolved form of batch mode hyperpolarized xenon generation uses a condenser submerged in liquid nitrogen, into which xenon condenses due to its relatively higher boiling point, but the buffer and quenching gases, He and N_2, do not. Gaseous N_2 does not condense because the temperature of the gas in the cold finger is higher than that of the surrounding liquid N_2 bath. This way, the gas that is bubbled into the phantom is primarily xenon, leading to larger SNR per transient in the NMR spectrum.

At times, the difference between atmospheric pressure and cell pressure is very high. Thus, when bubbling is initiated by the solenoid valve opening to air, a pressure gradient exists, which can lead to the sample being sucked up into the capillaries or even pushed through the phantom outlet. Some also suggest that this abrupt change might result in condensation of rubidium in the cell's glass arms, making them much more hazardous to clean. Thus, another common add-on is 'bypass' plumbing, which provides a constant pressure during and between experiments by maintaining a constant flow of gas but diverting it away from the sample phantom between scans. This is also known as continuous flow mode.

There is some finesse required to properly match pressure and flow to obtain optimal bubbling of gas into samples. If flow is too low for a given pressure, no bubbling will occur. If it is too high, one will end up with very large bubbles that push the sample solution up and out of the observation volume and potentially out of the phantom. This is a bigger problem with 5 mm phantoms compared to 10 mm phantoms due to their smaller diameter. If the oven temperature is changed, so will the quality of bubbling. As a result, it is important to do a few dummy scans when any parameters or samples are changed in order to monitor any changes in bubbling. There are few things worse than starting an hours-long hyperCEST experiment and having the bubbling get mussed up halfway through.

An additional consideration is the balance of flow rate with polarization rate. One may achieve a high flow rate with vigorous (but not excessive) bubbling and therefore a high concentration of xenon dissolved in the sample, which seems like the optimal setup. However, if flow is too high, one will be flowing xenon out of the polarizer faster than it can be polarized, leading to signal depletion over time. In total, these considerations amount to the requirement of largely empirical determinations of the best bubbling rate for a given sample.

When bubbling into aqueous liquids such as biological solutions, one may encounter problems with foaming. Foaming can cause a sample to creep up the phantom and be pushed out, leading to sample loss and possible damage to the solenoid outlet valve. Adding appropriate surfactants helps to reduce surface tension enough to break up bubbles and foam without doing harm to biomolecules. Many have reported the use of a variety of such surfactants; in our case we've found that the simple addition of 0.5-1% v/v octanol is often sufficient to reduce foaming, but can affect protein stability. Instead, when possible, a proprietary surfactant, pluronic L81, was used due to its passive effect on biological samples at low con-

centrations (1% v/v).

Some notable variations on directly bubbling into the sample exist. One such method involves pre-dissolving the xenon in a "bubbler" chamber before flowing the xenon-saturated liquid into the sample volume. This setup is ideal for studies requiring live cell imaging, as direct bubbling into cell solutions will lead to cell lysis. Flowing cell media through the bubbler and then into the sample volume is a gentler way to introduce dissolved hyperpolarized xenon to cells.

When samples are too viscous or too fragile for bubbling, gas exchange membranes can be used to non-disruptively dissolve xenon into the samples. A direct result of this thesis work, this method and device is expanded upon in depth in Chapter 8.

4.9 The Solenoid Valve

After the gas passes through the phantom, it travels through a flow meter and is separated from the external atmosphere by a solenoid valve. The solenoid valve has one inlet, an escape valve, and two outlets. One outlet is capped. When not bubbling, the gas is routed to the capped outlet.

When bubbling, the valve path switches so that gas flows through the uncapped outlet. This switch is activated by the spectrometer through an external trigger port on the console that can be activated by a pulse sequence program.

Chapter 5

Xenon sensitivity to differences in biosensor structure

Case: Effects of metal chelation on ^{129}Xe chemical shift of cryptophane cages

As touched on earlier, one pursued pathway for xenon biosensing is multiplexed detection, meaning the simultaneous identification of multiple unique analytes in one ^{129}Xe spectrum or image. This requires that each biosensor has either a markedly different chemical shift or relaxation rate when in the presence of its target. In the study comprising this chapter, we examined whether we could use cryptophane cages attached to a metal-chelating group (DOTA) to detect a large range of metal ions (Ca^{2+}, Cu^{2+}, Ce^{3+}, Zn^{2+}, Cd^{2+}, Ni^{2+}, Co^{2+}, Cr^{2+}, Fe^{3+} and Hg^{2+}). In all cases, xenon was sensitive to the capture of each type of metal ion. Interestingly, diastereomeric effects on the Xe spectra were also correlated with coordination number of the metal in the DOTA complex. As a result, we concluded that these sensors may be used to detect and quantify many biorelevant metal ions.

5.1 Background

Metal ions play an immense role in our lives, both biologically and environmentally.[69] Well-established methods for in vitro detection of metals, including atomic absorption spectroscopy and various electrochemical techniques exist, but aren't suitable for multiplexed detection nor examination of opaque, complex mixtures like whole blood or waste water.[70] Conventional NMR techniques can tackle simultaneous detection of different metal species, but at the cost of sensitivity loss and increased spectral complexity. Hyperpolarized xenon NMR, however, offers the potential for sensitive detection and simple, easily interpretable spectra. Recently, two different cryptophane cages modified with either a diphenylphosphino)benzamide or nitrilotriacetic acid group showed a responses to Zn^{2+} ions by inducing a change in chemical shift of the cryptophane bound ^{129}Xe NMR peak upon metal binding.[71,72] For the latter, chemical shift changes were also observed upon binding Pb^{2+} and Cd^{2+} ions.[73]

Table 5.1: DOTA-metal ion association constants[76]

Metal	$\log K_{a\ [Dota*Metal]}$	CN with DOTA
Ca^{2+}	16.4	8
Co^{2+}	20.3	6
Ni^{2+}	20.5	
Zn^{2+}	21.1	6
Cd^{2+}	21.3	8
Ce^{3+}	21.6	9
Cu^{2+}	22.2	6
Hg^{2+}	23	8
Fe^{2+}	24.4	

In our case, because our aim was to use one sensor to detect and discern a range of different metal species, we used DOTA (1,4,7,10-tetraazacyclododecane-1,4,7,10-tetraacetic acid) as our metal chelator. DOTA binds to a variety of metals with very high affinity (see Table 5.1 for a selection).

We chose the following metal ions as targets: $Fe^{2/3+}$, Cu^{2+}, Co^{2+}, Zn^{2+} and Ni^{2+} play essential roles in human metabolism,[74] while others, including Hg^{2+}, Cd^{2+}, and Pb^{2+}, are toxic and often found in waste water run-off.[75]

The origin of DOTA's ability to bind many metals lays in its structural flexibility and wealth of coordination points. DOTA contains four centrally-located tertiary amines and four carboxylates on its outer arms. When DOTA binds a metal ion, it can adopt a geometry that best satisfies that metal's size and preferred number of coordination points.[77,78] Smaller metals tend to prefer a lower number of coordination points (such as Ga^{2+}), while larger metals prefer a higher degree of coordination (such as Ce^{3+}).

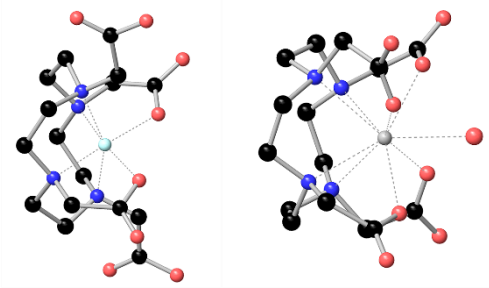

Figure 5.1: Crystallographically-determined structures of DOTA bound to metal ions with coordination numbers six, Ga^{2+} (left) and nine, Ce^{3+} (right).

Different coordination numbers (CNs) imply different DOTA geometries: coordinating at six

points generates an octahedral geometry while coordinating at eight points leads to a square antiprismatic geometry.[76] We posited that xenon may register this geometric difference based on previous studies that observed xenon sensitivity to structural changes in functionalized cryptophanes far away from the cage portion itself.[79,80] Therefore, the sensor was designed with cryptophane cage, DOTA, and a solubilizing Glu_5 peptide linker components (Fig.5.3). We also made sure to test metals tested were of a variety that included those with different DOTA coordination numbers.

5.2 Methods

5.2.1 Synthesis

All chemicals and solvents used in this study were of analytical grade and used as received from commercial sources unless otherwise noted. Deionized water (dd-H_2O) for synthesis and experiment was purified using a NANOpure system (Barnstead, USA), and phosphate-buffered saline free of metal ions was acquired from Sigma Aldrich.

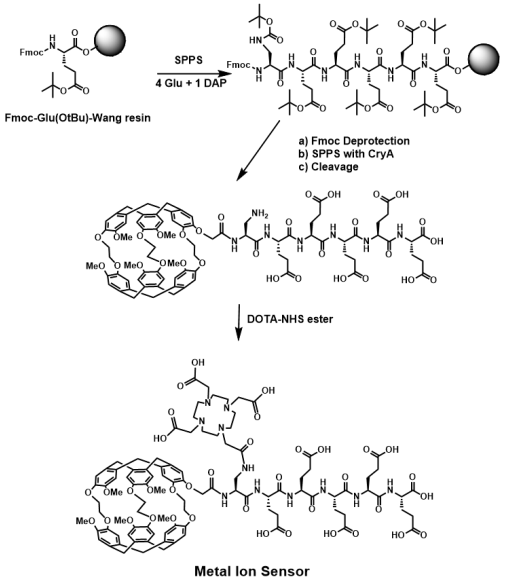

Figure 5.2: Synthesis of the metal ion sensor. Five glutamic acid molecules, one diaminopropionic acid, and a cryptophane cage were attached to Wang resin. They were then cleaved from the resin and DOTA was attached in aqueous solution.

An illustration of the synthetic flow is shown in Fig.5.2 (left). In order to maximize possible interactions between the DOTA moiety and xenon, we synthesized our sensor so that the DOTA was at a minimum distance from the cryptophane cage. A diaminopropionic acid was used to bridge this distance. A DOTA-NHS ester was used to couple the DOTA to the primary amine of the diaminopropionic acid in aqueous solution before addition of the cryptophane-A. The 5-membered Glu peptide was added to solubilize both the inherently hydrophobic cryptophane-A and to compensate for the slight hydrophobicity that evolves when DOTA binds metals.

The whole sensor was assembled on a Fmoc glutamic acid Wang resin with solid-phase synthesis methods. The fmoc group was deprotected by addition of 20% piperidine at room temperature followed by addition of 5 equivalents each of fmoc glutamic acid, HBTU, and HOBT in DMF. Reaction completion after 5 hours was confirmed by a Kaiser test. This process was repeated for each of the five

Glu residues, the Fmoc-diaminopropionic acid, and the cryptophane cage monoacid (Kang Zhao, Tianjin University, China) Once completed, the sensor was cleaved from the resin using TFA: water:triisopropylsilane (95:2.5:2.5) for 3 hours. Precipitation was accomplished with diethyl ether, the precipitate isolated and redissolved in water. NaOH was required to encourage dissolution. DOTA-NHS ester was added in excess to the solution, and further NaOH was added until all DOTA-NHS ester was dissolved. The reaction volume was left overnight and 1 mg purified with reverse-phase high pressure liquid chromatography. ESI-HRMS verified the sensor structure (calculated: 2173.7077, observed: 2173.5882).

5.2.2 ^{129}Xe NMR experiments

For NMR experiments, 50 µM sensor construct samples were prepared in phosphate-buffered saline (pH 7.4). Hyperpolarized xenon was generated and delivered using the setup described in Chapter 4. A 400 MHz (9.4 T) Oxford magnet and Varian VNMRS console were used to acquire NMR data with a repetition rate of 0.5 s and spectral width of 50 kHz. All experiments were performed with sample temperatures at 20°C and 35 psi to avoid any conflation of temperature and pressure induced shifts. For each sample, preliminary spectra of xenon in the sensor alone were acquired before metal ions were added at a 1:1 molar ratio.

5.3 Results

The cryptophane-A structure has a chirality conferred by the twisting of the -O(CH$_2$)$_2$O- groups that bridge the cyclotriveratrylene units into a *anti* configuration (Fig. 5.3).

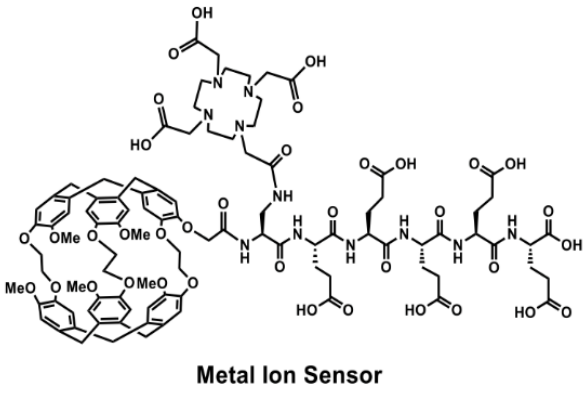

Figure 5.3: Sensor comprised of a cryptophane cage to bind xenon, a DOTA chelator, and solubilizing Glu_5 peptide.

Synthesis yields both enantiomers in equal parts. Our process of adding amino acid species to solubilize the cage for aqueous samples causes diastereomer formation. Since only amino acids of pure chirality are used, only two diastereomers in equimolar amounts are formed.

Xenon reflects its sensitivity to the chirality of the modified cage by the presence of two distinct and equally sized diastereomeric peaks in a xenon NMR spectrum (Fig.5.4).

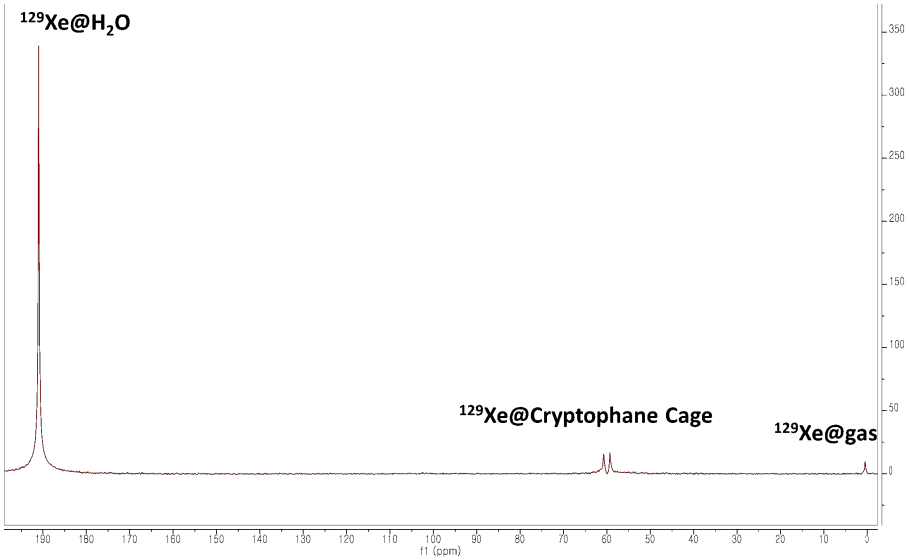

Figure 5.4: Hyperpolarized ^{129}Xe spectrum of the metal free sensor. The ^{129}Xe chemical shift was referenced to the ^{129}Xe in solution signal.

The addition of metal ions led to modest ($\leq$1 ppm) changes in the caged xenon chemical shift, sometimes asymmetrically for each diastereomer (Fig 5.5, Fig.5.6). The absence of any shift changes for the metal ions in the presence cage-peptide without DOTA attached verify that metal coordination to DOTA, and not metal-peptide interactions, is the source of the induced shift change. However, no correlation between shift change and atomic number or para/diamagnetic character was observed. This result indicates that the induced shift changes are likely due to structural deformations of the cage caused by transient interactions either enabled or disabled by the coordination of metals with DOTA, as suggested by theoretical work by Sears *et al.*[79,81]

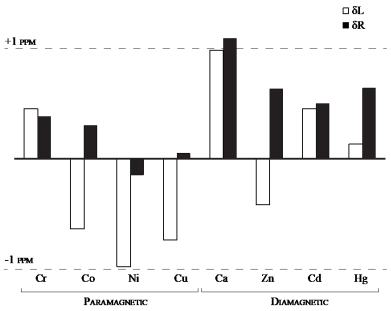

Figure 5.5: Comparison of metal induced xenon shift changes from free sensor to metal bound sensor for each diastereomer. Metals are arranged from lowest to highest atomic number within each subset.

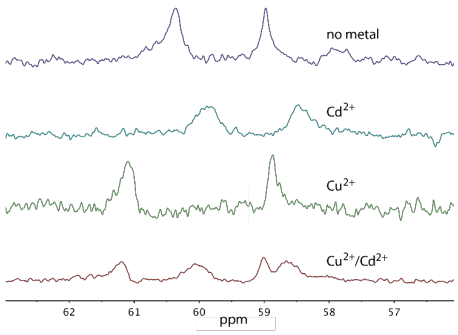

Figure 5.6: Comparison of ^{129}Xe spectra for 50 µM cryptophane complex with: no metal, Cu^{2+}, Cd^{2+}, and a 50/50 mix of Cd^{2+} and Cu^{2+}.

Transient contact-mediated interactions are also the likely culprit of the asymmetric shift changes for diastereomers of the same metal-coordinated sensor. Further, these results indicate that the distance between the coordinated metal and xenon is large enough to preclude paramagnetic relaxation effects on linewidths.

The smaller, first row transition metals examined form the hexadentate DOTA complex (CN = 6), while the larger metals form the octadentate complex (CN = 8). The octadentate complexes gave way to larger upfield shifts for both diastereomeric peaks. Interestingly, Ce^{3+}, a lanthanide with a CN = 9, yielded additional caged xenon peaks (Fig.5.7). This is likely the result of slow exchange between multiple isomers of DOTA-Ce^{3+}, which, according to previous ^{1}H NMR studies on lanthanide-DOTA chelates, take on a square antiprismatic geometry.[82] These isomers are formed by the acetate arms of DOTA falling into helical conformation upon the capture of a metal ion and capping with a water molecule.

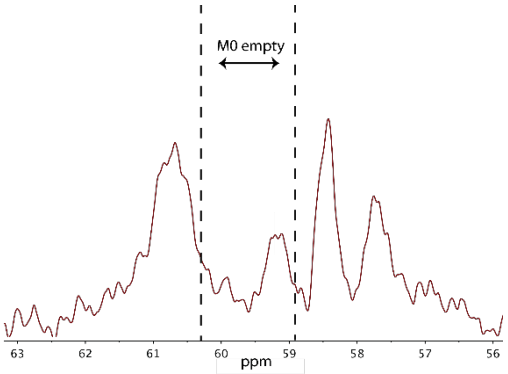

Figure 5.7: ^{129}Xe chemical shift of the cerium bound sensor (CN=9) showing broadened peaks and evidence of diastereomeric DOTA chelation. 'M0' indicates the chemical shift of the metal-free sensor.

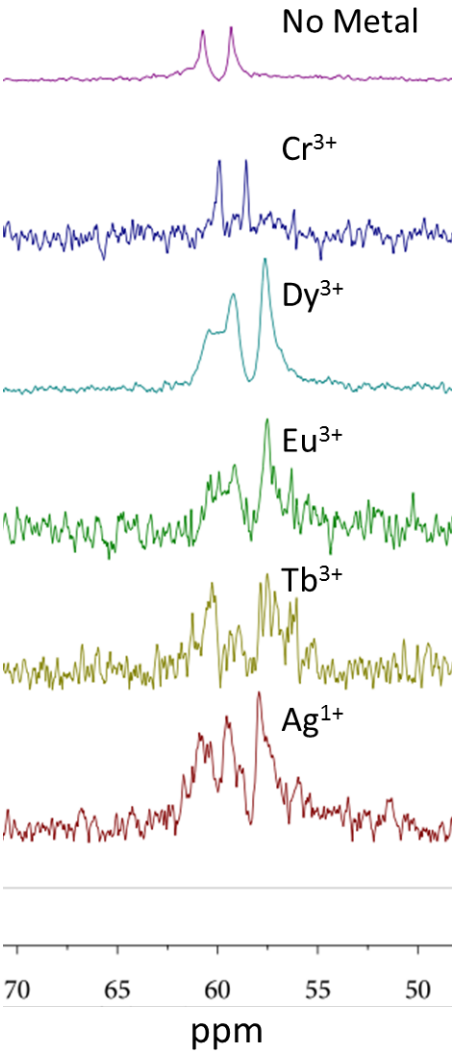

Figure 5.8: ^{129}Xe@Cryptophane cage spectra in complexes with various heavy metals. The presence of multiple peaks, and broadening are apparent.

Because DOTA can make stable complexes with certain heavy metals whose hyperfine interactions, including pseudocontact shifts, might result in enhanced chemical shift changes, we tested few other heavy metals (Dy^{3+}, Eu^{3+}, Tb^{3+}, and Ag^{2+}), Fig.5.8. The shift changes in this set were not substantial compared to those of the lighter metals.

As with Ce^{3+}, additional peaks evolved, indicating various structural isomers in slow exchange. The relaxation effects of the lanthanide ions is substantial, however, meaning much more signal averaging is required for detection and limiting further analysis at the time of this work.

Given that xenon is sensitive to the chirality of cryptophane-A,[81] it is not so surprising that it can detect the additional chirality of chelated DOTA, but it is interesting that it can do so at 8-10 bonds away from the cryptophane cage itself. This sensitivity can be exploited to detect isomeric metal complexes, which is important when analyzing samples of molecules whose isomers contain one or more that is toxic and others that are not.

Titrating the ratio of Fe^{3+} ion concentration to sensor showed two sets of diastereomeric peaks, indicating that the empty and bound DOTA forms are in slow exchange (Fig.5.9), which is in line with the high affinity of DOTA for the examined metals (Table 1).

5.4 Conclusion

The proportional increase in the peak areas corresponding to xenon in metal-coordinated cages and decrease in that for xenon in non-coordinated cages show the potential for quantative detection of specific metal ions. However, the variation in metal-induced shift due to as yet unclear dynamic structures formed by the cage, peptide and DOTA components of the sensor leaves much to be investigated before xenon-based metal ion sensors can be optimized.

Nonetheless, this technique, when applied with sensitivity enhancing methods such as ^{129}Xe enrichment and hyperCEST, makes possible the detection of metal complexes in the low nanomolar range. This, combined with the existence of distinct metal-induced shifts, enables the discernment of multiple metal ions in the same sample when one metal may be at a much lower concentration. ^{129}Xe MRI methods may further provide localized imaging of metals in a sample.

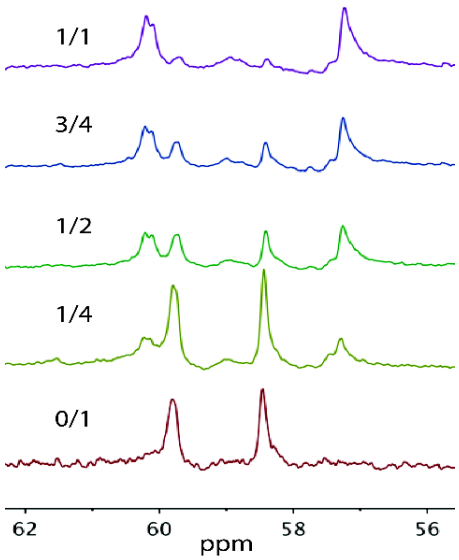

Figure 5.9: Spectra showing estimated ratios of dissolved Fe^{3+} to metal-free sensor with 1/1 corresponding to about 95 % bound.

Chapter 6

Taking a passive role: Indirectly functionalized xenon biosensors

Case: Rotaxane-based probes for the detection of hydrogen peroxide by ^{129}Xe hyperCEST NMR

The development of sensitive and chemically selective MRI contrast agents is imperative for the early detection and diagnosis of many diseases. Conventional responsive contrast agents used in ^{1}H MRI are impaired by the high abundance of protons in the body. ^{129}Xe hyperCEST NMR/MRI comprises a highly sensitive complement to traditional ^{1}H MRI due to its ability to report on specific chemical environments. To date, the scope of responsive ^{129}Xe NMR contrast agents, though growing exponentially, lacks breadth in specific detection of small molecules, which are often integral markers of disease. This chapter describes the synthesis and characterization of a rotaxane-based ^{129}Xe hyperCEST NMR contrast agent that can be turned on in response to H_2O_2, where upregulation of this small molecule is implicated in a number of disease states. Exogenous H_2O_2 was detected by ^{129}Xe hyperCEST NMR in the low µM range, as well as endogenously produced H_2O_2 by HEK 293T cells activated with tumor necrosis factor.

6.1 Background

Sensitive and selective detection of disease markers is of high importance in the identification and treatment of a variety of human diseases. Magnetic resonance imaging and spectroscopy (MRI and MRS) benefit from high resolution and excellent tissue penetration. Conventional MRI techniques rely on the difference in the relaxation properties of protons primarily from water molecules present in different tissue types. Typically, contrast agents in the form of paramagnetic metal chelates or spin-labeled biomolecules that alter relaxation properties of local water molecules are applied to provide additional structural and functional information.[83] Responsive ^{1}H and ^{13}C NMR contrast agents have also been developed that produce a signal only in the presence of particular disease markers such as enzymes, signaling molecules,

and oxidizing conditions.[84–87] This approach can aid in early disease detection and provides insight to the chemical environment enabling a better understanding of the disease pathology. However, even with these contrast agents, signal and sensitivity are lost due to spectral complexity within the limited chemical shift range of protons.

^{129}Xe hyperCEST NMR comprises a sensitive complement to traditional ^{1}H MR imaging approaches.[14] The easy deformation of xenon's electron cloud leads to its chemical shift range of several hundred ppm for biological systems, enabling direct and quantitative imaging of local spin environments that are often indistinguishable via conventional MRI. The combination of this acute sensitivity and xenon's high solubility in blood, tissue, and lipophilic membranes distinguishes it from other heteronuclear contrast agents.[13] Further, facile hyperpolarization of ^{129}Xe nuclei can be obtained through spin exchange optical pumping, leading to contrast enhancement of 4-5 orders of magnitude over thermal polarization.[2] The lack of background ^{129}Xe in most systems gives rise to uncomplicated spectra as well as the potential for improved resolution of small, localized populations of target molecules.[15]

Being inert, ^{129}Xe is effectively functionalized for selective detection by participating in supramolecular host-guest interactions that cause either large chemical shifts or changes in relaxation parameters that are distinct to the host environments in which ^{129}Xe resides.[19,58,88,89] Since the majority of xenon atoms are present in bulk solution and undergo continuous exchange with host molecules, we can exploit exchange between host-bound and "free" xenon by way of CEST techniques to attain detection limits of hosts down to the sub-nM level.[19,67]

To create "turn-on" ^{129}Xe hyperCEST NMR contrast agents, we typically use the known Xe host Cucurbit[6]uril (CB6) due to its favorable exchange parameters for hyperCEST applications.[57,61] CB6 is a torus-shaped molecule that can harbor a single Xe atom in its interior, creating a distinct ^{129}Xe@CB6 chemical shift.[66]

To prevent Xe atoms from entering the interior of CB6 and producing this unique signal until desired, the CB6 is threaded onto a molecular axle that occupies the CB6 cavity. This axle is then capped by two bulky stopper groups creating the supramolecular species known as a rotaxane. By designing one of these bulky stoppers to be cleaved under specific conditions such as activation by a disease marker, a Xe@CB6 signal can be selectively observed only when activated. Using these design principles, a rotaxane that cleaves in the presence of a strong base as well as an enzyme cleavable rotaxane probe that releases CB6 in the presence of a cancer-related matrix-metalloproteinase (MMP) enzyme have been produced.[54,67] Based on the design elements of these first examples, we sought to create a probe that would be responsive to upregulated levels of hydrogen peroxide (H_2O_2) (Fig.6.1).

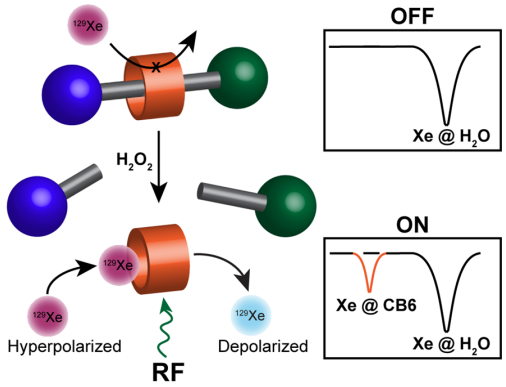

Figure 6.1: Schematic for the hydrogen peroxide-sensing rotaxane for Xe hyperCEST NMR. CB6 (orange) is threaded along a molecular axle (gray) which is mechanically locked into place by the presence of two bulky stoppers (blue and green) creating the supramolecular complex known as a rotaxane. The presence of the axle in the interior of CB6 prevents Xe from entering the cavity and presents no Xe@CB6 signal in the hyperCEST NMR spectrum (OFF). After cleavage of one of the bulky stoppers by reaction with H_2O_2, the CB6 cavity is now available to form a host-guest complex with Xe atoms. Insets: When inside the CB6 cavity, the Xe experiences a relatively shielded environment creating a unique chemical shift observable by Xe NMR. An RF saturation pulse corresponding to this chemical shift can be applied to selectively depolarize Xe inside the CB6. The reduction of the bulk hyperpolarized Xe ($Xe@H_2O$) signal as a result of depolarizing xenon at the Xe@CB6 chemical shift is then observed (ON). Recording the $Xe@H_2O$ signals using an array of saturation frequencies yields the above z-spectra.

Prior research has implicated upregulated levels of H_2O_2 in the advancement of inflammation and oxidative stress which has been correlated with the advancement of cancer,[90] diabetes,[91] cardiovascular disease, pulmonary disease, and inflammatory-induced processes such as wound healing.[92,93] ^{129}Xe MRI has demonstrated a unique strength in functional lung imaging, making such a sensor advantageous for the detection of pulmonary afflictions in which abnormally increased levels of H_2O_2 have been linked, such as in chronic obstructive pulmonary disease, community-acquired pneumonia, cancer of the lung, and denervation-induced muscle atrophy.[54,90,91] Current examples for imaging H_2O_2 in vivo or in opaque environments include chemiluminescent nanoparticles, a ^{13}C-labeled MRI probe, and a bioluminescent reporter.[86,94,95]

However, these techniques suffer from either limited sensitivity or the requirement of modifying the natural sample environment. Therefore, imaging H_2O_2 in an unperturbed environment at physiologically relevant concentrations remains an interesting challenge. The high sensitivity of ^{129}Xe hyperCEST NMR could allow for the detection of extracellular H_2O_2 at the low physiological levels, (0.5-50 µM), associated with the disease state.[92,96] Herein we describe the first synthesis, characterization, and application of a hydrogen peroxide-activated ^{129}Xe hyperCEST contrast agent for the detection of H_2O_2.

Four major design elements guided the synthesis of a rotaxane that could function as a sensitive and selective turn-on ^{129}Xe hyperCEST sensor for H_2O_2:

1. Inspired by the design of several H_2O_2 activated turn on fluorescent, PET, and $^{1}H/^{13}C$ MRI probes, a sensitive and selective aryl boronic acid group was chosen as a cleavable cap to our rotaxane (Fig.6.2a).[95–99]

2. To improve sensitivity, the rotaxane axle is composed of a paraxylene diamine moiety that has one of the lowest reported K_a for CB6 (5.5 x10^2) (Fig.6.2b).

3. To allow for ease of synthesis and modification to the rotaxane design, our synthesis was planned out convergently where the axle and cap are joined at later steps (Fig.6.2c).

4. To enable protein functionalization, a maleimide group serves as the other bulky capping group which can be attached to cysteine residues on a variety of biomolecules. Alternatively, a fluorophore can also be attached to allow for enhanced visualization of the cleavage reaction by UV HPLC (Fig.6.2d).

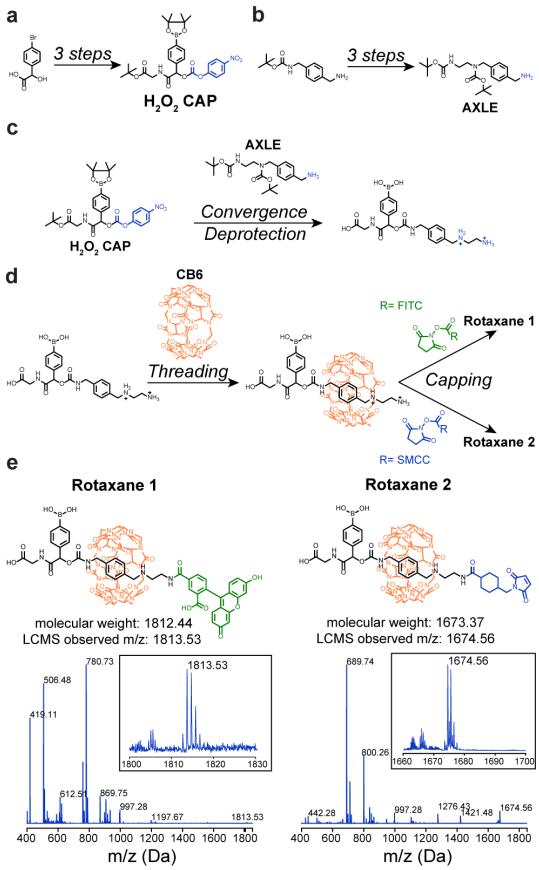

Figure 6.2: Convergent synthesis of Rotaxane 1 and Rotaxane 2. (a) Synthetic scheme to produce the H_2O_2-sensitive cap. (b) Synthetic scheme to produce the paraxylene diamine axle. (c) Combination of the cap and axle into a single molecule. (d) Threading of the CB6 molecule onto the singly-capped axle and subsequent capping of rotaxane with either maleimide or fluorophore functionality. (e) LC-MS traces of the final product Rotaxane-1 with expected m/z: 1813.44 Da and observed m/z: 1813.53 Da; boron isotope pattern observed. LC-MS traces of final product Rotaxane-2 with expected m/z: 1674.37 Da and observed m/z: 1674.56 Da; boron isotope pattern observed.

In this work, two rotaxanes were designed that differ in their non-responsive capping moiety. Rotaxane-1 is capped with a FITC fluorophore to allow for enhanced UV detection during HPLC/LC-MS cleavage studies. Rotaxane-2 is capped with a maleimide functional group that allows for further conjugation to biomolecules and was used in the ^{129}Xe hyperCEST experiments upon which this chapter focuses (Fig.6.2e).

6.2 Methods

6.2.1 General

All solvents and reagents, including cucurbit[6]uril hydrate (CB6·XH2O), 4-bromo-DL-mandelic acid, blycine tert-butyl ester hydrochloride, 1-(N-boc-aminomethyl)-4-(aminomethyl)benzene, N-boc-2-aminoacetaldehyde, NHS-fluorescein (5/6-carboxyfluorescein succinimidyl ester), and SMCC (succinimidyl 4-(N-maleimidomethyl)cyclohexane-1-carboxylate) were purchased from commercial suppliers and used without further purification. RR-TMV proteins were expressed as previously reported. Thin layer chromatography (TLC) was performed on silica gel 60 F254 (E. Merck) and visualized under a UV lamp at 254 nm. Column chromatography was carried out on silica gel 60 (E. Merck, 230–400 mesh).

6.2.2 Hyperpolarization

Hyperpolarized xenon was generated as usual via spin exchange optical pumping using our homebuilt polarizer. Rubidium was vaporized at 130-145°C in an oven and Rb polarization was obtained by applying circularly polarized light at 795 nm. Collisional mixing between Rb and ^{129}Xe atoms provided a ^{129}Xe polarization of roughly 1-3% throughout experiments. The system was pressurized at 60 psi during experiments with a gas mixture of 2% Xe (natural abundance), 10% N_2 and balance He, yielding a final concentration of ≈87 µM ^{129}Xe in the samples. Delivery of gas to the samples was controlled by an externally triggered solenoid valve at the outlet of the system.

6.2.3 hyperCEST experiments

All NMR data was acquired via a 400 MHz Varian VNMRS console using 5 and 10 mm VT liquids probes. An initial delay of 25 s allowed build-up of hyperpolarized xenon in the polarizer. During bubbling, xenon was delivered from the polarizer and bubbled into the sample for 20 s. Due to the tendency of cell samples to foam during bubbling, 1% v/v L81 Pluronic, a surfactant, was added to cell suspension and supernatant samples. After bubbling, a 5-8 s wait time allowed any bubbles or foam to disperse and a selective saturation pulse was applied at 22 dB (Varian) for 8 s. After saturation, an excitation pulse centered at the dissolved xenon resonance follows, proceeded by excitation (B_1 = 56 dB (Varian), τ= 11 s), FID acquisition and digitization. All samples were run at 293 K.

To acquire each point on hyperCEST z-spectra, saturation frequencies were arrayed so that any exchange of xenon between bulk water and a cage environment appeared as ‘dips’ in the dissolved xenon resonance at the saturation frequency corresponding to the caged xenon chemical shift. Due to the high sensitivity of Xe to very low CB6 concentrations and the tendency for CB6 to adsorb on glass surfaces, dummy samples were examined between ex-

periments to assure that no contamination contributed to observed CB6 signals.

Each FID in hyperCEST datasets was processed by Fourier transforming with zero-filling to 16384 points, 8 Hz apodization and zeroth-order phase correction. The area of the dissolved resonance was integrated for each spectrum, then divided by the largest in the set to normalize. All areas are then plotted versus saturation frequency to yield a z-spectrum. All z-spectra for a given sample were averaged then subjected to fitting by way of a least-squares iterative fit function applied to a simple Lorentzian model. This model along with most others does not account for the well-known 'spill-over' effect seen in z-spectral data, and therefore cannot be used to trivially quantify exchange characteristics of samples based on returned response widths.

6.2.4 Synthetic methods

Instrumentation and analysis

NMR spectra were recorded on Bruker Avance 300, 400 and 600 spectrometers for intermediate and final product characterization via ^{1}H, ^{13}C NMR. Small molecule intermediates were also analyzed using a low resolution LC-MS/MS which was equipped with an Agilent 1100 series liquid chromatograph (Agilent Technologies, USA) that was connected in-line with an API SCIEX 3200 MS/MS with an ESI ion source. Peptides and protein bioconjugates were analyzed using an Agilent 1200 series liquid chromatograph (Agilent Technologies, USA) that was connected in-line with an Agilent 6224 Time-of Flight (TOF) LC/MS system equipped with a Turbospray ion source. Percent modification was determined through integration of MS peaks. The integration of the completely unmodified protein peak served as an internal standard in determining the percent modification.

Synthetic procedures

Detailed synthetic methods, characterization data, and reagents can be found in *Sarah H. Klass, PhD Thesis, UC Berkeley, 2020.* The overall synethetic scheme is shown in Fig.6.2.

6.2.5 Protein and Peptide Modification

General procedure for modification of RR-TMV protein with Rotaxane-2

1-5 equivalents of rotaxane-2 with respect to TMV protein was added to a solution of protein in 1xDPBS pH 7.4 based on desired modification level. The solution was incubated for 2-4 h at ambient temperature with gentle rocking. The solution was then spin concentrated 3 times into 1xDPBS. Percent modification was determined by LC-MS TOF analysis and protein concentration was determined by absorbance at 280 nm, where the extinction coefficient for RR-TMV is 20,000.

General procedure for modification of V-CAM1 peptide with Rotaxane 2

1-5 equivalents of a 20 mM stock of rotaxane-2 with repsect to V-CAM1 protein in DMSO was added to a solution of protein in 100 mM PB. The solution was incubated for 2-4 h at ambient temperature with gentle rocking. The solution was then HPLC purified and lyophilized.

6.2.6 Cell Culture Procedures

Cell culture was conducted using standard techniques, using culture-treated flasks (Corning, Tewksbury, MA). HEK 293T cells were grown in Dulbecco's Modified Eagle Medium (DMEM) supplemented with 10% (v/v) FBS and 1% P/S. All cell lines were grown at 37°C in 5% CO_2 atmosphere. For ^{129}Xe NMR supernatant imaging experiments, immediately prior to addition of TNF, the supernatant of both the control and the experimental sample was removed and replaced with DPBS with 1% (v/v) FBS. The removal of most of the components in the DMEM media enabled better locking and Xe gas flow into the NMR tube.

6.2.7 Whole cell culture and cell supernatant experiments

For whole cell culture experiments, 0.75 µM TMV-Rotaxane-2 (7.5 µM Rotaxane-2) was added to 1.5 mL of a HEK 293T cell suspension in complete DMEM media at a concentration of 50,000 cells/mL for ^{129}Xe hyperCEST experiments. For cell supernatant experiments, cells were grown in 6 well plates to 100% confluency in complete DMEM media. To avoid technical issues encountered during the whole cell experiments with the complexity of the DMEM media, it was replaced with 750 µL of 1xDPBS + 1% FBS. For the TNF positive cells, 0.2uL of 200 µg/mL solution of recombinant human TNF (BD Biosciences, 554618) was added. The TNF negative cells were not treated, and both samples were incubated for 6 h at 37°C 5% CO_2. The supernatant from both wells was removed and centrifuged once to remove any cells that may be detached from the surface. The supernatant was then frozen until use in ^{129}Xe hyperCEST experiments. The supernatant media from cells incubated both with and without TNF were inoculated with 1 µM TMV-Rotaxane-2 (10 µM of Rotaxane-2). The samples were examined by ^{129}Xe hyperCEST NMR over the course of several hours.

6.3 Results

Cleavage of the rotaxane cap in the presence of excess H_2O_2 was monitored by HPLC/LC-MS. Although Rotaxane-1 was found to be completely oxidized by peroxide within one hour of exposure, the 1,6 elimination reaction that results in cap cleavage took much longer, with less than 50% cleavage after 16 hours.

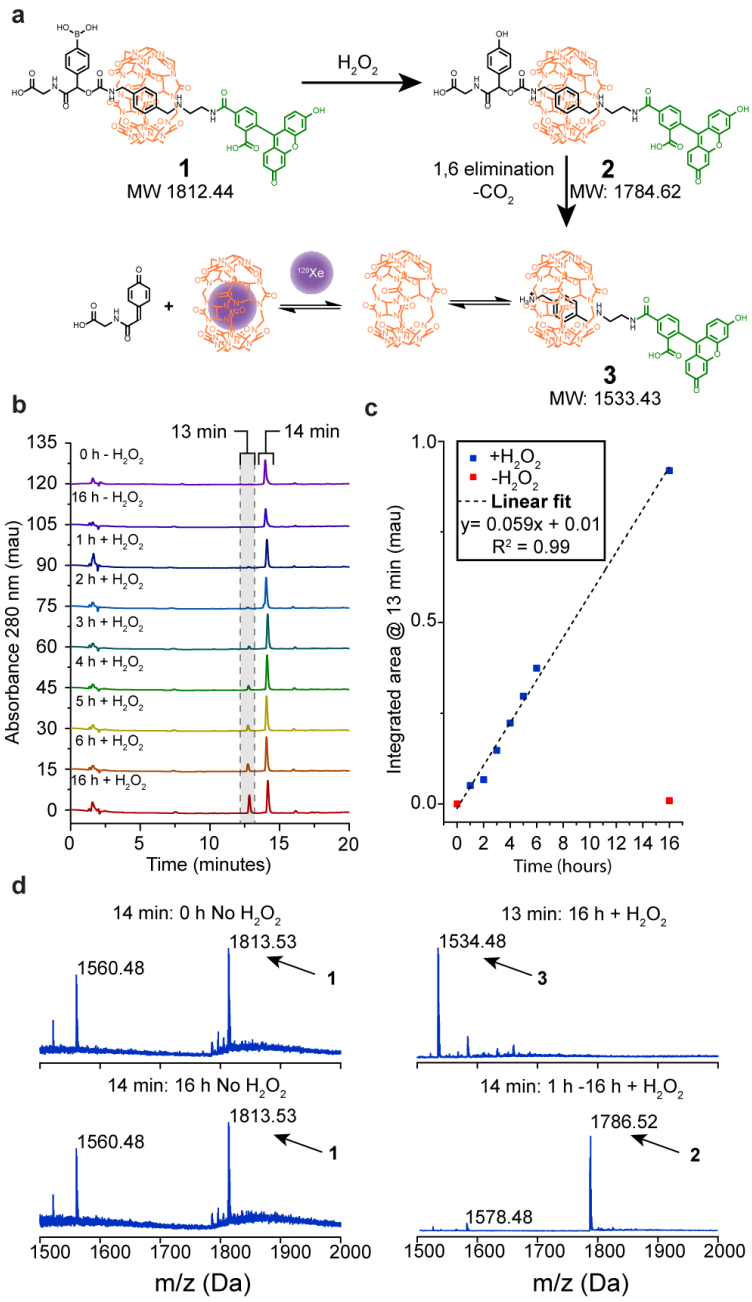

Figure 6.3: HPLC and MS analysis of rotaxane cleavage by H_2O_2. (a) Cleavage approach of Rotaxane-1 by H_2O_2 (b) HPLC traces of absorbance at 280 nm over the course of 16 h. A control sample with no H_2O_2 added was used to determine if there was any degradation of the rotaxane. The peak at 14 min was identified as either species 1 or 2 as no observable shift was seen upon oxidation, while the peak that emerges at 13 min was the cleaved rotaxane product. (c) By integrating the area under the emerging peak at 13 min a linear relationship is observed. (d) MS analysis of the peak at 13 min, determined to be the cleaved rotaxane product: expected m/z: 1534.43 Da; observed m/z: 1534.48 Da. MS analysis of the peak at 14 min corresponded to the intact Rotaxane-1 with the boronic acid group present only in samples that had not been exposed to H_2O_2 (0 and 16 h time points). In all samples that had been exposed to H_2O_2 (1–16 h time points), the MS trace corresponded to the oxidized phenol rotaxane, MW: 1786.52 Da.

Kinetic measurements were extrapolated from this data set under pseudo-first-order conditions (7.5 µM Rotaxane-1, 100 µM H_2O_2, 1xPBS pH 7.4) and yielded a rate constant of k = 8.52 x 10^{-3} s^{-1} (Fig.6.3).

To ascertain whether a successful cleavage reaction resulted in a ^{129}Xe hyperCEST signal, multiple concentrations of Rotaxane-2 and H_2O_2 were analyzed to monitor the emergence of the Xe@CB6 signal over time (Fig.6.4). A Xe@CB6 hyperCEST response evolves within one hour of addition of 2 equivalents peroxide (25 µM Rotaxane2, 50 µM H_2O_2), and quickly reaches and maintains an apparent maximum saturation of about 25% (Fig.6.4a). Previous rotaxane-based sensors required 8-24 h to demonstrate the same magnitude of CEST response, demonstrating the notable improvement in efficiency and sensitivity of this system.[54,67]

Titration of Rotaxane-2 (Fig.6.4b) and H_2O_2 concentrations (Fig.6.4c) led to detection limits of 2.5 µM and 5 µM, respectively. Although observed response sizes did increase with increasing Rotaxane-2 or H_2O_2 concentration, they did not seem to be able to achieve more than 25-28% saturation. Meanwhile, at the same acquisition parameters, 5 µM free CB6 that is not previously threaded onto a rotaxane will provide nearly complete saturation immediately. This could be explained by the formation of a CB6 exclusion complex between the carbonyl-laced portal of CB6 and the protonated amine at the end of the cleaved rotaxane as the CB6 dethreads. CB6 is known to form such exclusion complexes with short peptides as well as long diammonium alkanes.[100–102] Although kinetically favorable, the release of CB6 from the rotaxane requires a decrease in entropy as solvation occurs, which involves the association of two or more water molecules by CB6.[101] This intermediate association likely slows xenon entry into CB6 and reduces the CEST response as shown. Although others have reported that such intermediates persist for days to weeks, we cannot at this time conclude whether we are seeing a slow release of CB6 or a dynamic dissociation-reassociation process between CB6 and the cleaved rotaxane. Nonetheless, the successful acquisition of a Xe@CB6 response indicates that enough CB6 is released for xenon exchange in and out of the freed CB6 that is sufficiently fast for examination by hyperCEST.

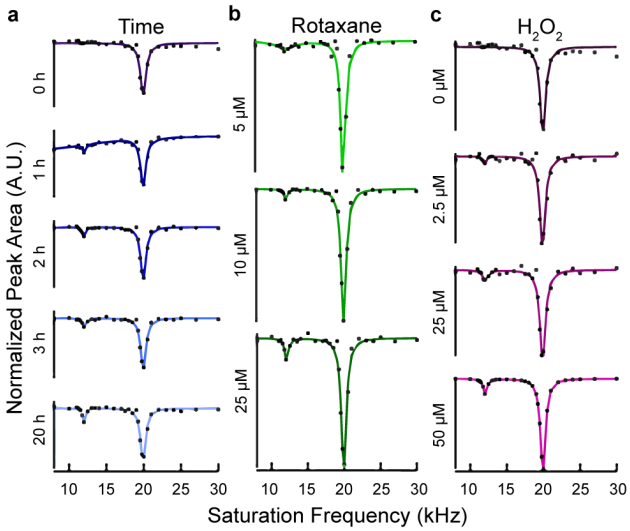

Figure 6.4: Rotaxane-2 acts as a ^{129}Xe hyperCEST NMR probe for H_2O_2. The signal at 20 kHz corresponds to bulk dissolved xenon in water and is always present, but upon addition of H_2O_2 (a), cleavage of Rotaxane-2 releases CB6, leading to the immediate evolution of a Xe@CB6 CEST response at 12 kHz that builds overtime. b-c) Signal can be observed down to 5 µM Rotaxane-2 and 2.5 µM H_2O_2.

The maleimide cap on Rotaxane-2 enabled the functionalization of cysteine residues present on the tobacco mosaic virus (TMV) protein-based nanoparticle and the VCAM-1 binding peptide. VCAM-1 binding peptide was chosen as a model peptide that has implications in inflammatory disease. TMV was chosen as a long circulating nanoparticle that also benefits from a multivalency effect, as up to 34 rotaxane molecules can be conjugated to a single disc. Here, the TMV protein was modified 30% resulting in 10 µM of rotaxane per 1 µM of TMV nanoparticle. Both TMV and VCAM could be easily attached to Rotaxane-2, indicating it can be functionalized with a diverse set of biomolecules (Fig. 6.5). The ability to conjugate these rotaxane-based sensors to macromolecules such as TMV and VCAM-1 enables the collective delivery of a high concentration of probes to a location of interest, which could lead to improved contrast in the targeted area.

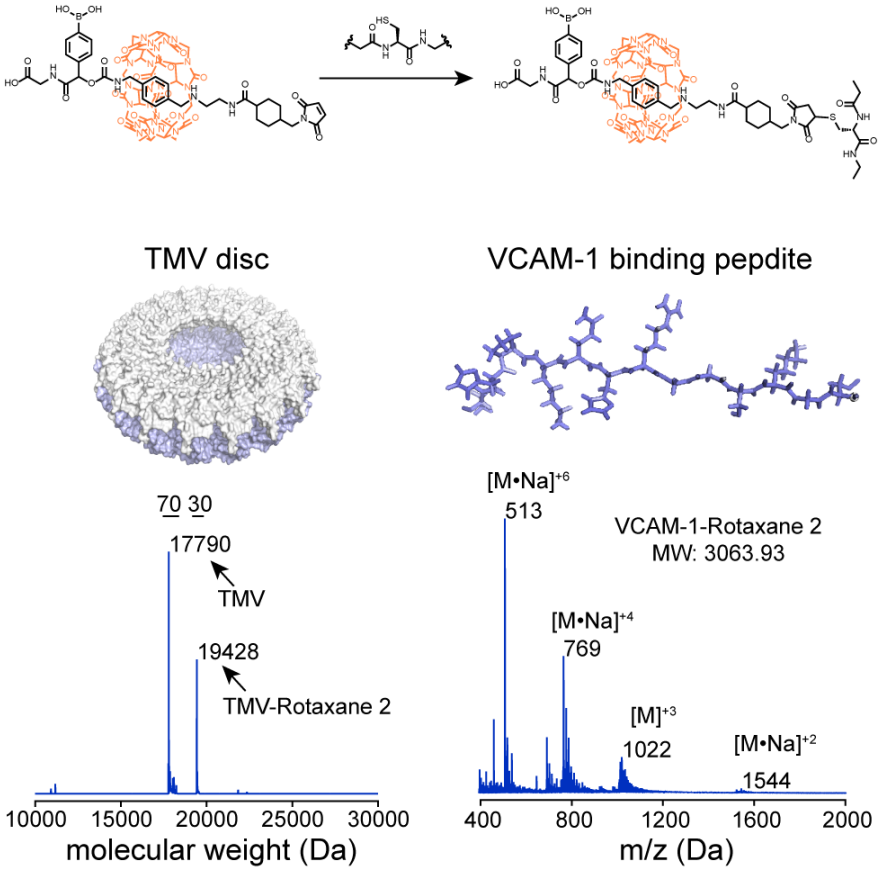

Figure 6.5: Attachment of Rotaxane-2 to proteins and peptides. LC-MS analysis of TMV-Rotaxane-2 with 30% modification. Unmodified TMV protein MW: 17790 Da; TMV-Rotaxane-2 MW: 19428 Da. Mass addition to the TMV protein amounts to 1638 Da, corresponding to Rotaxane-2*2H_2O. The percent modification can be increased or decreased depending on the number of Rotaxane-2 equivalents added. The VCAM-1 binding peptide was 100% modified with Rotaxane-2 and analyzed using LC-MS where the sodiated and non-sodiated adducts corresponding to the (1544 Da) $[M*Na]^{+2}$,(1022 Da) $[M*H]^{+3}$,(769 Da) $[M*Na]^{+4}$, and (513 Da) $[M*Na]^{+6}$ species are observed.

We then sought to detect endogenously produced H_2O_2 by exposing HEK 293T cells to tumor necrosis factor alpha (TNF), a signaling protein involved in immune cell regulation that causes an increase in cellular H_2O_2 production. Secreted H_2O_2 by tumor associated cells is thought to be the method by which cells fertilize the tumor microenvironment and thus drive the reverse Warburg effect, which causes the propagation of reactive oxygen species production from cancer cells to neighboring fibroblasts.[103] Adherent cells in 6 well plates were either exposed to 40 µg of TNF (TNF+) or remained untreated (TNF-). Both samples were incubated for 6 h at 37°C and 5% CO_2. The supernatant was then inoculated with 1 µM TMV-Rotaxane-2 (10 µM Rotaxane2). The samples were examined by ^{129}Xe hyperCEST NMR over the course of several hours (Fig.6.6).

No Xe@CB6 signal evolved for the TNF- sample even after 8 hours, while a response evolved and stabilized after two hours for the TNF+ sample. The Xe@CB6 signal, albeit significantly broadened, persisted even after 24 hours, lending credence to this detection method given the propensity of CB6 to pick up small molecule guests over time.

By comparison with the experiment in which exogenous H_2O_2 was added to HEK 293T cells, we estimate low µM H_2O_2 was expressed as a result of incubation with TNF. This is well within the detection limit of both sensor and target, demonstrating the utility of this technique to detect biologically relevant concentrations.

Whole cell experiments using a HEK 293T cell suspension in complete DMEM media at a concentration of 50,000 cells/mL were then attempted to confirm that the additional tagging of rotaxane-2 by TMV would not affect CB6 release nor xenon accessibility as well as determine whether exogenous H_2O_2 could still be detected by ^{129}Xe hyperCEST NMR in a more chemically complex but biologically relevant environment (Fig. 6.7).

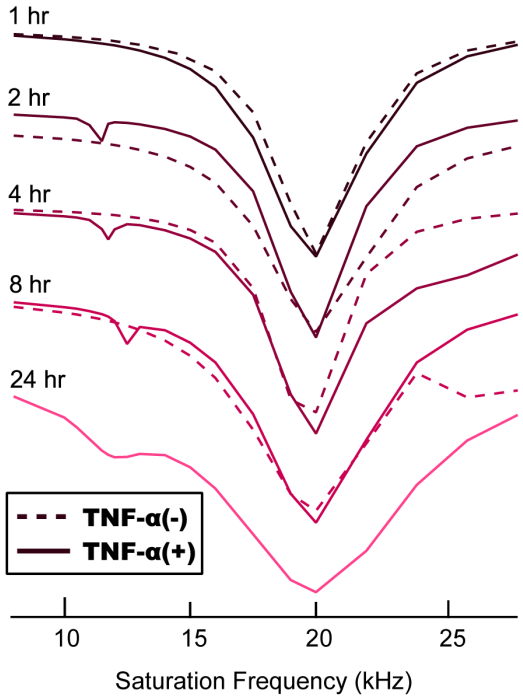

Figure 6.6: TMV-Rotaxane-2 produces a ^{129}Xe hyperCEST signal in response to endogenously produced H_2O_2. TMV-Rotaxane-2 was added to cell supernatant from HEK 293T cells that had (TNF+) and had not been (TNF-) exposed to TNF. The evolution of a Xe@CB6 CEST response at 12 kHz was monitored over 24 h. No Xe@CB6 response appeared for the any TNF(-) samples, while a signal appeared and stabilized within a few hours for TNF+ samples. The % CEST response for TNF+ samples were calculated based on the integrated areas corresponding to the Xe@CB6 (12 kHz) and Xe@ H_2O (20 kHz) peaks.

The molecular complexity of this new environment caused significant broadening of the dissolved xenon response due to shorter correlation times effected by the presence of proteins, but free CB6 could still be detected after the addition of 10 µM H_2O_2. However, due to the complexity of the cell culture media combined with the presence of whole cells, acquisition of this data proved technically difficult: inconsistent foaming of the samples and restricted bubbling due to increased sample viscosity erratically broadened signals or even obliterated signal entirely. Since these effects would not arise in *in vivo* contexts, current work aims to overcome this challenge using engineering solutions such as the membrane device described in Chapter 8.

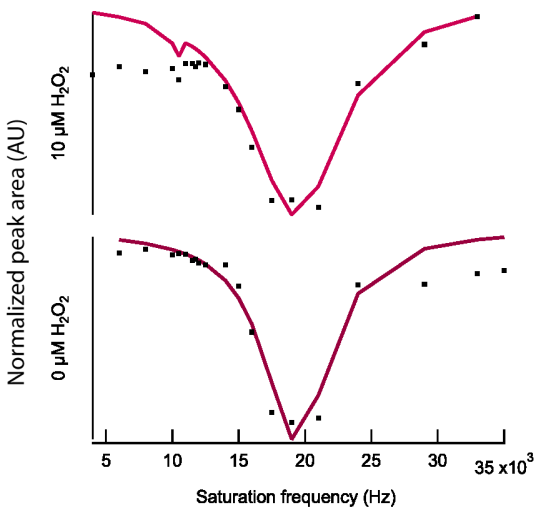

Figure 6.7: ^{129}Xe hyperCEST z-spectra of 0.75 µM TMV-Rotaxane-2 (7.5 µM Rotaxane-2) in a HEK 293T cell suspension in complete DMEM media at a concentration of 50,000 cells/mL with(top) and without(bottom) addition of exogenous H_2O_2. While it appears that whole cell environments may not impede CB6 release, this data remains inconclusive due to the low SNR resulting from this complex biological milieu.

6.4 Conclusion

In summation, we were able to demonstrate the synthesis of a novel CB6 rotaxane that enables the selective detection of endogenously produced H_2O_2 by ^{129}Xe hyperCEST NMR. We aim to extend these results to live-cell imaging, with the intent to progress the technique toward in vivo diagnostic imaging of diseased lung tissue in which peroxide levels are abnormally increased.

Chapter 7

Taking an active role: Directly functionalized xenon biosensors

Case: Selective protein detection via biotinylated cucurbit[7]uril and ^{129}Xe hyperCEST NMR

The available pool of biologically-based xenon biosensors with unique ^{129}Xe chemical shifts has grown substantially diverse. Directly functionalized xenon carriers, such as the large family of cryptophane-based biosensors, are better for localized imaging and provide contrast before and after binding events are detected but remain difficult to synthesize and tend toward aggregation. Indirectly functionalized xenon hosts such as the cucurbituril-based rotaxanes described in the previous chapter allow facile synthesis and have better exchange dynamics for CEST imaging techniques but are as yet invisible until turned 'on' by a binding event and are subject to displacement of xenon by a large variety of small molecules, limiting both *in vitro* and *in vivo* potential. In this study, we investigated a directly biotinylated cucurbituril as xenon probe for the small protein avidin. This sensor gave rise to a hyperCEST response at an unprecedented chemical shift difference (≈28 ppm) when in the presence of its target with up to 55% CEST contrast. This exciting discovery combines the strengths of both families of biosensors, enables a multitude of biological targets due to possibility of avidin conjugation, and also demonstrates a unique advantage of using functionalized cucurbiturils for their stronger interactions with protein surfaces compared to their cryptophane analogues.

7.1 Background

Hyperpolarized imaging agents are particularly attractive for quantitative and targeted contrast magnetic resonance imaging (MRI) applications because their high sensitivity, low background signal, and long relaxation times enable direct visualization of physiologic processes or specific molecular targets. While hyperpolarized ^{3}He gas and ^{13}C- and ^{15}N-labeled agents have continued to demonstrate their potential for clinical application, hyperpolarized

^{129}Xe gas remains at the forefront for targeted molecular imaging.[13] As a contrast medium, xenon is attractive because it is inert, exogenous, and non-toxic- in fact, it has been in use as an anesthetic gas for decades. Further, it has good aqueous solubility, and has a high polarizability that makes it very sensitive to its local chemical environment.[14–16] As we now know very well, ^{129}Xe nuclei can be hyperpolarized by spin exchange optical pumping to increase signal by 4–5 orders of magnitude compared to thermal polarization, which enables imaging at modest dissolved xenon concentrations.[2] Thus, compared to conventional MRI techniques, hyperpolarized ^{129}Xe MRI yields practical detection limits of small biological targets without the risks associated with ionizing radiation.

Molecular hosts with which xenon atoms transiently associate have enabled selective, localized and multiplexed detection of a diverse range of biological targets. Xenon atoms exchange in and out of the hosts and can act as a reporter of the hosts' chemical environment through changes in ^{129}Xe chemical shift or relaxation. When hosts interact with a specific biological or chemical target, they give rise to distinct ^{129}Xe NMR signals. Ideally, both the unbound and bound biosensors have resolved xenon signals, enabling quantitation of concentration and kinetic parameters.

These xenon-host ensembles, termed biosensors, currently come in a variety of structural flavors, with the two major classes (supramolecular compounds and larger compartmental carriers) encompassing most (See Chapter 3 for a list of current biosensor types and references [19, 20, 104] for a few recent examples. This ever-expanding array of xenon biosensors has been applied to the selective detection of a variety of binding events involving receptors on cell surfaces, transmembrane proteins, enzymes, and reporting on microenvironments indicative of tumors, such as abnormal pH, specific ionic milieus or oxidation.[20,57,104–108]

Application of chemical exchange saturation transfer (CEST) techniques to hyperpolarized xenon (hyperCEST) has furthered detection limits of biosensors to nano- and picomolar scales.[17] Instead of using labile protons on amides or water molecules, which can only provide detection limits down to mM concentrations, hyperCEST exploits the fact that thousands of xenon atoms can exchange in and out of a biosensor in one saturation cycle, greatly lowering the concentration requirements of both xenon hosts and biological targets for detection. Recent developments in ultra-fast hyperCEST imaging have made the prospect of fast, selective, and sensitive hyperpolarized ^{129}Xe MRI not only viable but even advantageous.

Cucurbiturils (CBns) comprise a class of promising hosts for ^{129}Xe hyperCEST MRI due to their commercial availability and favorable xenon exchange kinetics.[66] As described in Chapters 3 and 6, CBns are donut-shaped molecules comprised of n glycouril units linked by methylene bridges (Fig.7.1a, CB7 shown). For some time, derivatives of the six-membered structure, CB6, have been the "Goldilocks" hosts for CBn-based ^{129}Xe hyperCEST studies, although CB7 has recently shown promise as a faster-exchanging, alternative host.[108] Exchange rates of these cages with xenon are low enough ($\approx$2 kHz) to be within the slow-to-intermediate exchange regime, thus yielding a unique chemical shift associated with xenon

residing in CB6 or CB7, but also large enough to benefit from signal enhancement via hyperCEST.

However, CB6 has poor aqueous solubility compared to CB7, and both can bind nonspecific guests that exclude xenon.[61] Further, the difficulty of functionalizing CBns has restricted CBn-based biosensors to indirect detection methods, those in which the sensors remain inaccessible to xenon until some specific event "unlocks" them. The CBn moieties are then identical when active, meaning all such sensors will have the same chemical shift upon interaction with their target.[19,54,67]

Currently, CBns are better known for their utility as drug carriers that improve chemical stability and solubility of their drug payload.[61,62,65] Further, CB7 has shown utility for controlled release of drugs in cancerous cells.[64] Cao et al. reported synthesis of a directly biotinylated CB7 (btCB7, Fig.7.1a) as a carrier for anti-cancer drugs to murine lymphocytic leukemia (L1210FR) cancer cells, which overexpress biotin receptors.[109] The drug-btCB7 complexes demonstrated improved targeting specificity and cytotoxicity to L1210FR cells, while preserving healthy tissue and preventing side effects associated with non-selective toxicity.

In this study, we investigated btCB7 as a potential xenon biosensor for the small protein avidin, for which biotin has a very high affinity ($K_a \approx 10^{15}$ M^{-1}), with the aim of combining the target specificity conferred by directly functionalized xenon biosensors with the optimal hyperCEST characteristics of CBns. Specific detection of avidin makes possible biosensor customization, as avidin can be conjugated to other proteins and/or with other detection agents.[110]

7.2 Methods

7.2.1 Sample preparation

BtCB7 (Dr. Liping Cao, Isaacs Group, Dept. of Chemistry and Biochemistry, UMD), biotin (Sigma-Aldrich), and avidin from egg white (Sigma-Aldrich, Rockland) were each received as solid powders and dissolved in phosphate-buffered saline solution before use. For avidin titration experiments, the amount of avidin was increased, while the concentration of btCB7 remained constant (50 µM). Ratios were calculated based on number of binding sites per avidin molecule and given equilibrium conditions. MALDI data was acquired from a Bruker microflex LT instrument.

7.2.2 Xenon HyperCEST experiments

Xenon hyperpolarization and delivery was achieved on two xenon polarizer setups and described in detail below.

Table 7.1: HyperCEST spectrum acquisition parameters

Institution	%Xe	Pressure (b)	Flow (SLM)	Magnet system	Saturation pulse	B_1 power (mT)
1	2-5	3.51	0.1 (bypass: 0.25)	400 MHz Bruker Biospin	0.02-0.05 W, 5 s	0.35
2	2	4.00	0.2 (no bypass)	400 MHz Varian VNMRS	0.015 W, 4 s	1.9

1 - Leibniz Institute; 2 - UC Berkeley

In general, mixtures of 2-5% Xe (26.4% natural abundance ^{129}Xe), 10% N_2, and balance He were flowed through a spin-exchange optical pumping setup at 0.1-0.2 SLPM. Once hyperpolarized, the gas was bubbled directly into phantoms containing the samples via glass capillaries for 10 s. A settling time of 3-5 s allowed bubbles to disperse. Then, a standard hyperCEST experiment was performed: The saturation pulse frequency was swept from 4-40 kHz in 5.5-27.5 kHz steps between transients to encompass all Xe CEST responses. Specific pulse sequence parameters are denoted in Table 7.1. Due to the high sensitivity of Xe to very low CB7 concentrations and the tendency for CB7 to adsorb on glass surfaces, dummy samples were examined between experiments to assure that no contamination contributed to observed CB7 signals.

Data processing for these datasets was a bit different from that of previous work. To acquire ^{129}Xe hyperCEST z-spectra, saturation frequencies were arrayed so any exchange of xenon between bulk water and cages appeared as reduction in the dissolved xenon resonance when the saturation frequency matched the frequency corresponding to the caged xenon chemical shift. Each FID in hyperCEST datasets was processed by integrating the area of the FID for each saturation frequency, then dividing by the largest area in the set to normalize. All areas are then plotted versus saturation frequency to yield a z-spectrum. All z-spectra for a given sample were averaged then subjected to fitting by way of a least-squares iterative fit function applied to a simple Lorentzian model (See the Appendix for more details on the fits).

%CEST effect values were calculated from the data after normalization but before any fits were applied. The average ^{129}Xe hyperCEST response values at 40 ppm (the resonance corresponding to xenon in avidin-bound btCB7, 'on'), were calculated for all trials and subtracted from those at -40 ppm ('off') to account for any symmetric broadening effect about the dissolved response caused by titration of avidin concentration in the samples. Error bars were calculated by finding the percent error for each of the on/off averages then propagating error through the difference calculation.

7.2.3 Computational modeling

BtCB7 structures were built in Maestro (v. 2018-1) and subjected to minimization and conformational searches using the Macromodel conformational search tool with the OPLS-2005 force field. The monomeric avidin structure was obtained from the Protein Database (PDB ID: 2AVI) then run through minimization and Protein Prep Wizard in Maestro. BtCB7

docking on avidin was accomplished by Induced Fit calculations using the OPLS-2005 force field. Molecular dynamics simulations for monomeric, dimerized, and avidin-bound btCB7 were prepared in orthorhombic boxes of 0.15 M NaCl(aq) with Cl^- added to neutralize any charge and applying the SPC solvent model. Xenon atoms were modeled by using the van der Waals radii of I^- atoms and setting their charge to 0. Several iterations of 100 nanosecond trajectories using an NPT ensemble at 293K and 1.013 bar were simulated in Desmond.

7.3 Results

As a first step we examined whether biotinylation affected the observable ^{129}Xe hyperCEST signal for xenon inside btCB7 (Xe@btCB7), Figure 7.1. As a control we first measured the hyperCEST response from unmodified CB7, Figure 7.1b, which is very similar to that reported previously by Schnurr et al.[108] For Xe@btCB7 the response is again at -68 ppm, but is significantly weaker than that for unmodified CB7 (Fig.7.1b). Both hyperCEST signals are meager compared to typical CB6 responses at the same concentration. CB6 responses observed by others are fairly broad, which is attributed to facile exchange from the central cavity (diameter = 5.8 Å).

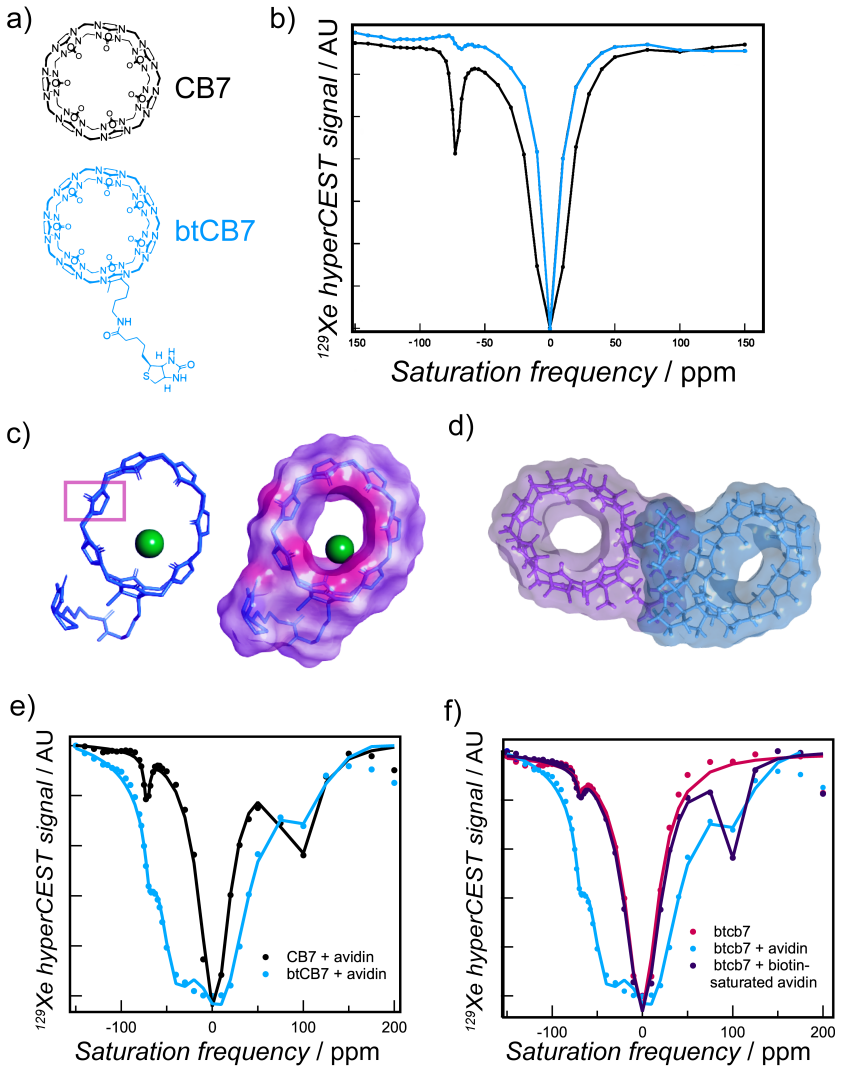

Figure 7.1: a) Structures of unmodified and biotinylated (bt-)CB7. b) A ^{129}Xe hyperCEST z-spectrum shows that both structures provide a similar chemical environment for xenon at -68 ppm, but that the population of xenon in btCB7 is greatly reduced. Conformational searches followed by MD simulations of btCB7 in monomer and dimer forms indicate that c) a btCB7 with an inverted glycouril unit (ibtCB7, highlighted) may make xenon capture possible in this relatively larger CBn, but d) ibtCB7 dimer formation may restrict xenon exchange. The small signal for the free sensor may therefore be due to low concentration of ibtCB7 relative to btCB7, limited exchange resulting from dimerization, or both. e) Unlike unmodified CB7, btCB7 gives rise to a new signal at -40 ppm when avidin is introduced. f) This signal does not appear when avidin is pre-saturated with biotin, indicating that the signal at -40 ppm is from xenon in avidin-bound btCB7

For CB7, with a larger diameter of 7.3 Å exchange should be even faster, and in that case a much broader Xe@CB7 signal is expected. Additionally, the broadening of the water dissolved xenon at 0 ppm is larger than expected given the width and intensity of the bound

xenon peak. As such, we believe that the peaks at -68 ppm arise from a known, low-population (≈1%) stereoisomer iCB7, in which a single glycouril unit is inverted (Fig.7.1c-d).[111] The 'inverted' CBns (iCBns) have a reduced internal cavity size relative to the normal CBn, ≈ 5.5 Å diameter for iCB7, and a preference for smaller guests. The smaller cavity explains the presence of weak, relatively sharp, CEST Xe signal from ibtCB7. We believe that the CB7 bound xenon resonance is too broad to directly detect, but the presence of Xe in CB7 is manifested through broadening of the water dissolved xenon peak.[111]

The Xe@ibtCB7 signal is significantly weaker than that from Xe@iCB7. Given that both structures have the same xenon chemical shift, their internal cavitiy environments are likely equivalent. It is possible that less ibtCB7 was formed during its synthesis than iCB7 during unmodified CB7 synthesis. Yields of the inverted isomer are reported as somewhat variable.[111] Alternately, xenon binding to ibtCB7 could be inhibited by an exclusion complex between ibtCB7 and its own biotin tail or that of another ibtCB7. CBns are known to form such exclusion complexes with short peptides as well as long diammonium alkanes,[101] but our MD simulations showed that the biotinylated tail does not appear to obstruct the CB7 portals (Fig 7.1c, right). The original report of btCB7 showed that it self-associates as dimers in solution, making the exclusion of xenon by aggregation another potential source of CEST response suppression.[109] MALDI analysis of our samples supports the presence of dimers (Fig.7.2), and further MD simulations show that two proximal btCB7 molecules quickly form persistent dimers where the biotin tails rest atop one another (Fig.7.1d). Avidin binding is strong and disrupts btCB7 dimerization.[109] Both monomeric and dimeric ibtCB7 modeled environments showed transient deformation of the CB7 portion of ibtCB7 around bound xenon atoms. This result is in line with previous work demonstrating the propensity of CB6 for flexing to accommodate guest molecules due to the thermodynamic benefit of freeing high energy water from its inner volume.[102,112]

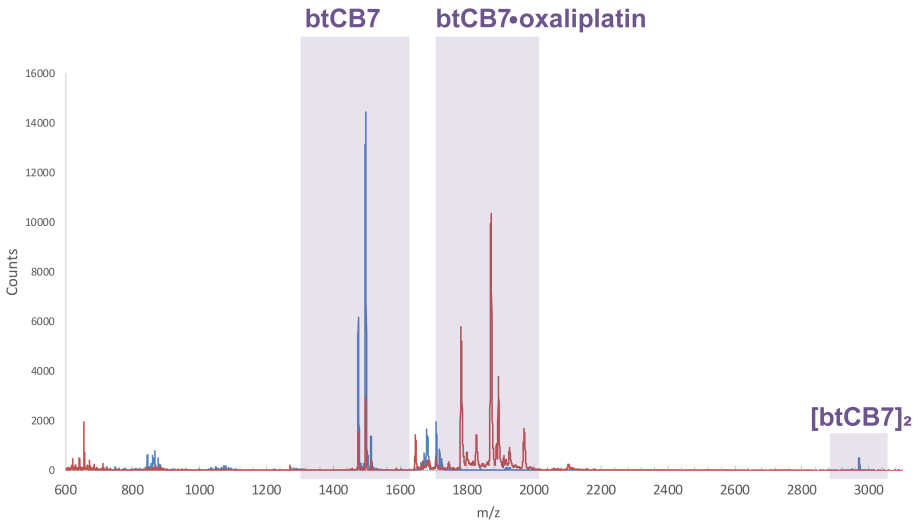

Figure 7.2: MALDI spectrum of btCB7 before (blue) and after (red) addition of excess (2:1) oxaliplatin. btCB7 calc: 1474.42, obs: 1474.44; btCB7*Na calc: 1497.41, obs: 1495.63; [btCB7]2*Na calc: 2971.83, obs: 2971.0; btCB7*oxaliplatin calc: 1871.70, obs: 1871.00

To evaluate the potential as a biosensor we studied btCB7 bound to avidin. Avidin is a homotetramer of ≈ 68 kD that contains one biotin receptor on each of its four subunits.

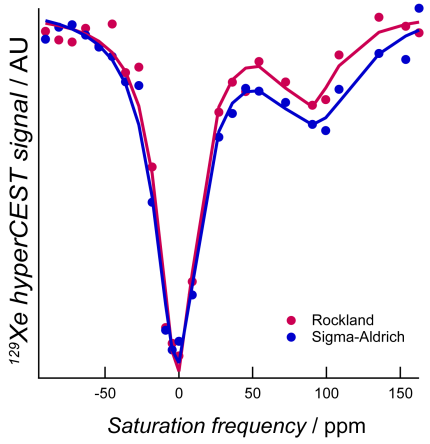

Figure 7.3: A broad signal at 100 ppm appears in a xenon z-spectrum of a sample of 12.5 µM avidin in 1.5 mL phosphate-buffered saline. This peak persisted for different suppliers (Sigma-Aldrich and Rockland) and batches of avidin.

Samples were made with 0.5 to 2 equivalents of biotin receptors relative to the btCB7, which was maintained at 50 µM. Upon the addition of avidin to samples containing btCB7, we observed four distinct signals as shown in Fig.7.1e-f. The Xe@ibtCB7 and water-dissolved xenon signals are seen at -68 ppm and 0 ppm, along with new signals at roughly -40 ppm and 100 ppm. We attribute the response at 100 ppm to the interaction of xenon atoms with avidin directly. In experiments with xenon in solution with only avidin this signal is present (Fig.7.3). It is well known that xenon binds to hydrophobic pockets and channel pores in proteins.[16,40] Recently, binding of xenon to maltose binding protein and TEM β-lactamase was observed by ^{129}Xe NMR, giving generally similar shifts (60-95 ppm downfield of the dissolved xenon resonance).[113,114]

The substantial response at -40 ppm is assigned to btCB7 bound to avidin (Xe@btCb7-avidin). To verify this we performed a number of controls: there was no signal at -40 ppm for unmodified CB7 in the presence of avidin (Fig.7.1e), or for btCB7 in the presence of avidin that was pre-saturated with biotin (Fig.7.1f).

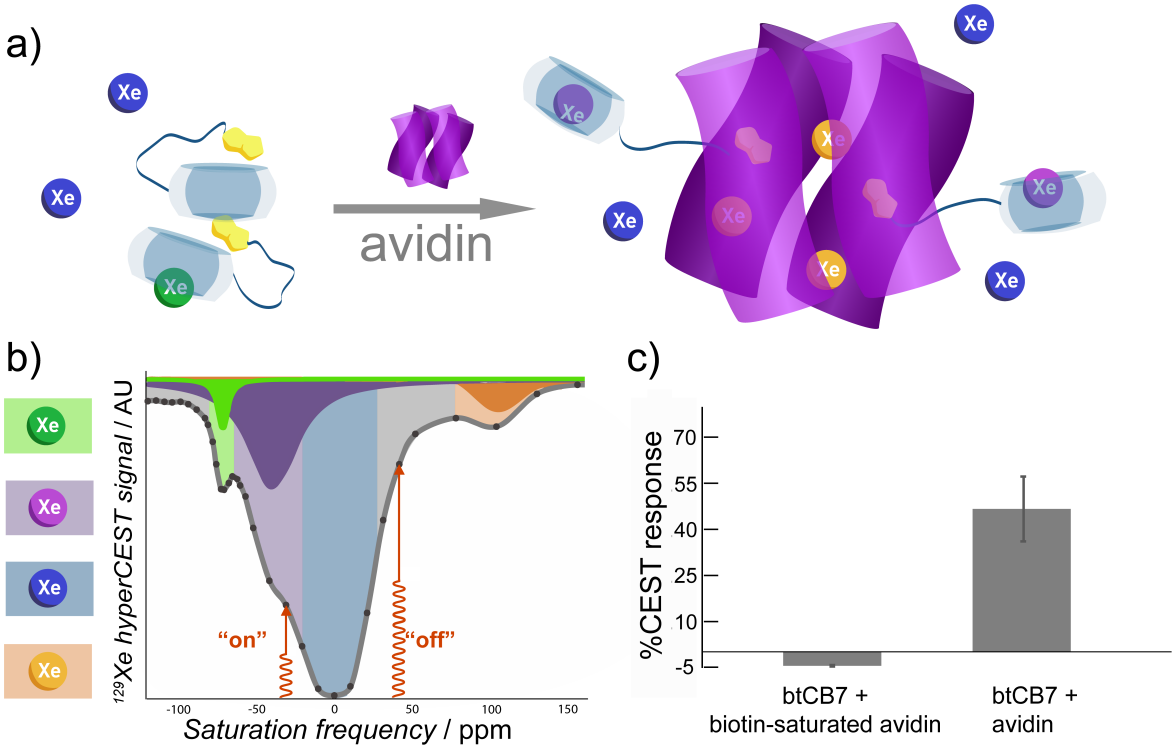

Figure 7.4: a) Four distinct xenon populations in this system can be identified in b) a ^{129}Xe hyperCEST z-spectrum (1:1 ratio of 50 µM btCB7 to avidin binding sites shown). The largest population of xenon is dissolved in the solvent (blue, 0 ppm), to which the chemical shifts of all populations are referenced. Some xenon undergoes exchange with ibtCB7 (green, -68 ppm). Upon addition of avidin, btCB7 binds to the protein, leading to a response for the btCB7-avidin complex (purple, -40 ppm). Xenon also interacts directly with avidin (orange, 100 ppm). c) CEST contrast gained as a result of adding avidin is evaluated by subtracting the 'off' signal at the position equal and opposite the dissolved xenon resonance at 40 ppm from the 'on' signal at -40 ppm, corresponding to btCB7 bound to avidin.

The assignments of the other CEST signals to other species are shown in Fig.7.4a-b. Increasing the avidin concentration yielded a larger signal at -40 ppm, but broadening of the xenon in solvent response made direct quantification difficult (Fig.7.5, top left). We performed Lorentzian fitting of the full spectra, which allowed for the separation and estimation of each population's contribution (Fig.7.5). This confirmed that the magnitude of the avidin bound btCB7 response increased for increasing amounts of avidin relative to biosensor.

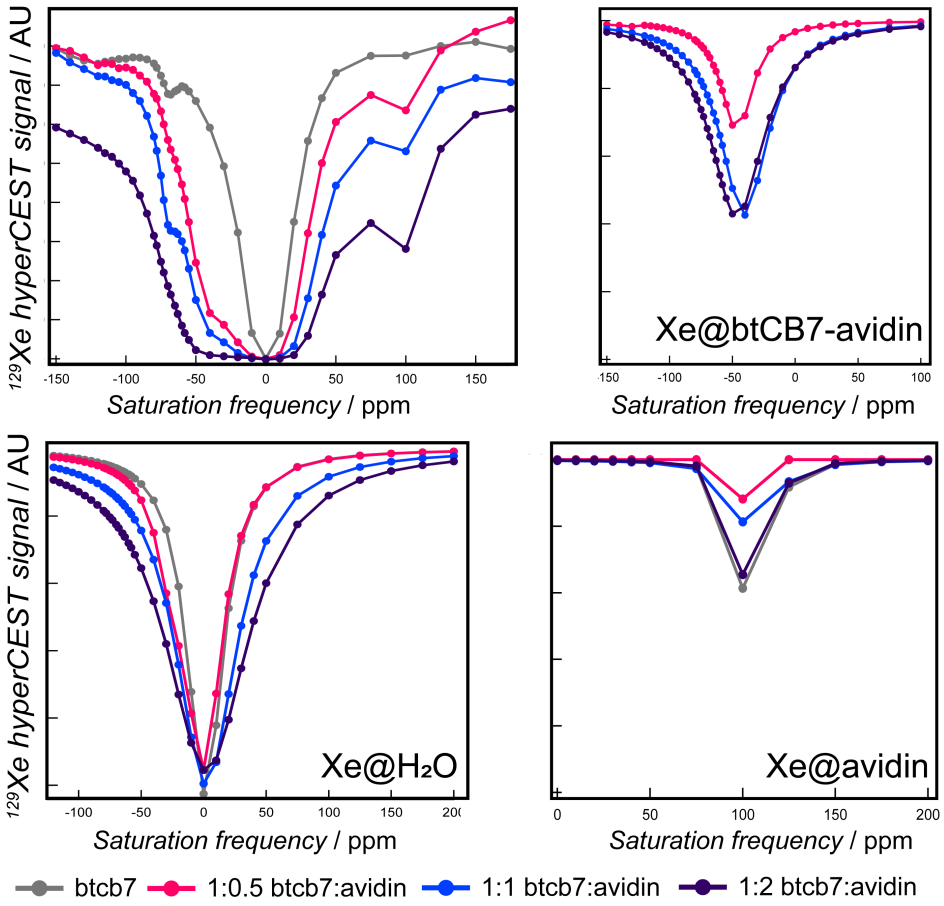

Figure 7.5: ^{129}Xe z-spectra show that increasing amounts of avidin lead to a larger Xe@btCB7-avidin response, but it is unclear from the full spectra how much response depth is due to broadening of the dissolved response. 50 µM btCB7 was used for all samples with amount of avidin being titrated. Ratios correspond to moles of btCB7 relative to avidin binding sites. Signals for each xenon population are deconvoluted from full z-spectra by applying Lorentzian fits, which reveal that increasing the amount of avidin appears to proportionally increase the magnitude of the signal corresponding to avidin-bound btCB7. Important to note is the apparent drifting of chemical shift in the Xe@btCB7 data. This is a result of the fitting function's difficulty with separating out the overlapping peaks, and not observed in data before fitting. This makes interpretation of these fits best for only qualitative comparisons.

Further verification that the signal at -40 ppm arises from btCB7 was provided by addition of the drug oxaliplatin, known to bind CB7 with high affinity ($\approx 10^8$ M^{-1}).[109] With drug bound the CB7 cavity is filled, displacing any xenon and preventing rebinding. Consistent with this addition of oxaliplatin to the btCB7-avidin sample led to loss of the signal at -40 ppm. This experiment also supports the assignment of the peak at -68 ppm as arising from iCB7. The smaller cavity from the inverted isomer of the CB7 cannot bind oxaliplatin, and the -68 signal is not affected by addition of the drug (Fig.7.6 and Fig.7.7).

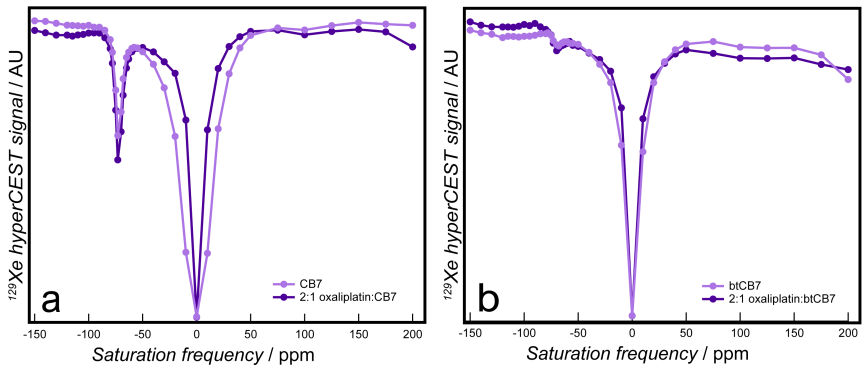

Figure 7.6: Z-spectra of 50 µM a) CB7 and b) btCB7 before and after addition of 100 µM oxaliplatin. In both cases, no signifcant effects on the Xe@cage response are observed. In the case of CB7, the dissolved xenon response narrows, indicating reduced exchange and implying that some CB7 may be effectively blocked by oxaliplatin.

Having identified the signal from btCB7 bound to avidin, we estimated imaging contrast potential by comparing 'on' versus 'off' resonance CEST to the xenon in solvent peak (Fig. 7.4c). Saturation at the frequency of btCB7 bound to avidin (-40 ppm, 'on') compared to the control (40 ppm, 'off') generates ≈ 55% CEST difference, which is sufficient to provide significant imaging contrast. To help understand the avidin bound Xe@btCB7 signal we performed docking and MD simulations on the btCB7-avidin complex in the presence of xenon (Fig 7.7, top).

These simulations showed that btCB7 fits into the biotin binding pocket of monomeric avidin with the CB7 moiety resting snugly between the loops L3,4 and L7,8 in the monomer. Such interactions may slightly occlude the CB7 and slow the xenon exchange such that a broad but clear resonance from it can be observed via CEST. Xenon atoms were also observed in pockets of the avidin (orange), Fig.7.7. Simulation trajectories confirmed that the CB7 portion of avidin-bound btCB7 experiences dynamic deformation that is more pronounced than its unbound counterpart (Fig. 7.8).

The short tether between CB7 and biotin appears to hold the CB7 in close proximity to the protein surface. These results support contact-mediated cage deformations as a source of the relatively downfield ^{129}Xe chemical shift for btCB7 bound to avidin, as has been seen for somewhat analogous xenon biosensors.[79,115,116] The ability to achieve close proximity of these cages to protein targets makes functionalized CB-based biosensors very attractive for imaging applications.

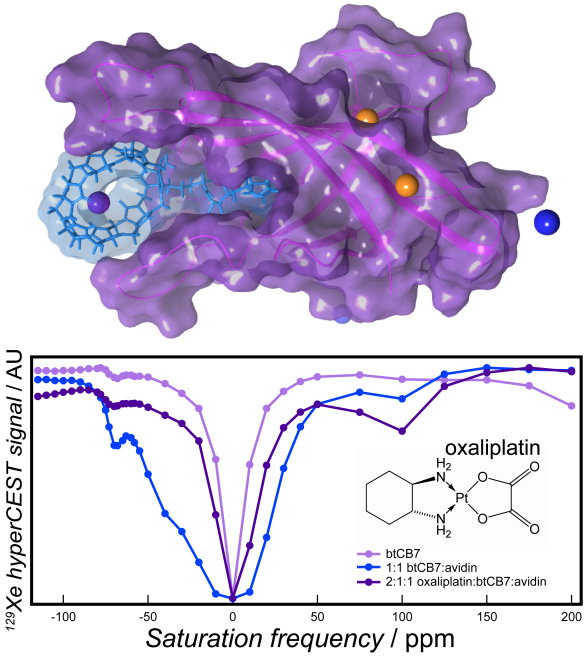

Figure 7.7: Top: Docking and MD simulations show that btCB7 fits into the biotin binding pocket of monomeric avidin with the CB portion resting between the L3,4 and L7,8 loops. Xenon atoms transiently caught in hydrophobic pockets of the monomer itself were also observed. Bottom: ^{129}Xe hyperCEST spectra of 50 µM btCB7 before and after addition of 100 µM oxaliplatin in the presence of avidin. Addition of oxaliplatin results in the disappearance of the avidin-bound btCB7 response at -40 ppm, indicating that oxaliplatin blocks xenon from the avidin-bound sensor while the unbound signal is unaffected.

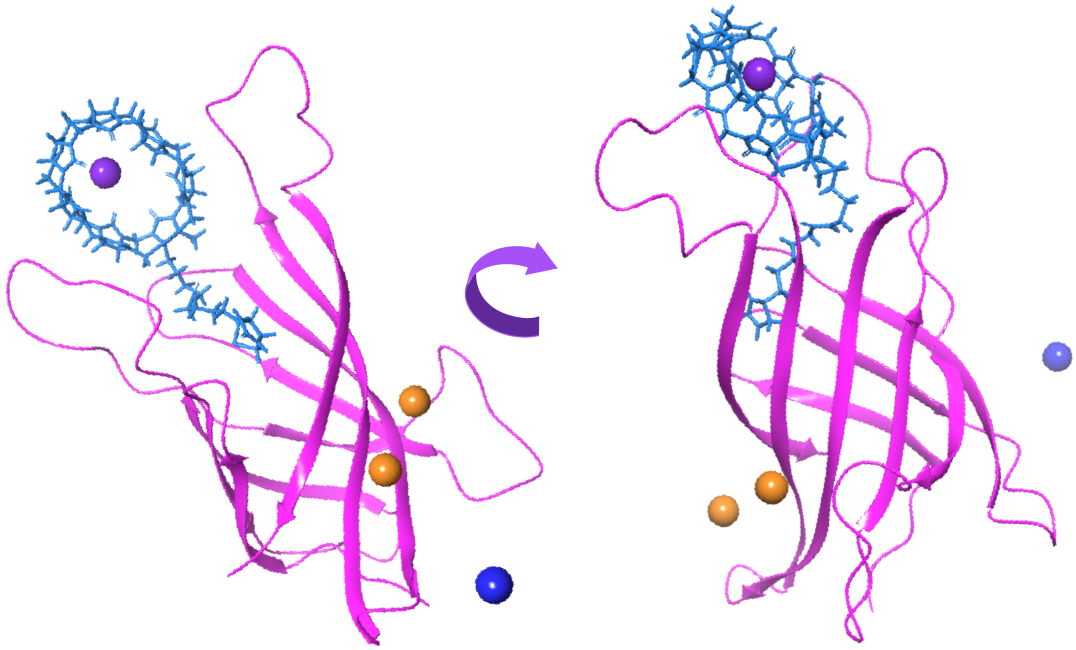

Figure 7.8: Additional snapshots of the bound btCB7-avidin structure show the additional deformation on the CB7 portion of btCB7 due to proximity to the protein surface.

7.4 Conclusion

In summary, the first example of a directly functionalized cucurbituril used for detection of a specific protein target by ^{129}Xe hyperCEST was presented. This work additionally lays the foundation for detection of many biological target through the use of avidin conjugation (e.g. to targeting antibodies).These observations support the potential for cucurbituril-based xenon biosensors to selectively, sensitively and potentially simultaneously report on multiple pathological markers in a single ^{129}Xe imaging session. The utility of this particular tool can be furthered by its use as an MRI reporter for biological target location and, potentially, *in vivo* monitoring of drug uptake into target cells.

Chapter 8

Oh, the places you'll go: Creating a device that exposes hyperpolarized xenon to new chemical environments

Case: Non-Disruptive Dissolution of Hp-^{129}Xe into Viscous Aqueous and Organic Liquid Crystalline Environments

As exciting as it is to see the different types of xenon biosensors proliferate, we must maintain focus and investment in making sure these probes are as effective in complex biological milieu as they are in simple buffer solutions. Because hyperpolarized xenon (hereforth hp-^{129}Xe) has a finite lifetime, it is imperative that we develop methods for delivering it to biological targets before it relaxes. As such, one challenging aspect of biological samples are their tendency to be highly viscous. Most xenon biosensors are delivered to samples by bubbling, which is not possible for viscous whole blood, plasma, saliva, or even dilute protein samples.

This chapter covers work we've done to develop a device that enables the dissolution of hyperpolarized xenon into viscous aqueous aqueous and organic samples without bubbling. This method is robust, requires small sample volumes ($\leq$60 µL), is compatible with existing NMR hardware and made from readily-available materials. We even detected dissolved xenon in an aqueous liquid crystal that is disrupted by the shear forces of bubbling, and we observed liquid-crystal phase transitions in MBBA. Ultimately, this tool allows an entirely new class of samples to be investigated by hyperpolarized-gas NMR.

8.1 Background

As has been thoroughly demonstrated by now, hp-^{129}Xe has proven to be an effective reporter for many biological and chemical systems, including *in vivo* medical imaging.[17,28,39,108] However, xenon NMR is also useful in material science as a highly sensitive, inert probe for

properties of liquid crystal (LC) phases, nanochannels and porous structures, and as a real-time reporter for the progress of chemical processes.[32–37] Anisotropic chemical environments such as LC phases can cause substantial shielding anisotropy in the xenon chemical shift tensor.[31] This is due to deformation of xenon's electron cloud caused by the ordering of molecules near it. In an isotropic environment, unrestricted molecular tumbling averages this contribution to zero. When molecular motion is constrained by electrostatic, steric, or other non-covalent interactions in an ordered phase, an anisotropic contribution, proportional to the degree of LC order, adds to the observed ^{129}Xe chemical shift. For thermotropic LCs like N-(4-methoxybenzylidene)-4-butylaniline (MBBA), for example, the degree of positional ordering and angle of the director axis with respect to the external field can be deduced from the xenon chemical shift anisotropy via variable temperature studies.[32,117]

In addition to materials applications, the ability to study LC phases via hp-^{129}Xe NMR may become advantageous for biosensing. NMR studies with hp-^{129}Xe require rapid delivery to avoid loss of signal through relaxation before detection. Hp-^{129}Xe has usually been introduced into samples through bubbling or shaking of Xe gas mixtures with the solution of interest, but these approaches are incompatible with viscous and/or easily damaged solutions such as liquid crystals or cell suspensions.[52–55,89,115,118–121]

One such alternate approach has been to flow the solution of interest around Xe permeable membrane tubes pressurized externally with hp-^{129}Xe, then into the NMR probe, e.g. over alginate beads containing cells.[55] This family of setups relies on the ability to pre-dissolve hp-^{129}Xe into a flowing transport medium that is later added to a sample of interest in the magnet.[122–126] Unfortunately, this approach is also incompatible with highly viscous or shear sensitive solutions.

By contrast, the dissolution of xenon into stationary liquids has been accomplished two ways: first, by pressurization with thermally polarized (TP-), isotopically-enriched, pure xenon sources,[31,80,127] and second, by using porous polypropylene hollow membrane fibers.[36] Until now, the only way to visualize viscous media by ^{129}Xe NMR was via TP-xenon pressurization, which is costly and often time-consuming compared to hp-^{129}Xe experiments. In the latter case, the solutions studied were neither viscous nor sensitive to agitation. We have also noted that polypropylene hollow fibers tend to rupture and break easily compared to silicone, often leading to the generation or trapping of bubbles in viscous samples.

To enable hp-^{129}Xe studies of viscous, ordered or otherwise mechanically sensitive solutions we developed a new method for direct dissolution of hp-^{129}Xe into any solution via a silicone gas-exchange membranes, *in situ* in the NMR spectrometer.

8.2 Methods

8.2.1 Membrane assembly construction

The assembled membrane device is shown in Fig.8.1. Polydimethylsiloxane (PDMS) silicone hollow membrane fibers of ID 190 µm, OD 300 µm (thickness: 55 µm) were obtained from PermSelect. 27-30 membrane fibers were cut to a length of 4 cm and rolled around a translucent polyimide tube of ID 61 µm, OD 86 µm (Amazon Supply, Catalog # B0013HMU8O), which was cut to a length of about 18 cm and inserted into a custom-designed, 3D-printed flow director comprised of a proprietary material (Somos WaterShed XC 11122, Proto Labs).

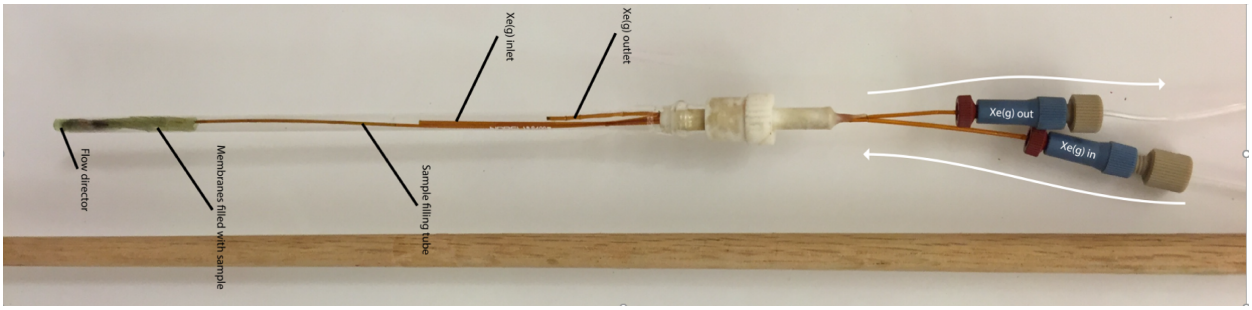

Figure 8.1: Membrane assembly for hp-^{129}Xe experiments.

Fig.8.2 shows a schematic of the flow director design. The flow directors were approximately 3.5 mm in diameter and 3.35 mm in length. The hollow fiber and polyimide tube bundle was inserted such that an empty space remained between the bundle and the bottom of the flow director. This assured that any sample introduced into the polyimide tube would be able to enter the hollow membrane fibers after reaching the flow director.

The interface between the hollow fibers and the flow director was sealed with medical-grade epoxy (Loctite M-21HP Hysol) and allowed to cure overnight. Samples were manually injected into the assembly via a syringe attached to the polyimide tube by PEEK microfluidic fittings (NanoPort Assemblies). The sample entered the flow director, then filled the membrane fibers from bottom to top. Successful filling of the membranes was easily observed due to their transparency. The assembly, approximately 4 mm total in diameter, requires less than 60 µL of sample to fill all the hollow membrane fibers. Membranes were flushed with water or cyclohexane to wash.

8.2.2 Preparation of membrane assembly for Hp-^{129}Xe experiments

Once filled with sample, the whole assembly was inserted into a 5 mm NMR tube (Fig.8.1. The NMR tube was sealed with a Teflon fitting containing both an inlet and an outlet for

Xe gas comprised of the same polyimide tubing used above. The gas inlet tube was secured to 1/16" PEEK tubing by microfluidic fittings that delivered hyperpolarized xenon directly from the polarizer to the sample tube. The gas outlet tube was connected to 1/16" PEEK tubing leading to a mass flow analyzer (Aalborg).

8.2.3 Sample Preparation

Solutions of 3% deuterated benzene (Isotec) by volume in N-(4-methoxybenzylidene)-4-butylaniline (MBBA, Sigma-Aldrich) were used for studies of solute ordering via ^{2}H and ^{129}Xe NMR inside the membranes.

Solutions of 10% v/v $^{2}H_2O$ (Sigma-Aldrich) in 0-30 mg/mL pf1 bacteriophage (Asla Biotech) were prepared by diluting phage with deionized water. All phage experiments were carried out at 15°C.

8.2.4 NMR experiments

Hyperpolarized ^{129}Xe was generated by spin-exchange optical pumping of a gas mixture of 2% Xe, 10% N_2, and 88% He (Airgas) using the homebuilt polarizer described in Chapter 4. Hp-^{129}Xe flowed directly into 5 mm or 10 mm valved NMR tubes for the pf1 phage and the MBBA samples, respectively, at 0.2 SLPM held at 240 kPa for all experiments. All NMR data were acquired on a 9.4 T magnet with a Varian VNMRS console.

^{129}Xe experiments were carried out using a multiple-acquisition, selective-excitation sequence with a center frequency at 17 kHz relative to the resonance frequency of ^{129}Xe gas at 9.4 T (≈110 MHz) and a bandwidth of 5-8 kHz. Between 4 and 8 transients were collected per repetition, followed by a 10-second delay during which hp-xenon inside the phantom was replenished. A fitting with a glass capillary allowed the flow of hyperpolarized xenon from a homebuilt polarizer to the bottom of the phantom. Spectra were referenced to the Xe gas peak.

^{2}H data were acquired with xenon flowing through the system to assure that observed ordering was maintained in the presence of xenon. A basic pulse-acquire sequence with a pulse length of 17.5 µs (5 mm probe) or 34 µs (10 mm probe) and a 1 s delay between transients was used. In the variable temperature studies of MBBA, temperatures were swept from low to high. An equilibration time of about 40 minutes was used after each temperature increase to ensure equilibration inside the membranes such that ^{2}H quadrupolar splittings remained constant.

8.3 Results

A schematic of the assembled setup is shown in Fig.8.2. Refer to the Fig.8.1 in the Methods section of this chapter for a detailed description of the construction and experimental procedure using this device. In short, the sample is injected by syringe through a polyimide fluid inlet tube and into the membranes via a plastic flow director cap. Compared to previous xenon dissolution work, the positions of the hp-^{129}Xe gas and sample are reversed in our assembly: where other devices had xenon flowing from the inner volume of hollow fiber membranes to a surrounding sample liquid, we elected to place the sample inside the hollow fibers surrounded by hp-^{129}Xe gas.[36,122–126] By placing the sample inside the membranes and selectively exciting the dissolved xenon resonance, we utilize our pool of hyperpolarized xenon gas more efficiently compared to previous membrane-based dissolution setups while also requiring significantly less sample compared to typical bubbling experiments.

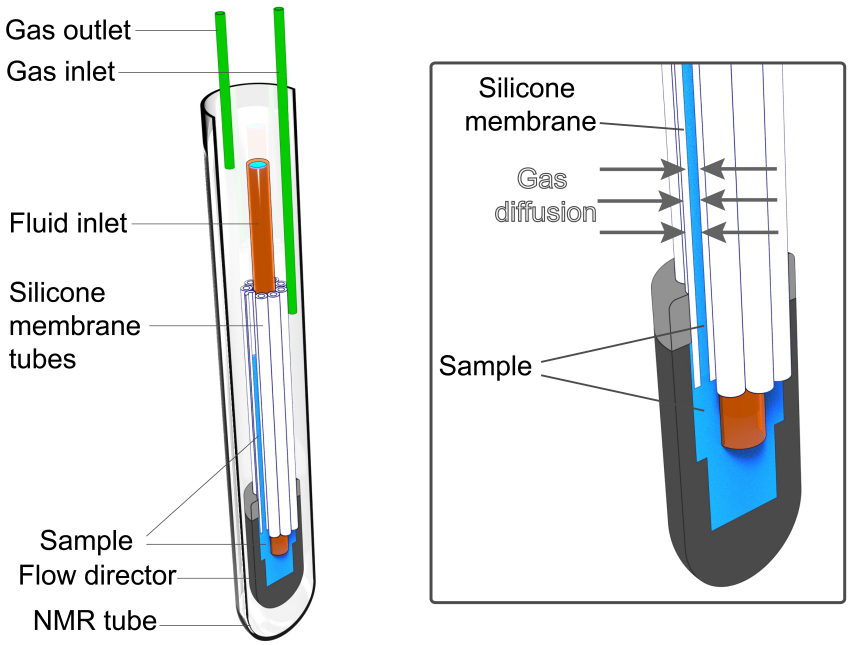

Figure 8.2: Membrane device,with cut-away, showing internal design of membrane fibers and the flow director. The sample (blue) is injected into the central polyimide fluid inlet tube (orange) and into the membranes via the flow director, which caps the bottom of the prototype. Xenon gas is introduced into and removed from the surrounding space through the gas inlet and outlet capillaries (green).

^{129}Xe spectra acquired using this system confirm the dissolution of xenon inside isotropic and ordered nematic solutions. The organic LC in this study was MBBA, which is uniaxial and thermotropic.[128,129] Weakly aligning, uniaxial pf1 bacteriophage was studied as an example of an aqueous LC medium.[130,131] Variable temperature studies of MBBA, and variable concentration studies of pf1 phage solutions were done with ^{2}H and ^{129}Xe NMR to confirm ordering and to demonstrate the utility of our approach for introducing hp-Xe into

previously inaccessible systems.

We used both aqueous and organic liquid crystals to serve as examples of viscous and aligned media, demonstrating the broad applicability of the device. Pf1 bacteriophage and MBBA were used as model samples because neither can be probed by hp-^{129}Xe using bubbling or 'shake-and-bake' experiments (which consist of pressurizing then physically agitating the sample to encourage mixing of the gas and solution). Both MBBA and pf1 are too viscous for bubbling to effectively dissolve xenon in a 5 mm tube. Shake-and-bake experiments fail because of poor mixing, and long times required to reestablish macroscopic order after mixing. Pf1 further serves as a model for relatively fragile biological samples, since shear forces caused by shaking or bubbling can damage it.[131] Since pf1's ability to form ordered phases relies on its structure being intact, the observation of unperturbed molecular ordering by pf1 indicates that this setup should be useful to study other delicate samples, such as living cells.

Molecular ordering was monitored by ^{2}H NMR. Deuterium, a spin-1 nucleus, has a quadrupole moment and thus yields a distinct peak splitting in aligned media. See Chapter 9 for a deeper examination of quadrupolar nuclei as reporters of molecular ordering. Observation of ^{2}H splittings confirmed that alignment was maintained in both MBBA and pf1 while xenon was being introduced.

A ^{129}Xe NMR peak corresponding to xenon inside the walls of the silicone membranes consistently appeared around 195 ppm (Fig.8.3, 8.4). The xenon-in-silicone peak moved an average 0.28 ppm/°C upfield for aqueous samples and 0.23 ppm/°C upfield for organic samples. This linear, upfield trend has also been observed for xenon adsorbed in polydimethylsiloxane (PDMS).[132] Dissolution of hyperpolarized xenon in aqueous and organic liquids of both low and high viscosity inside the membranes occurred in less than a minute, as monitored by the time evolution of the dissolved xenon peaks in arrayed single-shot spectra.

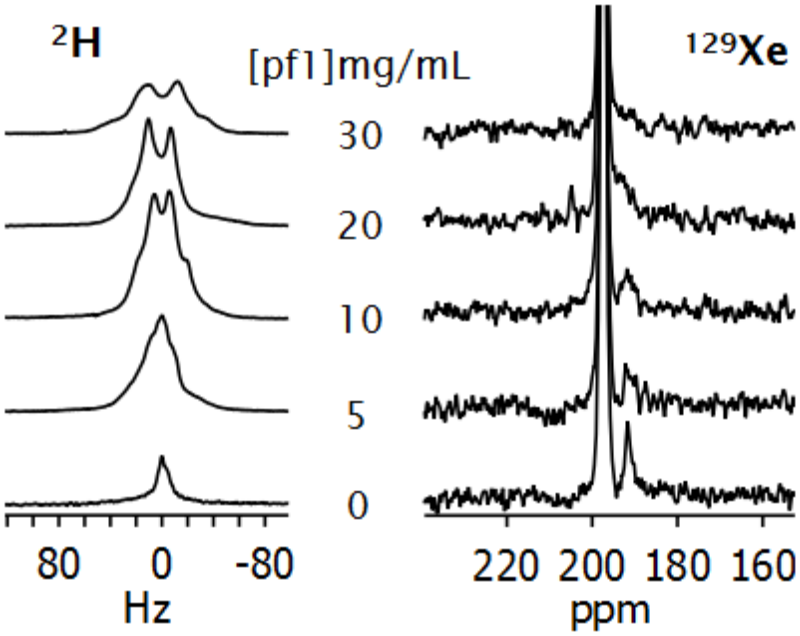

Figure 8.3: ^{2}H and ^{129}Xe spectra of 10% D_2O in 0-30 mg/mL pf1 phage. ^{2}H quadrupolar splitting indicates increasing ordering of D_2O molecules as phage concentration increases. The dissolved ^{129}Xe peak at ≈191 ppm broadens and coalesces with the silicone peak as phage concentrations increase.

The aqueous dissolved xenon peak was near 191 ppm (Fig.7.4), consistent with the value from bubbling xenon directly into solution. Viscous aqueous samples of pf1 bacteriophage provided weaker signals than the MBBA due in part to the lower solubility of xenon in water.[16] Nevertheless, the increase in ^{2}H quadrupolar splittings from D_2O, reflecting increased order of the D_2O[23] with increasing concentrations of phage, (Fig.7.4, left) demonstrate that the ordering remains unperturbed inside the membranes. Recent theoretical work supports that the order we observe inside the membranes is due to external field-induced alignment and not wall interactions.[133] Drawing from a study that applied thermally polarized xenon to an aqueous, lyotropic LC, we believe the significant broadening of the ^{2}H resonances with increasing phage concentration may reflect a collapse of the liquid crystal phase.[117,131]

MBBA has a well-characterized nematic-to-isotropic phase transition,[128,129] with the temperature at which this phase transition occurs heavily dependent on the identity and amount of solute dissolved in the MBBA.[134] The ^{2}H spectra (Fig.8.4, top) show quadrupolar splittings of benzene-d6 at low temperatures but disappear between 35°C and 40°C, demonstrating a loss of order.

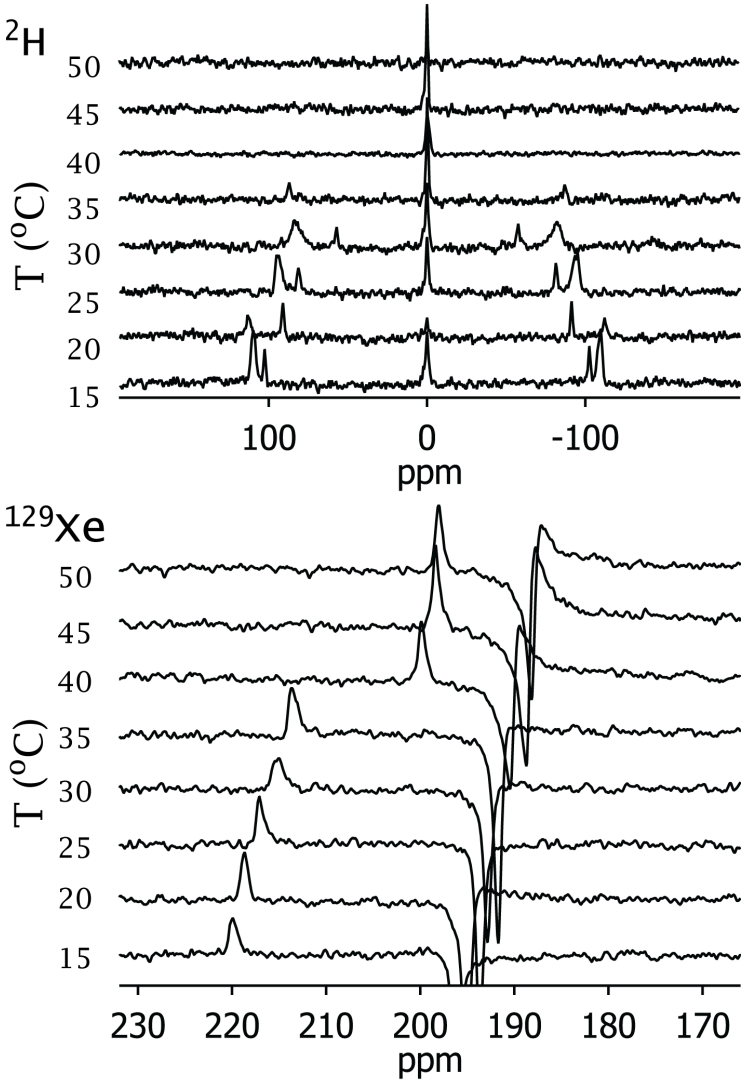

Figure 8.4: ^{2}H (top) and ^{129}Xe (bottom) spectra of 3% benzene-d6 in MBBA samples inside the membrane assembly over a range of temperatures. The dissolved Xe peak appears at 200-220 ppm. The xenon-in-silicone peak at 190-196 ppm is not phase corrected for better resolution between it and the dissolved xenon peak and is likely negatively phased due to residual suppressed signal. ^{2}H quadrupolar splitting indicates a transition from an anisotropic to an isotropic phase between 35-40° C, in good agreement with the jump in ^{129}Xe chemical shift of ≈13 ppm for the same temperature range.

This interval is consistent with previous work on similar samples.[134]

^{129}Xe is spin-1/2 and, therefore, does not have a quadrupole moment, but the chemical shift is sensitive to phase transitions in ordered media. A linear variation in the xenon-in-MBBA chemical shift occurs due to the increasing temperature, with an abrupt 12.4 ppm jump in the 35°C–40°C interval (Fig.8.4, bottom). This marked increase in shielding indicates a positive anisotropy of diamagnetic susceptibility, a known quality of MBBA,[135] and a common

characteristic of liquid crystals whose director axes are parallel to the external field.[32]

Both MBBA and pf1 bacteriophage are highly viscous samples into which xenon gas cannot be introduced by bubbling or shaking methods, previously precluding hyperpolarized gas experiments. With our device, it is now possible to obtain high quality hyperpolarized xenon spectra of these viscous solutions, or others prone to damage by agitation, in a moderate time without the requirement of isotopically enriched xenon sources, liquid flow, or shaking.

The logical next step in this work was to try to use ^{129}Xe to detect small analytes (Cryptophane-A (CryA) and cucurbit[6]uril (CB6)) in viscous solutions. We first attempted direct detection of 2 mM CryA in MBBA solution. CryA is inherently hydrophobic and dissolves readily in MBBA, but no Xe@CryA signal appeared. CB6 has modest solubility in both organics and aqueous solvents, so indirect detection (hyperCEST, see Chapter 3.4.3, 'hyperCEST' for an explanation of this experiment) was attempted to see if 0.1-1 mM CB6 and CB7 inside the membranes could be detected. A weakly selective excitation pulse centered between and capturing both the Xe@water and Xe@PDMS resonances was used. Still, low SNR led to messy and uninterpretable z-spectra. This experiment was repeated for 2 mM CryA in isotropic (low viscosity) MBBA with the same result.

This should perhaps come as no surprise, given the very small magnitude of the Xe@solvent peaks in this device compared to that of most bubbling samples. If a typical CEST responses attributed to xenon in a cage corresponds to a 50% reduction in the Xe@solvent signal, then in these devices, any small fluctuation in SNR due to flow obstruction, temperature changes, or even pressure could erroneously register as a response because of the low starting Xe@solvent SNR. Therefore, to enable small analyte detection using this device, SNR .

Both the Xe@membrane and the Xe@LC signals evolved within a few seconds to a minute of flowing hyperpolarized gas into the phantom, respectively, but many transients were required to capture the sample-dissolved ^{129}Xe signal with acceptable (> 10) SNR. We thus endeavored to better characterize gas transport through the membranes in order to determine the contributions of both physical transport and chemical relaxation to SNR limitations.

First, we explored the possibility that the setup was not effectively transporting xenon to the membranes due to a mechanical flow issue. Comparison of the membrane setup with the 'normal' bubbling setup indicated <50% of the expected Xe gas was reaching the PDMS. Gas was previously delivered to the *phantom* containing the device using the same polyimide tubing used in the membrane device itself. After replacing the 0.1 mm ID polyimide tubes that delivered gas to the phantom with 1/16" ($\approx$ 1.6 mm) PEEK tubing, Xe@PDMS signal was 275% improved for the membrane setup and equal to that of the bubbling setup (Fig 8.5). However, attempted hyperCEST experiments were still chaotic and uninterpretable. Therefore, although gas flow needed improvement, it was not the primary culprit of poor Xe@solvent signal.

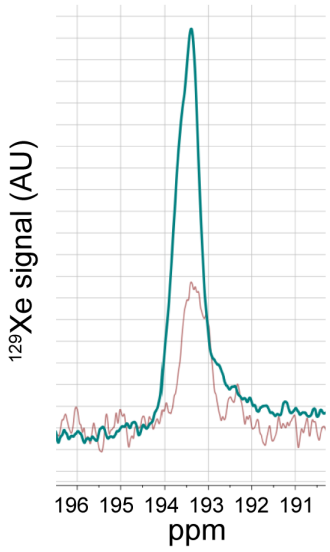

Figure 8.5: Single-shot Xe@PDMS signal before (red) and after (green) replacing gas delivery tubes with PEEK tubing.

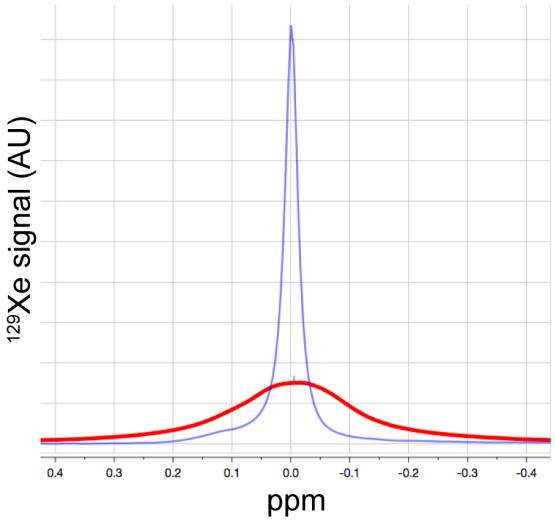

Figure 8.6: Single-shot Xe(g) signal before (blue) and after (red) addition of PDMS membranes.

Moving stepwise, we then characterized the dissolution of xenon into the PDMS membranes themselves. We compared the gaseous xenon resonance with and without PDMS membranes present, and found a) that the Xe(g) peak area is the same for both samples, b) that SNR lowers in the presence of membrane and c) linewidth increases (Fig 8.6, Table 8.1). The equal peak areas imply that xenon is being effectively delivered to the sample volume and unimpeded by the device structure. Lowered SNR follows an expectedly high affinity of Xe for PDMS, and the increased linewidth suggests that exchange is in the slow-to-intermediate exchange regime.

Table 8.1: ^{129}Xe NMR of Xe(g) with and without PDMs membranes present

System	Area (AU)	SNR (AU)	Linewidth (Hz)
Xe(g)	10.4	2540	10
Xe(g) + PDMS	10.8	374	26

In all, these results indicated effective delivery and dissolution of xenon into the membrane material. To determine the partition of gas in the membranes, the Xe(g) and Xe@PDMS peak areas were compared, lending a ratio of Xe@PDMS:Xe(g) = 12.05:0.25. At 60 psi of 2% natural abundance Xe and an optimistic 5% polarization, this leads to a Xe@PDMS concentration of ≈1.2 µM. This concentration is low (where ≈ 5-15 µM is expected for a

similarly composed sample of water), but can be compensated for by way of multiple-bubble acquisition, wherein multiple transients are acquired and averaged after a single period of bubbling xenon into the sample tube.

Given this starting concentration, we began to estimate diffusion times of xenon through the membranes using CO_2 as an analogue, as it is 95% the volume of Xe with like polarity and a self-diffusion constant of $11x10^6 cm^2 s^{-1}$ in PDMS. In theory, a xenon atom crossing an area of 55x55 µm (the thickness of the membrane) should take ≈ 3 ps to do so, with a permeation time (which include absorption, diffusion, and desorption) or ≈ 60 ps.[1] If these simple calculations are on par, and if one assumes that T_1, $T_2 > t_{permeation}$, then the lack of Xe@cage signal may not be due to slow transport through the membrane.

Table 8.2: Exchange dynamics of the Xenon-PDMS system weighted by spin pool populations

System	**Exchange rate k (s^{-1})**	**Lifetime τ (s)**
Total system	22	0.045
Gas → PDMS	6.2	0.160
PDMS → Gas	15.7	0.063

To get a more practical measure of transport, kinetic information was extracted from NMR data and shown in Table 8.2, given the relations

$$\Delta\nu = (1/\pi T_2 + 1/\pi\tau_{ex})$$
and
$$\tau_{ex} = (\tau_{gp}\tau_{pg})/(\tau_{gp} + \tau_{pg})$$

where τ_{pg} and τ_{gp} are the timescales associated with xenon moving from PDMS to gas and vice versa, respectively. In this highly asymmetric system, $k_{ex} \approx k_{pg}$. The theoretical permeation time of 10^{-12} s does not account for the long apparent lifetime of the Xe@PDMS sate (60 ms).

Clearly, the mean free path of Xe is not directly through the membrane. This result is upheld by RIS model simulations of N_2 in PDMS, which show 'jump diffusion' of the gas through the polymer. PDMS is not porous, but rather has many branched chains through which gas atoms may "jump" upon adequate flexing of the polymer chains. For N_2 atoms, this results in mean-squared displacements of ≈ 0.1 µm every 200 ps. Roughly applying this trend to our 55 µm-thick membrane, we get a diffusion time of about 0.1 ms, which would likely be even longer due to xenon atoms being 15% larger than the N_2 molecule, putting this process at a timescale that becomes relevant for relaxation mechanisms.

[1]For CO_2 in PermSelect membranes, P = 3250 barrer*, assume pressure differential of 0.08 atm across the membrane. 1 barrer = 10^{-10} cm^3 (STP)·cm/cm^2·s· cmHg; assume 1x1 mm membrane area.

Table 8.3: Relaxation measurements of ^{129}Xe in PDMS membranes

T_1 (s)	Xe(g)	Xe(g)+PDMS	Xe(g)+PDMS + water
For M_0-$M_z = e^{-t/T_1}$	48	24	22
For 3-component exponential fit	62	20	21

Accepting that diffusion is likely slowing xenon transport from the membranes to the sample, we then took relaxation measurements to determine if we could potentially compensate for slow transport by minimizing relaxation effects (Table 8.3. These measurements resulted in $T_{1(Xe@PDMS)}$, $T_2^*{}_{(Xe@PDMS)}$, and $T_{2(Xe@PDMS)}$ of 8.7 s, 3.5 ms, and 30 ms, respectively. These values show that relaxation is, as usual, dominated by T_2 and T_2*, whose corresponding rates are a factor of 2 faster than the measured exchange rate of xenon through PDMS. Even T_2 is much shorter than the exchange rate, precluding the possibility of preserving magnetization until the sample is reached by pulse sequence manipulation (e.g. through 180^o pulse trains).

However, since $T_2 > \tau_{Xe@PDMS}$, application of spin echoes did aid in recovery of the Xe@PDMS signal (Fig.8.7), demonstrating the likely contribution of interfacial susceptibility differences to relaxation. However, this finding is optimistic for experiments in which the Xe@PDMS peak may be used as a large spin pool for future hyperCEST experiments.

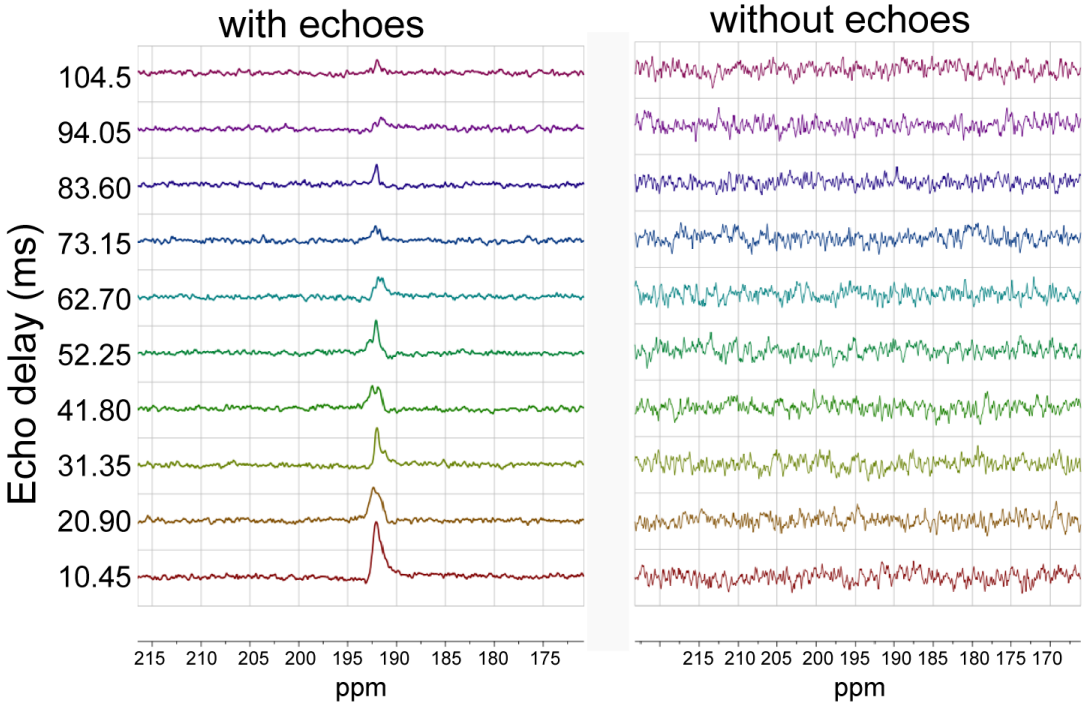

Figure 8.7: ^{129}Xe spectra showing the appreciable recovery effect of spin echoes on the Xe@PDMS peak.

8.4 Conclusion

We have developed the first robust method for dissolving hp-^{129}Xe directly into viscous liquids without bubbling, enabling completely new types of hyperpolarized gas studies. Proof-of-concept experiments demonstrated the quantitative abilities of this method in both aqueous and organic solutions, specifically in the detection of the nematic-isotropic phase transition of a thermotropic liquid crystal. These results mark the potential for new studies of hp-^{129}Xe in viscous and other anisotropic media, including those with cells, protein solutions, liquid crystals and polymers. This system also allows direct introduction of other gases into the sample, including oxygen and carbon dioxide for cell suspensions.

Further characterization of the device showed that slow transport of xenon through membranes combined with short T_2 and T_2* relaxation times limit direct detection of analytes, but the application of refocusing pulses that preserve the Xe@PDMS signal may enable indirect detection methods through hyperCEST spectroscopy.

Chapter 9

Fusion, ho! Xenon molecular sensors in orienting media

This final chapter consolidates the various knowledge gained from the ventures of previous chapters in an attempt to use ^{129}Xe to detect self-ordering of xenon host cucurbit[6]uril (CB6) in a liquid crystal (LC) phase of pf1 bacteriophage. With technology that enables us to monitor hyperpolarized xenon in viscous media, we will be able to observe and take advantage of the chemical shift enhancement proffered by molecular ordering on xenon chemical shift for improved molecular detection.

9.1 Background

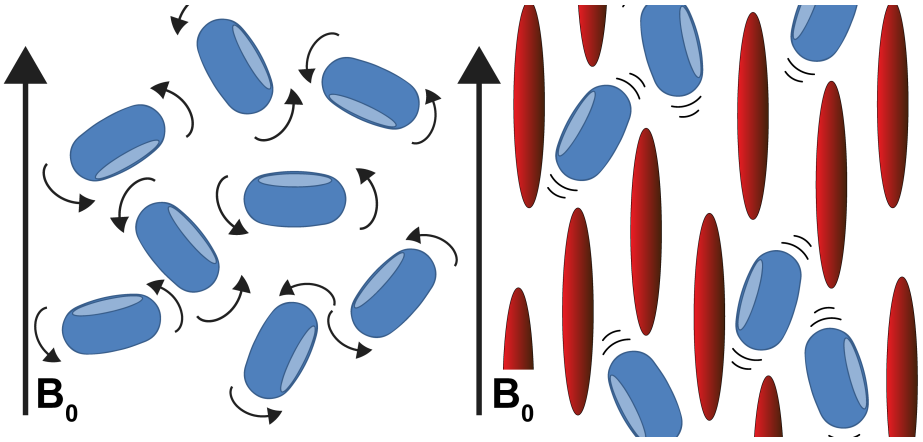

Figure 9.1: In an isotropic environment (left), CB6 molecules tumble freely and visit every possible orientation with respect to an external magnetic field. In an anisotropic environment (right) populated with molecules that form a liquid crystal phase (red ellipses), CB6 molecules can become restricted in their motion such that they can adopt only certain orientations with respect to the external field.

Indeed, Hp-^{129}Xe has proven effective for detection and analysis of a growing number of biological samples and processes. In a number of these studies, the mode of detection has relied on modest changes in ^{129}Xe chemical shift upon binding of targeted cryptophane conjugates to biological targets.[20,115] Increasing the chemical shift difference between bound and unbound sensor resonances will allow better contrast, and faster, more sensitive biosensing. One way to enhance the shift change associated with xenon binding events is the dissolution of biosensors in liquid crystals (LCs). The orienting environments of LCs cause an increase in anisotropy of the rotational diffusion of molecules and can restore orientation-dependent interactions in the NMR Hamiltonian that typically get averaged out in isotropic solutions. LCs have been used to augment shielding from chemical shift anisotropy, dipolar and quadrupolar coupling in a variety of chemical systems with both strongly and weakly orienting LCs.[136–138]

To illustrate, imagine a relatively rigid but geometrically asymmetric molecule, such as the now familiar torus-shaped cucurbit[6]uril (CB6), in an isotropic solution (Fig.9.1). With the application of an external magnetic field, nuclear spins preferentially align parallel to the magnetic field, but the CB6 molecules still tumble around freely in solution. To see how this tumbling affects the chemical shift of xenon inside of CB6, one turns to the Hamiltonian for a nuclear spin in a magnetic field.[23] With respect to the high field approximation, four major terms evolve: the Zeeman term corresponding to the interaction of the spin with the external magnetic field incorporating the effect of chemical shift, the indirect J-coupling, direct dipolar coupling, and lastly quadrupolar coupling, respectively shown:

$$
\begin{aligned}
H = \frac{-B_z}{2\pi} \sum_i \gamma_i (1 - \sigma^{iso} - \sigma^{aniso}) I_{i,z} \\
+ \sum_{i,j} J_{ij}^{iso} \vec{I}_i \cdot \vec{I}_j \\
+ \sum_{i,j} (2D_{ij}^{aniso} + J_{ij}^{aniso})[I_{i,z} I_{j,z} - \frac{1}{4}(I_{i+} I_{j-} + I_{i-} I_{j+}] \\
+ \sum_i \frac{eQ_i V_{i,zz}}{4I_i(I_i - 1)} [3I_{i,z}^2 - I_i(I_i + 1) + \frac{1}{2}\eta(I_+^2 + I_-^2)]
\end{aligned}
\tag{9.1}
$$

where B_z is the z-component of the effective external magnetic field, γ is the gyromagnetic ratio, σ^{iso} and σ^{aniso} are the isotropic and anisotropic components of the chemical shielding, respectively, and $\mathbf{I}$ is the nuclear spin operator for spins i and j. and $I_\pm = I_x \pm iI_y$ indicate raising and lowering operators. J, D, and Q are the scalar J-coupling, dipolar coupling, and quadrupolar constants, accordingly. $V_{i,zz} = eq$ is the relevant principal component of the

electric field gradient (EFG), and η_Q is the quadrupolar asymmetry parameter. Assuming solvent shielding contributions are negligible, which has been previously demonstrated to be reasonable in relevant solutions,[32,124] the J-coupling and dipolar coupling interaction terms disappear. Unless the spin has a quadrupole moment, only the effective Zeeman term remains.[1]:

$$H = \frac{-B_z}{2\pi} \sum_i \gamma_i (1 - \sigma^{iso} - \sigma^{aniso}) I_{i,z} \tag{9.2}$$

and the experimental shielding becomes:

$$< \sigma_{zz} >= \sigma^{iso} + \sigma^{aniso} \tag{9.3}$$

Chemical shift is directly proportional to chemical shielding, so it is easy to see the potential for chemical shift enhancement when anisotropic chemical shielding is present. However, the anisotropic shielding component is orientation-dependent:

$$\sigma^{aniso} = \frac{2}{3} \Delta\sigma P_2(cos(\alpha)) \tag{9.4}$$

where $\Delta\sigma = \sigma_{\parallel} - \sigma_{\perp}$ and $P_2\cos(\alpha)$ is the second-order Legendre polynomial with α being the angle between the liquid crystal director axis and the external magnetic field:

$$P_2(cos(\alpha)) = \frac{1}{2}(3cos^2(\alpha) - 1) \tag{9.5}$$

Therefore, in the isotropic aqueous case mentioned above, since molecules are able to visit every molecular orientation with respect to the external field, the anisotropic term averages out to zero. There is no anisotropy for xenon atoms to feel, encapsulated or not, and one is left with the isotropic Zeeman term, and thus the isotropic chemical shift.

If anisotropy is added to the system, things get more complicated (and interesting). One way to impose orientational molecular ordering is to use uniaxial liquid crystals whose director axis is parallel with the external magnetic field.[31] Because of the $P_2\cos(\alpha)$ term, liquid crystals whose director axes run along the external magnetic field contribute most strongly to the experimental shielding.

Because of the oblong shape of the CB6 molecules, their motion may become constrained in this liquid crystal environment, either electrostatically or geometrically (Fig.9.1). One can think of this as navigating a field (the isotropic case) versus a thick grove of trees (the anisotropic case): in the field, one can navigate by walking upright, rolling on the ground, tumbling, what have you. In the grove, however, one may be able to slip between trunks

[1] Although this description is applicable to any nucleus, the same result arises for ^{129}Xe: ^{129}Xe itself does not typically contribute meaningful scalar or dipolar coupling, nor does it possess a quadrupole moment.

and branches while walking upright, but she will certainly not get very far by rolling on the ground. Such is the constraining effect of liquid crystal phases on the motion of molecules. If the majority of CB6 molecules in the solution are constrained in the same orientations, they themselves create an anisotropic environment that a xenon atom feels and responds to through asymmetric distortions in its electron cloud when encapsulated in the host molecules.

One quantifies the effect of this constraint by re-exploring the above spin Hamiltonian. Although some anisotropic scalar coupling exists, its contribution will be negligible. The dipolar coupling term is also orientation dependent, and there is some evidence suggesting that dipolar coupling between xenon and xenon host molecules may be recovered in liquid crystalline solutions.[38] However, chemical exchange adversely affects the strength and visibility of dipolar splitting in the ^{129}Xe spectra. Again, no quadrupole interaction is observed. Thus, the Zeeman term dominates as before, but the anisotropic shielding term does not average out, as xenon atoms will 'feel' the ordering of both the constrained CB6 molecules and the surrounding liquid crystal milieu. Thus, a host molecule whose motion is constrained by placement in an ordered environment will contribute an additional value of shift to the xenon atom whose magnitude depends on the degree of ordering.[31,32] The quantitative measure of solute ordering is called the order parameter S ($0 \leq S \leq 1$). The order parameter depends on a variety of experimental conditions, from the identities of the liquid crystal and oriented solute to the temperature of the system.

The following work sought to determine whether CB6 molecules, given their small size, could actually be ordered in an aqueous liquid crystal environment before attempting to observe hp-^{129}Xe inside of ordered cages. Although similar work explored the orientability of cryptophane derivatives in organic LC ZLI 1132, the advantage of the following system is commercial availability of CB6 and biological compatibility.[139]

9.2 Methods

9.2.1 Sample preparation

CB6 (Sigma-Aldrich) and guest molecule cyclopentylmethane amine (CPMA) (Sigma Aldrich) were used as received. The addition of salt was required for sufficient dissolution of CB6 for ^{1}H- and ^{14}N-NMR experiments. Various salt types and concentrations were explored, and Na_2SO_4 allowed the highest concentration of CB6 to be dissolved (up to 20 mM) without apparent inhibition of xenon exchange nor effecting the ordering ability of pf1 bacteriophage, as judged by ^{2}H-NMR.

CB6 and CB6*CPMA solutions were carefully introduced to the pf1 solution, and the total sample, which was very viscous, was carefully pipeted into 5 mm phantoms prior to experiments in order to avoid shearing of the phage during transfer.

9.2.2 NMR experiments

^{1}H- and ^{2}H-NMR experiments were performed on a 400 MHz Varian NMRS console, while ^{14}N- experiments were performed using a 700 MHz Bruker Biospin console. 256-1024 transients were collected for each spectrum with 8 Hz exponential line broadening applied.

9.3 Results

Pf1 bacteriophage was chosen as the ordering medium for these investigations despite being only weakly nematic, as it is aqueous and thus compatible with biological samples.[130] Additionally, pf1 is lyotropic, and unlike a thermotropic LC would not require temperature changes that would also influence xenon chemical shift. Additionally, as per the previous study in Chapter 8, the concentrations of pf1 phage that led to order observable by ^{129}Xe NMR were already determined.

However, the concentrations of pf1 at which CB6 would be oriented (if possible) had not yet been discovered. Because the membrane device described in Chapter 8 was not yet optimized for detection of xenon in cages, another approach for determining whether CB6 molecules could be ordered in liquid crystals was required. In the previous study, order was confirmed not only by ^{129}Xe but also ^{2}H by way of deuterium's quadrupole moment. Much like the anisotropic shielding, the scalar, dipolar and quadrupolar coupling terms in Eqn. 9.1 are orientation dependent, leading to additional splittings of the D_2O magnetic resonance when molecular ordering is present. However, ^{2}H chemical shift, scalar and dipolar interactions are incredibly weak (<5 kHz at 11.7 T) leaving the quadrupolar coupling term, reprinted in Eqn 9.6, to dominate.[140]

$$+\sum_i \frac{eQ_iV_{i,zz}}{4I_i(I_i-1)}[3I_{i,z}^2 - I_i(I_i+1) + \frac{1}{2}\eta(I_+^2 + I_-^2)] \tag{9.6}$$

The scalar quadrupolar moment (Q) for the deuteron ($\approx 2.9x10^{-27}cm^2$), yielding quadrupolar couplings in the range of hundreds of kHz.

Although seemingly large, the quadrupolar interaction is usually much smaller than the Zeeman term, and so can be treated as a first order perturbaton to the Zeeman levels. this perturbation results in an additional splitting of the Zeeman levels, such that $\Delta E = h(\nu_0 \pm \nu_Q)$. In the case of axial symmetry imposed by the uniaxial liquid crystals explored in these studies, the splitting reduces to

$$\Delta\nu_Q = \frac{3e^2qQ}{4h}(3cos^2\theta - 1) \tag{9.7}$$

where the previously mentioned substitution $V_{i,zz} = eq$ has been made. θ corresponds to the angle between the ^{2}H-X bond and the z axis. Thus, the existence net direction of orientational molecular ordering can be extrapolated from quadrupolar splitting. As seen in

Chapter 8, variable temperature studies can further reveal the degree of solute ordering and phase transition information.

While ^{2}H splittings of D_2O are useful for determining whether solvent molecules are ordering, they cannot directly imply ordering of CB6. Acquisition of a ^{2}H-labeled CB6 was out of the question, so a more clever approach was needed. ^{14}N also has a quadrupole moment and can be used to monitor ordering of solutes in LCs.[141] but relaxation mechanisms of quadrupolar nuclei are so strong that ^{14}N-NMR peaks of complex macromolecules like CB6 are broadened to death.

Recalling that CB6 acts as a good host for a number of small nitrogen-containing molecules, we posited that we could indirectly detect alignment of CB6 by pf1 through ^{14}N-NMR of strongly binding ($K_a \approx 3.3x10^5\ M^{-1}$) guest cyclopentylmethane amine (CPMA, Fig.9.2). A number of studies, including work previously done in this laboratory, have also sought the enhancement of host-guest interactions by aligning inclusion complexes with LCs.[38,142,143]

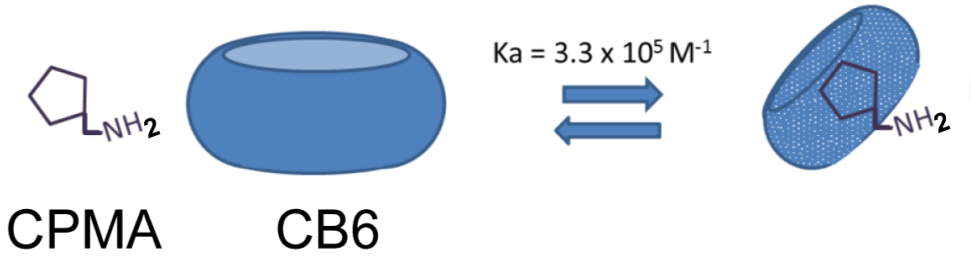

Figure 9.2: CPMA is a strongly-binding guest molecule for CB6 whose structural simplicity and relatively symmetric nitrogen moiety make it an appealing ^{14}N-NMR reporter for the degree of ordering of CB6 molecules.

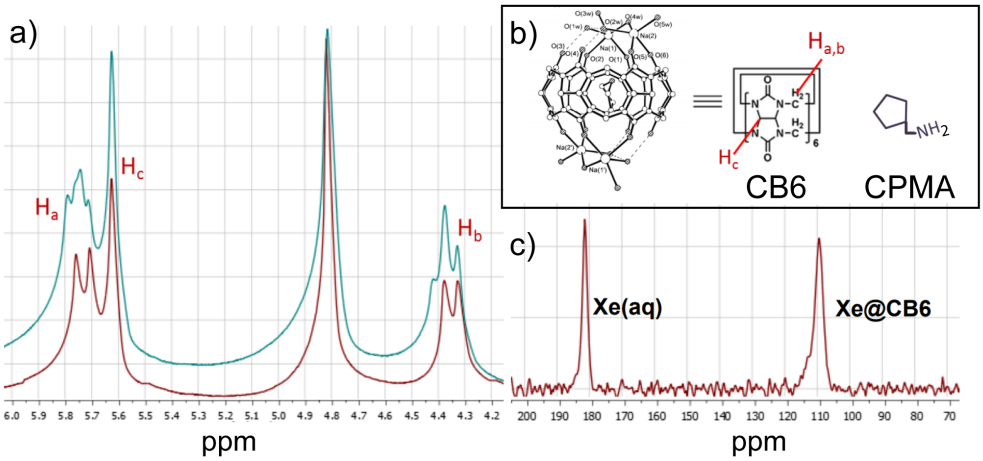

Figure 9.3: a)^{1}H spectra of 20 mM CB6 with (blue) and without (red) 20 mM CPMA in 1XPBS. Association of CPMA breaks symmetry of the methylene bridge protons, leading to the observed splitting at 4.35 and 5.75 ppm. b) Structures of CB6 and CPMA. c) A ^{129}Xe spectrum of 2 mM CB6 in 0.2M Na_2SO_4 and 1XPBS shows the unique resonance associated with xenon residing in CB6 is not hindered by the presence of sodium ions.

Since ^{14}N is a quadrupolar nucleus and CPMA a nitrogen-containing small molecule, ordering of CPMA could be determined by observation of quadrupolar splitting at the CPMA resonance. ^{1}H NMR spectra confirmed complexation of CPMA and CB6 (Fig.9.3a). ^{2}H studies confirmed that the amount of 0.2 M Na_2SO_4 required to solubilize CB6 did not appreciably diminish ordering of D_2O molecules in 35 mg/mL pf1 medium.^{14}N-NMR of CPMA in isotropic solutions showed that neither free nor CB6-complexed CPMA was ordered in the absence of pf1 phage (Fig.9.4).

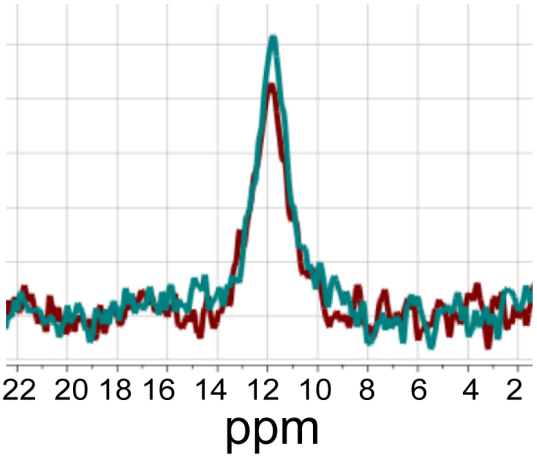

Figure 9.4: ^{14}N-NMR spectra of 10-20 mM free (blue) and CB6-bound (Red) CPMA in isotropic solution (0.2 M Na_2SO_4). Though it contains nitrogen atoms, CB6 is too complex to yield its own ^{14}N peak due to strong quadrupolar relaxation effects. The observed peak actually corresponds to the nitrogen atom in CPMA. This data indicates that in the absence of orienting media, CPMA experiences no apparent anisotropic quadrupolar interactions.

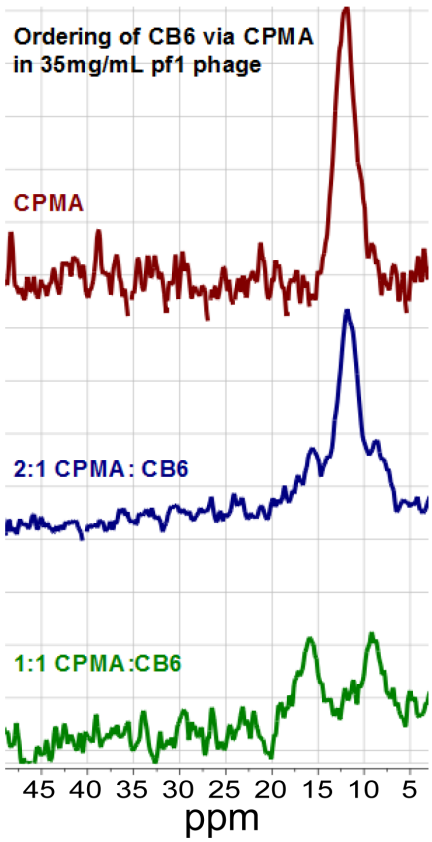

Figure 9.5: ^{14}N-NMR spectra of 10-20 mM free and CB6-bound CPMA in an anisotropic pf1 (0.2 M Na_2SO_4) solution. Evolution of a quadrupolar splitting of the CPMA resonance centered at $\approx$ 12 ppm upon addition of CB6 indicates that CB6 self-orders in the pf1 liquid crystal phase and takes its CPMA guest along with it.

Addition of oriented-phase pf1 phage also led to no observable splitting for free CPMA. However, for CB6-bound CPMA in oriented pf1, quadrupolar splitting of $\approx$ 350 Hz was observed (Fig.9.5). The whole of these data imply that CB6 is ordered by pf1, and bound CPMA along with it. The degree to which CB6 is ordered can be estimated by proxy through the order parameter of the C-^{14}N bond in CPMA, which takes the same P_2 Legendre polynomial form as the chemical anisotropic shielding term:

$$S =< P_2 cos(\Phi) >= \frac{1}{2}(3cos^2(\Phi) - 1) \tag{9.8}$$

In this case, Φ is the angle between the long axis of a molecule and the director axis of the liquid crystal. Order parameters are typically obtained by variable temperature experiments

for thermotropic LCs, but lyotropic LCs are not so trivial. Rather, lyotropic LC order parameters are a function of both temperature and density.[144] While these data show some net orientation of CB6 in pf1, more experiments at a range of temperatures and concentrations of phage are required to determine the phase behavior of CPMA and CB6 in pf1. To clarify, the degree of order of CPMA or CB6 does not trivially translate to the ordering felt by the xenon atom. Even though xenon is also a CB6 guest, it exchanges much more quickly than does CPMA, making it difficult to predict the degree to which CB6 ordering will influence xenon's anisotropic chemical shift component. Nonetheless, these results are encouraging for the anisotropic shift enhancement hypothesis and provide motivation for continued work.

9.4 Conclusion

This work demonstrated the ability of CB6 to self-orient in an aqueous orienting environment. Knowing now that CB6 can become ordered in a dilute pf1 bacteriophage LC phase, the logical next step is to examine the xenon-CB6 system with ^{129}Xe NMR in isotropic and anisotropic solutions to determine the degree to which xenon is sensitive to CB6 ordering via anisotropic chemical shielding. In addition, further experiments gauging the tunability of CB6 ordering as well as functionalizing CB6 with different rigid and flexible groups to observe their effects on CB6 ordering and xenon chemical shift are of interest.

Chapter 10

Conclusion

As has been thoroughly established in this dissertation, the pursuit of sensitive and selective xenon biosensors has inspired constructs as diverse as the phenomena they seek to detect. In this work alone, three uniquely constructed molecular sensors demonstrated their abilities to both encapsulate xenon on timescales amenable to NMR and MRI techniques and accomplish targeted molecular detection. Further, this dissertation work accomplished observation of the orientability of curcurbit[6]uril in an aqueous liquid crystal, demonstrating the potential to use these cages for studies of the effects of orientation on binding event detection and contrast. Continuing work includes examination of these and other xenon hosts in isotropic and anisotropic media to quantify any anisotropic ^{129}Xe chemical shift enhancement that might come from host-target binding events.

In addition, this work resulted in the first device and setup enabling long-term experiments involving dissolution of hyperpolarized ^{129}Xe into viscous and orienting media. It was shown that xenon can dissolve in isotropic and anisotropic media and and detect molecular order within the device. Future efforts will continue to target detection of molecular cages inside the device to explore effects of orientation on binding event detection as well as to further the potential of using hyperpolarized ^{129}Xe to probe unprocessed viscous samples, such as whole blood and saliva.

The sum of these contributions is another strong push toward clinical application of hyperpolarized Xe MRI. Coupled with the evolution of clever reconstruction methods that allow the acquisition of images within the limit of relaxation of hyperpolarized atoms, this technique continues to evolve into a powerful diagnostic imaging modality.

Bibliography

(1) Pysz, M.; Gambhir, S.; Willmann, J. *ClinRadiol* **2010**, *65*, 500–516.

(2) Walker, T. G.; Happer, W. *Reviews of Modern Physics* **1997**, *69*, 629–642.

(3) Nikolaou, P.; Goodson, B. M.; Chekmenev, E. Y. *Chemistry - A European Journal* **2015**, *21*, 3134.

(4) Barskiy, D. A. et al. *Chemistry - A European Journal* **2016**, *23*, 725–751.

(5) Hirsch, M. L.; Kalechofsky, N.; Belzer, A.; Rosay, M.; Kempf, J. G. *Journal of the American Chemical Society* **2015**, *137*, 8428–8434.

(6) Ardenkjaer-Larsen, J. H. *Journal of Magnetic Resonance* **2016**, *264*, 3–12.

(7) Ward, H. R. *Accounts of Chemical Research* **1972**, *5*, 18–24.

(8) Kovtunov, K. V.; Zhivonitko, V. V.; Skovpin, I. V.; Barskiy, D. A.; Koptyug, I. V. Parahydrogen-Induced Polarization in Heterogeneous Catalytic Processes., 2012.

(9) Green, R. A.; Adams, R. W.; Duckett, S. B.; Mewis, R. E.; Williamson, D. C.; Green, G. G. R. *Progress in Nuclear Magnetic Resonance Spectroscopy* **2012**, *67*, 1–48.

(10) Natterer, J.; Bargon, J. *Progress in Nuclear Magnetic Resonance Spectroscopy* **1997**, *31*, 293–315.

(11) Adams, R. W.; Aguilar, J. A.; Atkinson, K. D.; Cowley, M. J.; Elliott, P. I. P.; Duckett, S. B.; Green, G. G. R.; Khazal, I. G.; Lopez-Serrano, J.; Williamson, D. C. *Science* **2009**, *323*, 1708–1711.

(12) Hövener, J.-B.; Schwaderlapp, N.; Lickert, T.; Duckett, S. B.; Mewis, R. E.; Highton, L. A. R.; Kenny, S. M.; Green, G. G. R.; Leibfritz, D.; Korvink, J. G.; Hennig, J.; von Elverfeldt, D. *Nature Communications* **2013**, *4*, DOI: 10.1038/ncomms3946.

(13) Mcmahan, Z. H.; Wigley, F. M., *HHS Public Access*; 3, 2015; Vol. 5, pp 355–370.

(14) Witte, C.; Schröder, L. *NMR in Biomedicine* **2012**, *26*, 788–802.

(15) Oros, A. M.; Shah, N. J. *Physics in Medicine and Biology* **2004**, *49*, DOI: 10.1088/0031-9155/49/20/R01.

(16) Cherubini, A.; Bifone, A. *Progress in Nuclear Magnetic Resonance Spectroscopy* **2003**, *42*, 1–30.

(17) Schröder, L. *Physica Medica* **2013**, *29*, 3–16.

(18) Mazzanti, M. L.; Walvick, R. P.; Zhou, X.; Sun, Y.; Shah, N.; Mansour, J.; Gereige, J.; Albert, M. S. *PLoS ONE* **2011**, *6*, e21607.

(19) Wang, Y.; Dmochowski, I. J. *Accounts of Chemical Research* **2016**, *49*, 2179–2187.

(20) Mari, E.; Berthault, P. *Analyst* **2017**, *142*, 3298–3308.

(21) Schröder, L. *Hyperpolarized and Inert Gas MRI: From Technology to Application in Research and Medicine* **2016**, 263–277.

(22) Jennings, W. B. *Analytica Chimica Acta* **1982**, *144*, 297.

(23) Levitt, M. H., *Spin dynamics: basics of nuclear magnetic resonance*; John Wiley & Sons: Chichester, UK, 2001, Ch. 6.

(24) Keeler, J. **2010**.

(25) Kowalewski, J. Nuclear Spin Relaxation in Liquids., 2017.

(26) Gore, J. C.; Anderson, A. W. In *eMagRes*; John Wiley & Sons, Ltd: 1996.

(27) Driehuys, B.; Pollaro, J.; Cofer, G. P. *Magnetic Resonance in Medicine* **2008**, *60*, 14–20.

(28) Driehuys, B.; Martinez-Jimenez, S.; Cleveland, Z. I.; Metz, G. M.; Beaver, D. M.; Nouls, J. C.; Kaushik, S. S.; Firszt, R.; Willis, C.; Kelly, K. T.; Wolber, J.; Kraft, M.; McAdams, H. P. *Radiology* **2012**, *262*, 279–289.

(29) Lynch, C. 3.; Baum, J.; Tenbrinck, R. *Anesthesiology* **2000**, *92*, 865–868.

(30) Jordan, B. D.; Wright, E. L. **2015**.

(31) Muenster, O.; Jokisaari, J.; Diehl, P. *Molecular Crystals and Liquid Crystals* **1991**, *206*, 179–186.

(32) Jokisaari, J. **2013**, *2*, 279–288.

(33) Sozzani, P.; Comotti, A.; Simonutti, R.; Meersmann, T.; Logan, J. W.; Pines, A. *Angewandte Chemie - International Edition* **2000**, *39*, 2695–2698.

(34) Springuel-Huet, M. A.; Bonardet, J. L.; Gedeon, A.; Fraissard, J. *Magnetic Resonance in Chemistry* **1999**, *37*, S1–S13.

(35) Baias, M.; Demco, D. E.; Istrate, D.; Popescu, C.; Blümich, B.; Möller, M. *The Journal of Physical Chemistry B* **2009**, *113*, 12136–12147.

(36) Duewel, M.; Vogel, N.; Weiss, C. K.; Landfester, K.; Spiess, H. W.; Münnemann, K. *Macromolecules* **2012**, *45*, 1839–1846.

(37) Moudrakovski, I. L.; Sanchez, A. A.; Ratcliffe, C. I.; Ripmeester, J. A. *Journal of Physical Chemistry B* **2001**, *105*, 12338–12347.

(38) Goodson, B. M. Nuclear magnetic resonance of laser-polarized noble gases in molecules, materials and organisms., Ph.D. Thesis, University of California, Berkeley, 1999.

(39) Patz, S.; Muradian, I.; Hrovat, M. I.; Ruset, I. C.; Topulos, G.; Covrig, S. D.; Frederick, E.; Hatabu, H.; Hersman, F. W.; Butler, J. P. *Academic Radiology* **2008**, *15*, 713–727.

(40) Roose, B. W.; Zemerov, S. D.; Dmochowski, I. J., *Xenon–Protein Interactions: Characterization by X-Ray Crystallography and Hyper-CEST NMR*, 1st ed.; Elsevier Inc.: 2018; Vol. 602, pp 249–272.

(41) Seltzer, S. **2008**.

(42) Zaiss, M.; Schnurr, M.; Bachert, P. *Journal of Chemical Physics* **2012**, *136*, DOI: 10.1063/1.3701178.

(43) Kunth, M.; Witte, C.; Hennig, A.; Schröder, L. *Chemical Science* **2015**, *6*, 6069–6075.

(44) Fairchild, R. M.; Joseph, A. I.; Holman, K. T.; Fogarty, H. A.; Brotin, T.; Dutasta, J. P.; Boutin, C.; Huber, G.; Berthault, P. *Journal of the American Chemical Society* **2010**, *132*, 15505–15507.

(45) Bartik, K.; Luhmer, M.; Heyes, S. J.; Ottinger, R.; Reisse, J. *Journal of Magnetic Resonance, Series B* **1995**, *109*, 164–168.

(46) Adiri, T.; Marciano, D.; Cohen, Y. *Chemical Communications* **2013**, *49*, 7082–7084.

(47) Schnurr, M.; Joseph, R.; Naugolny-Keisar, A.; Kaizerman-Kane, D.; Bogdanoff, N.; Schünke, P.; Cohen, Y.; Schröder, L. *ChemPhysChem* **2018**, 1–7.

(48) Fukutomi, J.; Adachi, Y.; Kaneko, A.; Kimura, A.; Fujiwara, H. *Journal of Inclusion Phenomena and Macrocyclic Chemistry* **2007**, *58*, 115–122.

(49) Hane, F. T.; Li, T.; Smylie, P.; Pellizzari, R. M.; Plata, J. A.; Deboef, B.; Albert, M. S. *Scientific Reports* **2017**, *7*, 4–10.

(50) Roukala, J.; Zhu, J.; Giri, C.; Rissanen, K.; Lantto, P.; Telkki, V. V. *Journal of the American Chemical Society* **2015**, *137*, 2464–2467.

(51) Jeong, K.; Netirojjanakul, C.; Munch, H. K.; Sun, J.; Finbloom, J. A.; Wemmer, D. E.; Pines, A.; Francis, M. B. *Bioconjugate Chemistry* **2016**, *27*, 1796–1801.

(52) Stevens, T. K.; Ramirez, R. M.; Pines, A. *Journal of the American Chemical Society* **2013**, *135*, 9576–9.

(53) Shapiro, M. G.; Ramirez, R. M.; Sperling, L. J.; Sun, G.; Sun, J.; Pines, A.; Schaffer, D. V.; Bajaj, V. S. *Nature Chemistry* **2014**, *6*, 629–634.

(54) Finbloom, J. A.; Slack, C. C.; Bruns, C. J.; Jeong, K.; Wemmer, D. E.; Pines, A.; Francis, M. B. *Chemical Communications* **2016**, *52*, 3119–3122.

(55) Klippel, S.; Döpfert, J.; Jayapaul, J.; Kunth, M.; Rossella, F.; Schnurr, M.; Witte, C.; Freund, C.; Schröder, L. *Angewandte Chemie - International Edition* **2014**, *53*, 493–496.

(56) Lerouge, F.; Melnyk, O.; Durand, J. O.; Raehm, L.; Berthault, P.; Huber, G.; Desvaux, H.; Constantinesco, A.; Choquet, P.; Detour, J.; Smaïhi, M. *Journal of Materials Chemistry* **2009**, *19*, 379–386.

(57) Wang, Y.; Dmochowski, I. J. *Chemical Communications* **2015**, *51*, 8982–8985.

(58) Bartik, K.; Luhmer, M.; Dutasta, J.-P.; Collet, A.; Reisse, J. *Journal of the American Chemical Society* **1998**, *120*, 784–791.

(59) Spence, M. M.; Ruiz, E. J.; Rubin, S. M.; Lowery, T. J.; Winssinger, N.; Schultz, P. G.; Wemmer, D. E.; Pines, A. *Journal of the American Chemical Society* **2004**, *126*, 15287–15294.

(60) Lowery, T. J.; Garcia, S.; Chavez, L.; Ruiz, E. J.; Wu, T.; Brotin, T.; Dutasta, J.-P.; King, D. S.; Schultz, P. G.; Pines, A.; Wemmer, D. E. *ChemBioChem* **2005**, *7*, 65–73.

(61) Barrow, S. J.; Kasera, S.; Rowland, M. J.; del Barrio, J.; Scherman, O. A. *Chemical Reviews* **2015**, *115*, 12320–12406.

(62) Shchepotina, E. G.; Pashkina, E. a.; Yakushenko, E. V.; Kozlov, V. a. *Nanotechnologies in Russia* **2011**, *6*, 773–779.

(63) Kim, K.; Selvapalam, N.; Ko, Y. H.; Park, K. M.; Kim, D.; Kim, J. *Chemical Society Reviews* **2007**, *36*, 267–279.

(64) Chen, Y.; Huang, Z.; Zhao, H.; Xu, J. F.; Sun, Z.; Zhang, X. *ACS Applied Materials and Interfaces* **2017**, *9*, 8602–8608.

(65) Jin Jeon, Y.; Kim, S.-Y. Y.; Ho Ko, Y.; Sakamoto, S.; Yamaguchi, K.; Kim, K.; Jeon, Y. J.; Kim, S.-Y. Y.; Ko, Y. H.; Sakamoto, S.; Yamaguchi, K.; Kim, K. *Organic & Biomolecular Chemistry* **2005**, *3*, 2122–2125.

(66) Kim, B. S.; Ko, Y. H.; Kim, Y.; Lee, H. J.; Selvapalam, N.; Lee, H. C.; Kim, K. *Chemical Communications* **2008**, *0*, 2756.

(67) Slack, C. C.; Finbloom, J. A.; Jeong, K.; Bruns, C. J.; Wemmer, D. E.; Pines, A.; Francis, M. B. *Chemical Communications* **2017**, *53*, 1076–1079.

(68) Boutin, C.; Léonce, E.; Brotin, T.; Jerschow, A.; Berthault, P. *Journal of Physical Chemistry Letters* **2013**, *4*, 4172–4176.

(69) Quang, D. T.; Kim, J. S. *Chemical Reviews* **2010**, *110*, 6280–6301.

(70) Cui, L.; Wu, J.; Ju, H. *Biosensors and Bioelectronics* **2015**, *63*, 276–286.

(71) Zhang, J.; Jiang, W.; Luo, Q.; Zhang, X.; Guo, Q.; Liu, M.; Zhou, X. *Talanta* **2014**, *122*, 101–105.

(72) Kotera, N.; Tassali, N.; Løonce, E.; Boutin, C.; Berthault, P.; Brotin, T.; Dutasta, J.-p.; Delacour, L.; Traorø, T.; Buisson, D.-a.; Taran, F.; Coudert, S.; Rousseau, B. *Angewandte Chemie* **2012**, 4176–4179.

(73) Tassali, N.; Kotera, N.; Boutin, C.; Léonce, E.; Boulard, Y.; Rousseau, B.; Dubost, E.; Taran, F.; Brotin, T.; Dutasta, J.-P.; Berthault, P. *Analytical Chemistry* **2014**, *86*, 1783–1788.

(74) Choi, Y. W.; Park, G. J.; Na, Y. J.; Jo, H. Y.; Lee, S. A.; You, G. R.; Kim, C. *Sensors and Actuators B: Chemical* **2014**, *194*, 343–352.

(75) Nieboer, E.; Richardson, D. H. S. *Environmental Pollution Series B, Chemical and Physical* **1980**, *1*, 3–26.

(76) Viola-Villegas, N.; Doyle, R. P. *Coordination Chemistry Reviews* **2009**, *253*, 1906–1925.

(77) Heppeler, A.; André, J. P.; Buschmann, I.; Wang, X.; Reubi, J.-C.; Hennig, M.; Kaden, T. A.; Maecke, H. R. *Chemistry - A European Journal* **2008**, *14*, 3026–3034.

(78) Benetollo, F.; Bombieri, G.; Calabi, L.; Aime, S.; Botta, M. *Inorganic Chemistry* **2003**, *42*, 148–157.

(79) Sears, D. N.; Jameson, C. J. **2003**, *119*, DOI: 10.1063/1.1625364.

(80) Schlundt, A.; Kilian, W.; Beyermann, M.; Sticht, J.; Günther, S.; Höpner, S.; Falk, K.; Roetzschke, O.; Mitschang, L.; Freund, C. *Angewandte Chemie - International Edition* **2009**, *48*, 4142–4145.

(81) Ruiz, E. J.; Sears, D. N.; Pines, A.; Jameson, C. J.; Sciences, M.; Di, V.; National, L. B. **2006**, 16980–16988.

(82) Aime, S.; Botta, M.; Fasano, M.; Marques, M. P. M.; Geraldes, C. F. G. C.; Pubanz, D.; Merbach, A. E. *Inorganic Chemistry* **1997**, *36*, 2059–2068.

(83) Caravan, P. *Chemical Society Reviews* **2006**, *35*, 512.

(84) Park, J. Y.; Baek, M. J.; Choi, E. S.; Woo, S.; Kim, J. H.; Kim, T. J.; Jung, J. C.; Chae, K. S.; Chang, Y.; Lee, G. H. *ACS Nano* **2009**, *3*, 3663–3669.

(85) Ye, D.; Shuhendler, A. J.; Pandit, P.; Brewer, K. D.; Tee, S. S.; Cui, L.; Tikhomirov, G.; Rutt, B.; Rao, J. *Chemical Science* **2014**, *5*, 3845.

(86) Lippert, A. R.; Keshari, K. R.; Kurhanewicz, J.; Chang, C. J. *Journal of the American Chemical Society* **2011**, *133*, 3776–3779.

(87) Angelovski, G.; Gottschalk, S.; Milošević, M.; Engelmann, J.; Hagberg, G. E.; Kadjane, P.; Andjus, P.; Logothetis, N. K. *ACS Chemical Neuroscience* **2014**, *5*, 360–369.

(88) Spence, M. M.; Rubin, S. M.; Dimitrov, I. E.; Ruiz, E. J.; Wemmer, D. E.; Pines, A.; Yao, S. Q.; Tian, F.; Schultz, P. G. *Proceedings of the National Academy of Sciences of the United States of America* **2001**, *98*, 10654–7.

(89) Palaniappan, K. K.; Ramirez, R. M.; Bajaj, V. S.; Wemmer, D. E.; Pines, A.; Francis, M. B. *Angewandte Chemie (International ed. in English)* **2013**, *112*, 1–6.

(90) Szatrowski, T. P.; Nathan, C. F. *Cancer research* **1991**, *51*, 794–8.

(91) Houstis, N.; Rosen, E. D.; Lander, E. S. *Nature* **2006**, *440*, 944–948.

(92) Niethammer, P.; Grabher, C.; Look, A. T.; Mitchison, T. J. *Nature* **2009**, *459*, 996–999.

(93) Reuter, S.; Gupta, S. C.; Chaturvedi, M. M.; Aggarwal, B. B. *Free Radical Biology and Medicine* **2010**, *49*, 1603–1616.

(94) Lee, D.; Khaja, S.; Velasquez-Castano, J. C.; Dasari, M.; Sun, C.; Petros, J.; Taylor, W. R.; Murthy, N. *Nature Materials* **2007**, *6*, 765–769.

(95) Van de Bittner, G. C.; Dubikovskaya, E. A.; Bertozzi, C. R.; Chang, C. J. *Proceedings of the National Academy of Sciences of the United States of America* **2010**, *107*, 21316–21.

(96) Weinstain, R.; Savariar, E. N.; Felsen, C. N.; Tsien, R. Y. *Journal of the American Chemical Society* **2014**, *136*, 874–7.

(97) Srikun, D.; Miller, E. W.; Domaille, D. W.; Chang, C. J. *Journal of the American Chemical Society* **2008**, *130*, 4596–7.

(98) Carroll, V.; Michel, B. W.; Blecha, J.; VanBrocklin, H.; Keshari, K.; Wilson, D.; Chang, C. J. *Journal of the American Chemical Society* **2014**, *136*, 14742–14745.

(99) Lin, V. S.; Dickinson, B. C.; Chang, C. J. *Methods in Enzymology* **2013**, *526*, DOI: 10.1016/B978-0-12-405883-5.00002-8.

(100) Meschke, C.; Buschmann, H. J.; Schollmeyer, E. *Thermochimica Acta* **1997**, *297*, 43–48.

(101) Buschmann, H. J.; Mutihac, L.; Mutihac, R. C.; Schollmeyer, E. *Thermochimica Acta* **2005**, *430*, 79–82.

(102) Danylyuk, O.; Fedin, V. P.; Sashuk, V. *Chemical Communications* **2013**, *49*, 1859–1861.

(103) Martinez-Outschoorn, U. E.; Lin, Z.; Trimmer, C.; Flomenberg, N.; Wang, C.; Pavlides, S.; Pestell, R. G.; Howell, A.; Sotgia, F.; Lisanti, M. P. *Cell cycle (Georgetown, Tex.)* **2011**, *10*, 2504–20.

(104) Rose, H. M.; Witte, C.; Rossella, F.; Klippel, S.; Freund, C.; Schroder, L. *Proceedings of the National Academy of Sciences* **2014**, *111*, 11697–11702.

(105) Riggle, B. A.; Wang, Y.; Dmochowski, I. J. *Journal of the American Chemical Society* **2015**, *137*, 5542–5548.

(106) Piontek, A.; Witte, C.; Rose, H. M.; Eichner, M.; Protze, J.; Krause, G.; Piontek, J.; Schröder, L. *Annals of the New York Academy of Sciences* **2017**, *1397*, 195–208.

(107) Witte, C.; Martos, V.; Rose, H. M.; Reinke, S.; Klippel, S.; Schröder, L.; Hackenberger, C. P. *Angewandte Chemie - International Edition* **2015**, *54*, 2806–2810.

(108) Schnurr, M.; Sydow, K.; Rose, H. M.; Dathe, M.; Schröder, L. *Advanced Healthcare Materials* **2015**, *4*, 40–45.

(109) Cao, L.; Hettiarachchi, G.; Briken, V.; Isaacs, L. *Angewandte Chemie International Edition* **2013**, *52*, 12033–12037.

(110) Hermanson, G. T., *(Strept)avidin–Biotin Systems*, 2013; Vol. 11, pp 465–505.

(111) Isaacs, L.; Park, S.-k.; Liu, S.; Ko, Y. H.; Selvapalam, N.; Kim, Y.; Kim, H.; Zavalij, P. Y.; Kim, G.-h.; Lee, H.-s.; Kim, K. **2005**, *8*, 18000–18001.

(112) Freeman, W. A. *Acta Crystallographica Section B* **1984**, *40*, 382–387.

(113) Wang, Y.; Roose, B. W.; Palovcak, E. J.; Carnevale, V.; Dmochowski, I. J. *Angewandte Chemie - International Edition* **2016**, *55*, 8984–8987.

(114) Roose, B. W.; Zemerov, S. D.; Dmochowski, I. J. *Chem. Sci.* **2017**, 7631–7636.

(115) Lowery, T. J.; Garcia, S.; Chavez, L.; Ruiz, E. J.; Wu, T.; Brotin, T.; Dutasta, J.-P.; King, D. S.; Schultz, P. G.; Pines, A.; Wemmer, D. E. *ChemBioChem* **2006**, *7*, 65–73.

(116) Sears, D. N.; Jameson, C. J.; Harris, R. A. **2004**, *120*, 3277–3283.

(117) Li, X.; Newberry, C.; Saha, I.; Nikolaou, P.; Whiting, N.; Goodson, B. M. *Chemical Physics Letters* **2006**, *419*, 233–239.

(118) Rubin, S. M.; Lee, S.-Y.; Ruiz, E.; Pines, A.; Wemmer, D. E. *Journal of Molecular Biology* **2002**, *322*, 425–440.

(119) Boutin, C.; Stopin, A.; Lenda, F.; Brotin, T.; Dutasta, J. P.; Jamin, N.; Sanson, A.; Boulard, Y.; Leteurtre, F.; Huber, G.; Bogaert-Buchmann, A.; Tassali, N.; Desvaux, H.; Carrire, M.; Berthault, P. *Bioorganic and Medicinal Chemistry* **2011**, *19*, 4135–4143.

(120) Bai, Y.; Wang, Y.; Goulian, M.; Driks, A.; Dmochowski, I. J. *Chemical Science* **2014**, *5*, 3197–3203.

(121) Wei, Q.; Seward, G. K.; Hill, P. A.; Patton, B.; Dimitrov, I. E.; Kuzma, N. N.; Dmochowski, I. J. *Journal of the American Chemical Society* **2006**, *128*, 13274–13283.

(122) Norquay, G.; Leung, G.; Stewart, N. J.; Tozer, G. M.; Wolber, J.; Wild, J. M. *Magnetic resonance in medicine : official journal of the Society of Magnetic Resonance in Medicine / Society of Magnetic Resonance in Medicine* **2014**, *00*, 1–9.

(123) Causier, A.; Carret, G.; Boutin, C.; Berthelot, T.; Berthault, P. *Lab Chip* **2015**, *15*, 2049–2054.

(124) Goodson, B. M. *Journal of magnetic resonance (San Diego, Calif. : 1997)* **2002**, *155*, 157–216.

(125) Amor, N.; Zänker, P. P.; Blümler, P.; Meise, F. M.; Schreiber, L. M.; Scholz, A.; Schmiedeskamp, J.; Spiess, H. W.; Münnemann, K. *Journal of Magnetic Resonance* **2009**, *201*, 93–99.

(126) Cleveland, Z. I.; Möller, H. E.; Hedlund, L. W.; Driehuys, B. *Journal of Physical Chemistry B* **2009**, *113*, 12489–12499.

(127) Jokisaari, J. P.; Luckhurst, G. R.; Timimi, B. A.; Zhu, J.; Zimmermann, H. *Liquid Crystals* **2015**, 1–14.

(128) Keyes, P. H.; Daniels, W. B. **1975**, *63*, 5006–5010.

(129) Croucher, M. D.; Patterson, D. *Journal of Solution Chemistry* **1980**, *9*, 771–784.

(130) Zweckstetter, M.; Bax, A. **2001**, DOI: 10.1023/A.

(131) Thiriot, D. S.; Nevzorov, A. a.; Opella, S. J. *Protein science : a publication of the Protein Society* **2005**, *14*, 1064–70.

(132) Miller, J. B.; Walton, J. H.; Roland, C. M. *Macromolecules* **1993**, *26*, 5602–5610.

(133) Karjalainen, J.; Vaara, J.; Straka, M.; Lantto, P. *Phys. Chem. Chem. Phys.* **2015**, *17*, 7158–7171.

(134) Molga, E.; Stecki, J. *Journal of Chemical Thermodynamics* **1977**, 79–90.

(135) Tsuchiya, H.; Nakamura, K. *Molecular Crystals and Liquid Crystals* **1974**, *29*, 89–101.

(136) Lounila, J.; Jokisaari, J. *Progress in Nuclear Magnetic Resonance Spectroscopy* **1982**, *15*, 249–290.

(137) Emsley, J. W.; Lindon, J. C. PREFACE., 1975.

(138) COURTIEU, J.; BAYLE, J. P.; FUNG, B. M. *ChemInform* **2010**, *25*, no–no.

(139) Chaffee, K. E.; Marjanska, M.; Goodson, B. M. *Solid State Nuclear Magnetic Resonance* **2006**, *29*, 104–112.

(140) Ulrich, A. S.; Grage, S. L. *Studies in Physical and Theoretical Chemistry* **1998**, *84*, DOI: 10.1016/S0167-6881(98)80010-4.

(141) Siminovitch, D. J.; Jeffrey, K. R. **1981**, *645*, 270–278.

(142) Péchiné, J.-M.; Meddour, A.; Courtieu, J. *Chem. Commun.* **2002**, 1734–1735.

(143) Marjanska, M.; Goodson, B. M.; Castiglione, F.; Pines, A. *The Journal of Physical Chemistry B* **2003**, *107*, 12558–12561.

(144) Dierking, I.; Al-zangana, S. *Nanomaterials* **2017**, *7*, DOI: 10.3390/nano7100305.

(145) Gomes, M. Progress in Xenon and Proton Relaxation Based Sensing., Ph.D. Thesis, UC Berkeley, 2017.

Appendix

Lorentzian fit functions for hyperCEST data

The code used to process FIDs for z-spectra plotting has been reported several times elsewhere. For a thorough description, refer to Gomes, 2017.[145] The following scripts were used to fit data after FIDs had been Fourier Transformed and normalized, and are comprised of a simple error-minimizing function that compares actual peak widths and positions to theoretical Lorentzian lineshapes, and compares the two until the difference between data and theoretical shapes are within a directed tolerance. Again, this function does not account for spill-over saturation effects that can arise in hyperCEST experiments, and so this data was primarily used for qualitative visualization.

fit.m

Begin by inputing saturation frequencies and integrated FID areas from hyperCEST processing. The function fminsearch searches for the minimum of function fitlorentzian(lambda,t,y) using only lambda as variable input argument, which is technically an error between the fit and y data and iterates until the constraints of 'options' (number of iterations, optimization time, and/or error tolerance) are met.

```
t=[%List of saturation frequencies%];
y=[%List of integrated areas from FIDs%];

format compact
global c

start = [position1, width1, position2, width2,...];
%starting guesses from 'start;'

options = optimset('TolFun',1e-10);
options.MaxIter = 1e20;
options.MaxFunEvals = 1e20;
% Determines how close the model must fit the data

tic
parameter=fminsearch(@(lambda)(fitlorentzianb(lambda,t,y)),start,options);
toc
```

fitlorentzianb.m

Fitting functions for a Lorentzian band spectrum with flat baseline correction. Returns baseline as c(1), position as c(2), and width as c(3).

```
function err = fitlorentzianb(lambda,t,y)
global c
A = zeros(length(t),round(length(lambda)/2));
for j = 1:length(lambda)/2,
    A(:,j) = lorentzian(t,lambda(2*j-1),lambda(2*j))';
end
B=[ones(size(y))' A];
c = B\y';
%compute the n-length peak height vector by least-squares regression
z = B*c;
err = norm(z-y');
```

---

parameters = fminsearch(@(lambda)(fitfunction(lambda,x,y)),start) performs an iterative fit of the data in the vectors x,y to a model described in a previously-created function called fitfunction, using the first guesses in the vector start.
If there are n peaks in the model, then the length of lambda is 2n, one entry for each iterated variable ([position1 width1 position2 width2....etc]).
For loop constructs n x length(t) matrix containing a Lorentzian model for each peak, then computes n-length peak height vector c by least-squares regression. resulting peak heights used to compute z, sum of all n model peaks, then err computes RSD between model z and data y. z is returned to calling function fminsearch and evaluated again until err is minimized.

lorentzian.m

A simple Lorentzian function.

```
function g = lorentzian(x,position,width)
% lorentzian(x,position,width) is a Lorentzian function that takes
% arguments x, position, and width, where x may be scalar, vector, or matrix.
% Position and width are scalar

g=ones(size(x))./(1+((x-position)./(0.5.*width)).^2);
```

fminsearch.m

```
% fminsearch is a multidimensional unconstrained nonlinear minimization
% (Nelder-Mead).

function [x,fval,exitflag,output] = fminsearch(funfcn,x,options,varargin)

% X = fminsearch(FUN,X0,OPTIONS)  minimizes with the default optimization
% parameters replaced by values in the structure OPTIONS.

defaultopt=struct('Display','notify','MaxIter','200*numberOfVariables',...
    'MaxFunEvals','200*numberOfVariables','TolX',1e-4,'TolFun',1e-4, ...
    'FunValCheck','off','OutputFcn',[],'PlotFcns',[]);

% If just 'defaults' passed in, return the default options in X
if nargin==1 && nargout <= 1 && strcmpi(funfcn,'defaults')
    x = defaultopt;
    return
end

if nargin<3, options = []; end

% Detect problem structure input
if nargin == 1
    if isa(funfcn,'struct')
        [funfcn,x,options] = separateOptimStruct(funfcn);
    else % Single input and non-structure
        error('MATLAB:fminsearch:InputArg',...
            getString(message('MATLAB:optimfun:fminsearch:InputArg')));
    end
end

if nargin == 0
    error('MATLAB:fminsearch:NotEnoughInputs',...
        getString(message('MATLAB:optimfun:fminsearch:NotEnoughInputs')));
end

% Check for non-double inputs
if ~isa(x,'double')
  error('MATLAB:fminsearch:NonDoubleInput',...
    getString(message('MATLAB:optimfun:fminsearch:NonDoubleInput')));
```

```
end

n = numel(x);
numberOfVariables = n;

% Check that options is a struct
if ~isempty(options) && ~isa(options,'struct')
    error('MATLAB:fminsearch:ArgNotStruct',...
    getString(message('MATLAB:optimfun:commonMessages:ArgNotStruct',3)));
end

printtype = optimget(options,'Display',defaultopt,'fast');
tolx = optimget(options,'TolX',defaultopt,'fast');
tolf = optimget(options,'TolFun',defaultopt,'fast');
maxfun = optimget(options,'MaxFunEvals',defaultopt,'fast');
maxiter = optimget(options,'MaxIter',defaultopt,'fast');
funValCheck = strcmp(optimget(options,'FunValCheck', ...
defaultopt,'fast'),'on');

% In case the defaults were gathered from calling: optimset('fminsearch'):
if ischar(maxfun) || isstring(maxfun)
    if strcmpi(maxfun,'200*numberofvariables')
        maxfun = 200*numberOfVariables;
    else
        error('MATLAB:fminsearch:OptMaxFunEvalsNotInteger',...
         getString(message('MATLAB:optimfun:fminsearch: ...
         OptMaxFunEvalsNotInteger')));
    end
end
if ischar(maxiter) || isstring(maxiter)
    if strcmpi(maxiter,'200*numberofvariables')
        maxiter = 200*numberOfVariables;
    else
        error('MATLAB:fminsearch:OptMaxIterNotInteger',...
            getString(message('MATLAB:optimfun:fminsearch:
            OptMaxIterNotInteger')));
    end
end

switch printtype
    case {'notify','notify-detailed'}
        prnt = 1;
```

```
    case {'none','off'}
        prnt = 0;
    case {'iter','iter-detailed'}
        prnt = 3;
    case {'final','final-detailed'}
        prnt = 2;
    case 'simplex'
        prnt = 4;
    otherwise
        prnt = 1;
end
% Handle the output
outputfcn = optimget(options,'OutputFcn',defaultopt,'fast');
if isempty(outputfcn)
    haveoutputfcn = false;
else
    haveoutputfcn = true;
    xOutputfcn = x; % Last x passed to outputfcn; has input x's shape
    % Parse OutputFcn which is needed to support cell array syntax
    % for OutputFcn.

    outputfcn = createCellArrayOfFunctions(outputfcn,'OutputFcn');
end

% Handle the plot
plotfcns = optimget(options,'PlotFcns',defaultopt,'fast');
if isempty(plotfcns)
    haveplotfcn = false;
else
    haveplotfcn = true;
    xOutputfcn = x; % Last x passed to plotfcns; has input x's shape
    % Parse PlotFcns which is needed to support cell array syntax
    % for PlotFcns.
    plotfcns = createCellArrayOfFunctions(plotfcns,'PlotFcns');
end

header = ' Iteration   Func-count     min f(x)         Procedure';

% Convert to function handle as needed.
funfcn = fcnchk(funfcn,length(varargin));
% Add a wrapper function to check for Inf/NaN/complex values
if funValCheck
```

```
    % Add a wrapper function, CHECKFUN, to check for NaN/complex values
    % withouth having to change the calls that look like this:
    % f = funfcn(x,varargin{:});
    % x is first argument to CHECKFUN, then the user's function, then
    % the elements of varargin. To accomplish this we need to add the
    % user's function to the beginning of varargin, and change funfcn
    % to be CHECKFUN.
    varargin = [{funfcn}, varargin];
    funfcn = @checkfun;
end

n = numel(x);

% Initialize parameters
rho = 1; chi = 2; psi = 0.5; sigma = 0.5;
onesn = ones(1,n);
two2np1 = 2:n+1;
one2n = 1:n;

% Set up a simplex near the initial guess.
xin = x(:); % Force xin to be a column vector
v = zeros(n,n+1); fv = zeros(1,n+1);
v(:,1) = xin;    % Place input guess in the simplex! (credit L.Pfeffer)
x(:) = xin;    % Change x to the form expected by funfcn
fv(:,1) = funfcn(x,varargin{:});
func_evals = 1;
itercount = 0;
how = '';
% Initial simplex setup continues later

% Initialize the output and plot functions.
if haveoutputfcn || haveplotfcn
    [xOutputfcn, optimValues, stop] = callOutputAndPlotFcns(outputfcn, ...
    plotfcns,v(:,1),xOutputfcn,'init',itercount, ...
        func_evals, how, fv(:,1),varargin{:});
    if stop
        [x,fval,exitflag,output] = cleanUpInterrupt(xOutputfcn, ...
        optimValues);
        if  prnt > 0
            disp(output.message)
        end
        return;
```

```
    end
end

% Print out initial f(x) as 0th iteration
if prnt == 3
    disp(' ')
    disp(header)
    fprintf(' %5.0f %5.0f %12.6g %s\n', itercount, func_evals, fv(1), how);
elseif prnt == 4
    formatsave.format = get(0,'format');
    formatsave.formatspacing = get(0,'formatspacing');
    % reset format when done
    oc1 = onCleanup(@()set(0,'format',formatsave.format));
    oc2 = onCleanup(@()set(0,'formatspacing',formatsave.formatspacing));
    format compact
    format short e
    disp(' ')
    disp(how)
    disp('v = ')
    disp(v)
    disp('fv = ')
    disp(fv)
    disp('func_evals = ')
    disp(func_evals)
end
% OutputFcn and PlotFcns call
if haveoutputfcn || haveplotfcn
    [xOutputfcn, optimValues, stop] = callOutputAndPlotFcns(outputfcn, ...
    plotfcns,v(:,1),xOutputfcn,'iter',itercount, ...
        func_evals, how, fv(:,1),varargin{:});
    if stop  % Stop per user request.
        [x,fval,exitflag,output] = cleanUpInterrupt(xOutputfcn, ...
        optimValues);
        if  prnt > 0
            disp(output.message)
        end
        return;
    end
end

% Continue setting up the initial simplex.
```

```
% Following improvement suggested by L.Pfeffer at Stanford
usual_delta = 0.05;         % 5 percent deltas for non-zero terms
zero_term_delta = 0.00025;  % Even smaller delta for zero elements of x
for j = 1:n
    y = xin;
    if y(j) ~= 0
        y(j) = (1 + usual_delta)*y(j);
    else
        y(j) = zero_term_delta;
    end
    v(:,j+1) = y;
    x(:) = y; f = funfcn(x,varargin{:});
    fv(1,j+1) = f;
end

% sort so v(1,:) has the lowest function value
[fv,j] = sort(fv);
v = v(:,j);

how = 'initial simplex';
itercount = itercount + 1;
func_evals = n+1;
if prnt == 3
    fprintf(' %5.0f %5.0f %12.6g %s\n', itercount, func_evals, fv(1), how)
elseif prnt == 4
    disp(' ')
    disp(how)
    disp('v = ')
    disp(v)
    disp('fv = ')
    disp(fv)
    disp('func_evals = ')
    disp(func_evals)
end
% OutputFcn and PlotFcns call
if haveoutputfcn || haveplotfcn
    [xOutputfcn, optimValues, stop] = callOutputAndPlotFcns(outputfcn, ...
    plotfcns,v(:,1),xOutputfcn,'iter',itercount, ...
        func_evals, how, fv(:,1),varargin{:});
    if stop  % Stop per user request.
        [x,fval,exitflag,output] = cleanUpInterrupt(xOutputfcn, ...
        optimValues);
```

```
        if  prnt > 0
            disp(output.message)
        end
        return;
    end
end
exitflag = 1;

% Main algorithm: iterate until
% (a) the maximum coordinate difference between the current best point and
% the other points in the simplex is less than or equal to TolX.
% Specifically, until max(||v2-v1||,||v3-v1||,...,||v(n+1)-v1||) <= TolX,
% where ||.|| is the infinity-norm, and v1 holds the
% vertex with the current lowest value; AND
% (b) the corresponding difference in function values is less than
% or equal to TolFun. (Cannot use OR instead of AND.)
% The iteration stops if the maximum number of iterations or
% function evaluations are exceeded
while func_evals < maxfun && itercount < maxiter
    if max(abs(fv(1)-fv(two2np1))) <= max(tolf,10*eps(fv(1))) && ...
            max(max(abs(v(:,two2np1)-v(:,onesn)))) <= ...
            max(tolx,10*eps(max(v(:,1))))
        break
    end

    % Compute the reflection point

    % xbar = average of the n (NOT n+1) best points
    xbar = sum(v(:,one2n), 2)/n;
    xr = (1 + rho)*xbar - rho*v(:,end);
    x(:) = xr; fxr = funfcn(x,varargin{:});
    func_evals = func_evals+1;

    if fxr < fv(:,1)
        % Calculate the expansion point
        xe = (1 + rho*chi)*xbar - rho*chi*v(:,end);
        x(:) = xe; fxe = funfcn(x,varargin{:});
        func_evals = func_evals+1;
        if fxe < fxr
            v(:,end) = xe;
            fv(:,end) = fxe;
            how = 'expand';
```

```
    else
        v(:,end) = xr;
        fv(:,end) = fxr;
        how = 'reflect';
    end
else % fv(:,1) <= fxr
    if fxr < fv(:,n)
        v(:,end) = xr;
        fv(:,end) = fxr;
        how = 'reflect';
    else % fxr >= fv(:,n)
        % Perform contraction
        if fxr < fv(:,end)
            % Perform an outside contraction
            xc = (1 + psi*rho)*xbar - psi*rho*v(:,end);
            x(:) = xc; fxc = funfcn(x,varargin{:});
            func_evals = func_evals+1;

            if fxc <= fxr
                v(:,end) = xc;
                fv(:,end) = fxc;
                how = 'contract outside';
            else
                % perform a shrink
                how = 'shrink';
            end
        else
            % Perform an inside contraction
            xcc = (1-psi)*xbar + psi*v(:,end);
            x(:) = xcc; fxcc = funfcn(x,varargin{:});
            func_evals = func_evals+1;

            if fxcc < fv(:,end)
                v(:,end) = xcc;
                fv(:,end) = fxcc;
                how = 'contract inside';
            else
                % perform a shrink
                how = 'shrink';
            end
        end
        if strcmp(how,'shrink')
```

```
                for j=two2np1
                    v(:,j)=v(:,1)+sigma*(v(:,j) - v(:,1));
                    x(:) = v(:,j); fv(:,j) = funfcn(x,varargin{:});
                end
                func_evals = func_evals + n;
            end
        end
    end
    [fv,j] = sort(fv);
    v = v(:,j);
    itercount = itercount + 1;
    if prnt == 3
        fprintf(' %5.0f  %5.0f  %12.6g  %s\n', ...
        itercount, func_evals, fv(1), how)
    elseif prnt == 4
        disp(' ')
        disp(how)
        disp('v = ')
        disp(v)
        disp('fv = ')
        disp(fv)
        disp('func_evals = ')
        disp(func_evals)
    end
    % OutputFcn and PlotFcns call
    if haveoutputfcn || haveplotfcn
        [xOutputfcn, optimValues, stop] = callOutputAndPlotFcns( ...
        outputfcn,plotfcns,v(:,1),xOutputfcn,'iter',itercount, ...
            func_evals, how, fv(:,1),varargin{:});
        if stop  % Stop per user request.
            [x,fval,exitflag,output] = cleanUpInterrupt(xOutputfcn, ...
            optimValues);
            if  prnt > 0
                disp(output.message)
            end
            return;
        end
    end
end   % while

x(:) = v(:,1);
fval = fv(:,1);
```

```
output.iterations = itercount;
output.funcCount = func_evals;
output.algorithm = 'Nelder-Mead simplex direct search';

% OutputFcn and PlotFcns call
if haveoutputfcn || haveplotfcn
    callOutputAndPlotFcns(outputfcn,plotfcns,x,xOutputfcn,'done', ...
    itercount, func_evals, how, fval, varargin{:});
end

if func_evals >= maxfun
    msg = getString(message('MATLAB:optimfun:fminsearch: ...
    ExitingMaxFunctionEvals', sprintf('%f',fval)));
    if prnt > 0
        disp(' ')
        disp(msg)
    end
    exitflag = 0;
elseif itercount >= maxiter
    msg = getString(message('MATLAB:optimfun:fminsearch: ...
    ExitingMaxIterations', sprintf('%f',fval)));
    if prnt > 0
        disp(' ')
        disp(msg)
    end
    exitflag = 0;
else
    msg = ...
      getString(message('MATLAB:optimfun:fminsearch: ...
      OptimizationTerminatedXSatisfiesCriteria', ...
               sprintf('%e',tolx), sprintf('%e',tolf)));
    if prnt > 1
        disp(' ')
        disp(msg)
    end
    exitflag = 1;
end

output.message = msg;
```

```
%---------------------------------------------------------------------------
function [xOutputfcn, optimValues, stop] = ...
callOutputAndPlotFcns(outputfcn,plotfcns,x,xOutputfcn,state,iter,...
    numf,how,f,varargin)
% CALLOUTPUTANDPLOTFCNS assigns values to the struct OptimValues and then
% calls the outputfcn/plotfcns.
%
% state - can have the values 'init','iter', or 'done'.

% For the 'done' state we do not check the value of 'stop' because the
% optimization is already done.
optimValues.iteration = iter;
optimValues.funccount = numf;
optimValues.fval = f;
optimValues.procedure = how;

xOutputfcn(:) = x;  % Set x to have user expected size
stop = false;
state = char(state);
% Call output functions
if ~isempty(outputfcn)
    switch state
        case {'iter','init'}
            stop = callAllOptimOutputFcns(outputfcn,xOutputfcn, ...
            optimValues,state,varargin{:}) || stop;
        case 'done'
            callAllOptimOutputFcns(outputfcn,xOutputfcn,optimValues, ...
            state,varargin{:});
        otherwise
            error('MATLAB:fminsearch:InvalidState',...
                getString(message('MATLAB:optimfun:fminsearch: ...
                InvalidState')));
    end
end
% Call plot functions
if ~isempty(plotfcns)
    switch state
        case {'iter','init'}
            stop = callAllOptimPlotFcns(plotfcns,xOutputfcn, ...
            optimValues,state,varargin{:}) || stop;
        case 'done'
            callAllOptimPlotFcns(plotfcns,xOutputfcn,optimValues, ...
```

```
            state,varargin{:});
        otherwise
            error('MATLAB:fminsearch:InvalidState',...
                getString(message('MATLAB:optimfun:fminsearch: ...
                InvalidState')));
    end
end

%-----------------------------------------------------------------------
function [x,FVAL,EXITFLAG,OUTPUT] = cleanUpInterrupt(xOutputfcn,optimValues)
% CLEANUPINTERRUPT updates or sets all the output arguments of FMINBND
% when the optimization is interrupted.

% Call plot function driver to finalize the plot function figure window.
% If no plot functions have been specified or the plot function figure no
% longer exists, this call just returns.
callAllOptimPlotFcns('cleanuponstopsignal');

x = xOutputfcn;
FVAL = optimValues.fval;
EXITFLAG = -1;
OUTPUT.iterations = optimValues.iteration;
OUTPUT.funcCount = optimValues.funccount;
OUTPUT.algorithm = 'Nelder-Mead simplex direct search';
OUTPUT.message = getString(message('MATLAB:optimfun:fminsearch: ...
OptimizationTerminatedPrematurelyByUser'));

%-----------------------------------------------------------------------
function f = checkfun(x,userfcn,varargin)
% CHECKFUN checks for complex or NaN results from userfcn.

f = userfcn(x,varargin{:});
% Note: we do not check for Inf as FMINSEARCH handles it naturally.
if isnan(f)
    error('MATLAB:fminsearch:checkfun:NaNFval',...
        getString(message('MATLAB:optimfun:fminsearch:checkfun:NaNFval', ...
        localChar( userfcn ))));
elseif ~isreal(f)
    error('MATLAB:fminsearch:checkfun:ComplexFval',...
        getString(message('MATLAB:optimfun:fminsearch:checkfun: ...
        ComplexFval', localChar( userfcn ))));
end
```

```
%---------------------------------------------------------------------------
function strfcn = localChar(fcn)
% Convert the fcn to a character array for printing

if ischar(fcn)
    strfcn = fcn;
elseif isstring(fcn) || isa(fcn,'inline')
    strfcn = char(fcn);
elseif isa(fcn,'function_handle')
    strfcn = func2str(fcn);
https://www.overleaf.com/project/5bea427ef455f133d8f6b52delse
    try
        strfcn = char(fcn);
    catch
        strfcn = getString(message('MATLAB:optimfun:fminsearch: ...
        NameNotPrintable'));
    end
end
```

Reference for fminsearch script: Jeffrey C. Lagarias, James A. Reeds, Margaret H. Wright, Paul E. Wright, "Convergence Properties of the Nelder-Mead Simplex Method in Low Dimensions", SIAM Journal of Optimization, 9(1): p.112-147, 1998. Copyright 1984-2017 The MathWorks, Inc.